VISCOELASTIC CHARACTERIZATION OF CHONDROCYTES WITH A 3D-PRINTED VARIABLE-HEIGHT FLUIDIC DEVICE

by

Michael John Neubauer

A dissertation submitted in partial fulfillment
of the requirements for the degree

of

Doctor of Philosophy

in

Mechanical Engineering

MONTANA STATE UNIVERSITY
Bozeman, Montana

Decemeber 2024

©COPYRIGHT

by

Michael John Neubauer

2024

All Rights Reserved

ACKNOWLEDGEMENTS

Firstly, I would like to acknowledge my advisor, Dr. Stephan Warnat, for providing an opportunity to join his lab and for his continuing support, guidance, and mentorship. Stephan's patience and optimism were exactly what I needed. I also want to thank my committee members, Dr. Ron June, Dr. Cecily Ryan, and Dr. Alan Fine, for their support and advice. A special thanks to Dr. Priyanka Brahmachary for preparing all the chondrocyte cells for my research. Thank you to all the graduate students and researchers who trained, collaborated with, and supported me: Dr. Matt Mcglennen, Maddy Thomae, Dr. Seth Kane, Daniel Collins, Haley Ketteler, Hande Arpali, Jonah Theisen, Dr. Markus Dieser, Dr. Heidi Smith, and Dr. Kristin Connolly. Thank you to all the undergraduates I had the privilege of instructing and mentoring as a graduate student, particularly Kadin Ritter, Ryan Kulasekara, and Stacey Mockel, for helping me improve as a mentor. A big thank you to my undergraduate roommates Peter, Max, Ben, and Zack for convincing me that graduate school was possible. Lastly, I thank my parents, Steve and Joyce, for their unceasing love and support and for teaching me what truly matters in life.

TABLE OF CONTENTS

1. INTRODUCTION 1

Motivation 1
Dissertation Outline 1
Background 3
Mechanical Characterization of Cells 4
Cell Mechanics 4
Conventional Single-Cell Characterization Methods 5
Microfluidic Integrated Methods 8
Passive Microfluidics 9
Microfluidic Micropipette Aspiration 9
Deformability Cytometry 11
Active Microfluidics 15
Flow-through PDMS Membranes 15
Non-flow-through Devices 18
Comparing Passive and Active Methods 19
Chondrocytes 22
Knowledge Gaps 23
Research Goals, Hypotheses, and Objectives 25

2. THEORY 28

Linear Viscoelastic Models 28
Burgers Model Derivation 31

3. 3D PRINTING ON GLASS FOR DIRECT SENSOR INTEGRATION 36

Contribution of Authors and Co-Authors 36
Manuscript Information 37
Abstract 38
Introduction 38
Methods 41
Component Characterization 44
Device Characterization 46
Sample Applications 47
Results and Discussion 49
Component Characterization 49
Device Characterization 51
Sample Applications 51
Discussion 52

TABLE OF CONTENTS – CONTINUED

Conclusion 54

4. VISCOELASTIC RECOVERY TIMES OF CHONDROCYTES MEASURED USING A NOVEL 3D-PRINTED DEVICE 55

Contribution of Authors and Co-Authors 55
Manuscript Information 56
Abstract 57
Introduction 57
Materials and Methods 59
3D-printed Flow Cell Fabrication and Assembly 59
Cell Culture 62
Cell Compression Procedure 63
Microscopy 64
Image Analysis 64
Theory 65
Results and Discussion 67
Image Analysis and Curve Fitting 67
Cell Deformation and Recovery 67
Discussion 70
Conclusion 72

5. VISCOELASTIC PROPERTIES OF CHONDROCYTES FROM MONOLAYER AND ALGINATE CULTURES 73

Contribution of Authors and Co-Authors 73
Manuscript Information 74
Abstract 75
Introduction 75
Methodology 77
Flow-cell and CLSM Imaging 77
Chondrocyte Harvest and Culture 78
Calcein AM and Wheat Germ Agglutinin Staining 79
Data Analysis 80
Results and Discussion 81
Cell Appearance 81
Viscoelastic Recovery Time 84
Discussion 87
Conclusion 88

TABLE OF CONTENTS – CONTINUED

6. CONCLUSION AND FUTURE OUTLOOK 89

REFERENCES CITED 94

APPENDICES 116

APPENDIX A : Laplace Transforms 117
APPENDIX B : Supplemental Material for: Viscoelastic recovery times of chondrocytes measured using a novel 3D-printed device 119

LIST OF TABLES

Table Page

2.1 Common linear viscoelastic mechanical models..... 30

A.1 Laplace transforms.....118

LIST OF FIGURES

Figure Page

1.1 Example mechanical models for cells 6

1.2 Microfluidic micropipette aspiration 10

1.3 PDMS membranes for cell deformation 16

2.1 Burgers mechanical model 31

3.1 Modified build plate 42

3.2 Micro-machined sensor 43

3.3 Fabrication process and image of device 45

3.4 Mean transmission of 502 nm and 660 nm light 50

3.5 Microbeads viewed through through glass and 3D printed structure 50

3.6 Results of device characterization 52

3.7 Results of measuring various conductivity solutions 53

3.8 Nyquist plot of three different dilutions of *E. coli* K12 cells in milli-Q water 53

4.1 A conceptual overview of the 3D-printed variable-height fluidic device 60

4.2 Exploded drawing of the device and an image of it mounted in the microscope 61

4.3 2D image projection and edge detection 65

4.4 Burgers model and general recovery 66

4.5 Projected area and linear strain of a chondrocyte 67

4.6 Images of three cells at three time points; prior to applied strain, at maximum strain, and after 3 minutes of recovery, respectively. 68

4.7 Total vs permanent strain of cells. 69

4.8 Recovery time of bovine chondrocytes as a function of total applied compressive strain. 70

5.1 Monolayer vs alginate cultures for chondrocytes 79

LIST OF FIGURES – CONTINUED

Figure Page

5.2 Fitting the projected area of chondrocytes with a Burgers equation 81

5.3 CLSM images of bovine chondrocytes from monolayer and alginate cultures 82

5.4 CLSM images of bovine chondrocytes from a monolayer culture 83

5.5 CLSM images of primary OA chondrocytes from monolayer and alginate cultures 84

5.6 Total strain vs permanent strain for bovine and primary OA chondrons from monolayer cultures 85

5.7 A boxplot of the viscoelastic recovery time for bovine and primary OA chondrocytes from monolayer cultures 85

5.8 Boxplots of the viscoelastic recovery time for bovine and primary OA chondrocytes from monolayer and alginate cultures 86

B.1 FTIR spectra of glass and tape showing effective tape removal 120

B.2 An overview schematic of the custom pressure controller 121

B.3 Response time of pressure controller 121

B.4 Cell size does not influence permanent strain 122

ABSTRACT

Mechanical characterization of cells supports advancements in tissue engineering, drug development, and diagnostics, making it an essential tool in basic research and clinical applications. Conventional methods, such as atomic force microscopy (AFM) and micropipette aspiration (MPA), are currently limited by a low throughput of roughly 10 cells/h. To address this challenge, this work aims to develop a measurement platform with increased throughput to characterize chondrocyte cells responsible for maintaining the articular cartilage, which lines bones in joints and is associated with a prevalent disease, osteoarthritis (OA).

A 3D-printed variable-height fluidic channel was fabricated on a glass substrate to apply mechanical deformation to chondrocyte cells suspended in a buffer solution. Chondrocytes were compressed between two pieces of glass integrated into the 3D-printed fluidic channel and then recovered to their original shape after removing the applied strain. The cells' cytoplasm was fluorescently stained and imaged with confocal laser scanning microscopy (CLSM) during deformation and recovery. The projected area of chondrocytes was converted to linear strain and fit to a Burgers viscoelastic mechanical model. The viscoelastic recovery time of bovine chondrocytes was found to be 39 s with a std of 18 s, which was consistent with previously reported values from MPA and AFM measurements.

It has been shown that chondrocytes harvested from cartilage and grown in 2D monolayer cultures do not mimic the *in vivo* phenotype, preventing the translation of research to practical applications. The developed measurement platform was used to compare chondrocytes from the typical 2D monolayer cultures to a recently developed 3D alginate-encapsulation culture, which produces chondrocytes visually resembling the *in vivo* phenotype. Chondrocytes from monolayer and alginate cultures were distinct, with 31 s and 13 s recovery times, respectively, for bovine chondrocytes. This difference was also observed for primary OA chondrocytes, with a recovery time of 34 s and 13 s for monolayer and alginate cultures, respectively.

This work demonstrates a novel measurement platform capable of a throughput of 50 cells/h. Given this system's throughput scales with FOV, it shows great potential for the mechanical characterization of cells.

1

INTRODUCTION

Motivation

In recent years, the investigation of the mechanical properties of cells has emerged as a pivotal area of research, providing valuable insights into cellular behavior, function, and responses to environmental cues. The ability to accurately characterize the mechanical features of cells is integral to understanding fundamental cellular processes, unraveling disease mechanisms, and advancing therapeutic interventions. The mechanical properties of cells, including stiffness, deformability, and adhesion, are critical indicators of cellular health and functionality. These properties play pivotal roles in cellular processes such as migration, division, and response to external stimuli. Understanding cell mechanics is particularly crucial in the context of diseases, as alterations in mechanical properties are often associated with pathological conditions, including cancer, neurodegenerative disorders, and cardiovascular diseases. Moreover, investigations into cell mechanics have contributed significantly to tissue engineering and regenerative medicine, where tailored mechanical environments are essential for designing effective biomaterials and supporting the integration of transplanted cells. Researchers have gained a deeper appreciation for cellular behavior by exploring the mechanical intricacies of cells, paving the way for advancements in diagnostics, drug development, and therapeutic interventions.

Dissertation Outline

Chapter 1: Introduction. An overview of technologies for measuring mechanical properties of cells is presented first, followed by a review of active and passive microfluidic

methods. A brief explanation of chondrocyte cells is included afterwards. Key research gaps and research objectives are presented. The main body of this dissertation (Chapter 3-5), address the outlined objectives.

Chapter 2: This chapter describes linear-viscoelastic mechanical models used for cell modeling. It presents the functions of springs and dashpots and key behaviors which can be accounted for by combinations of these elements. A mathematical derivation of the four-element Burgers model is provided using Laplace transforms. Finally, a rational for converting projected area to linear strain is explained.

Chapter 3: "3D printing on glass for direct sensor integration", published in Engineering Research Express, December 2019. This works demonstrates the process of 3D printing open-faced channels directly on a glass substrates for the benefit of improved microscopy and sensor integration. The microfabricated electrical impedance spectroscopy (EIS) sensor is evaluated by electrical sheet resistance (collinear four-point-probe), Raman spectroscopy, and conductivity standard solutions before and after printing a fluidic channel directly over the sensor. No changes in the sensor surface or performance is observed and its function is exhibited by measuring the conductivity and EIS spectra of conductivity solutions and *E.coli* K12 dilutions, respectively.

From this work, 3D printing on glass is shown to be a viable method for creating a fluidic channel on a glass substrate and this work describes the methods developed for this purpose. The next step is the creation of the proposed variable-height flow channel.

Chapter 4: "Viscoelastic recovery times of chondrocytes measured using a novel 3D-printed device", prepared for submission to the Journal of Biomedical Microdevices, November, 2024. In this study, the design, fabrication, and use of a 3D-printed variable-height flow channel is presented. An in depth explanation of the 3D printing and assembly of the device is provided and the device is used with confocal microscopy to measure the viscoelastic recovery time of chondrocyte cells. The results demonstrate that the device is

capable of measuring viscoelastic recovery time and those times are consistent with previously published literature.

The 3D printing on glass method previously developed is expanded for 3D printing on a thin glass coverslip. The proposed device is fabricated and shown the be capable of measuring viscoelastic properties of chondrocytes. Now that the device is fabricated and tested, the next step was to use it to explore if chondrocyte culturing methods changed their viscoelastic properties.

Chapter 5: "Viscoelastic properties of chondrocytes from monolayer and alginate cultures", prepared for submission to the Journal of Biomechanics, December, 2024. In this work, an analysis of primary osteoarthritic and bovine chondrocytes from monolayer and alginate cultures characterized with the developed device is presented. The results suggest that cells cultured in alginate have a reduced recovery time and increased percentage elastic recovery compared to monolayer culures.

Chapter 6: Conclusions and future direction of the presented variable-height flow channel. This chapter highlights the key findings and conclusion fo this work. The remaining challenges, and possible future directions of this technology are discussed.

Background

Given the importance of studying cell mechanics, several technologies have been developed for this purpose, which are briefly described here and in more detail in other reviews [1–7]. The limiting factors for these technologies are the throughput and the number of cells characterized per time. Low-throughput technologies have a throughput of approximately 10 cells/h [2, 8]; however, throughput is often not measured or reported. Microfluidics have been widely used to overcome this challenge. Microfluidics involves the precise control of small volumes of fluids in micrometer-scale channels. Mesofluidic devices with millimeter- or centimeter-sized channels work in the same way and are not distinguished

in this review. Microfluidic devices enable researchers to control the microenvironment surrounding cells with high precision and greatly decrease the cell handling and positioning difficulties associated with traditional and macroscopic cell mechanical characterization technologies, thereby increasing the measurement throughput. An et al [9] recently reviewed high-throughput microfluidic devices that utilize static microfluidic channels to measure cell mechanical properties by imaging cell deformation through constricting channels and fluid-flow-induced strain.

While less common, non-static (movable) microfluidic channels have also been used to study biomechanics, including mechanotransduction, the process by which cells sense and respond to their mechanical environments. Cells transduce these signals into various biological outputs, which can alter their mechanical properties. These microdevices are typically more difficult to fabricate and operate, but can apply dynamic deformation to cells. Onal et al [10] reviewed these microdevices, particularly those capable of applying compressive deformations to cells. The authors stressed the need for the development of novel microfluidic-based flexible microdevices.

Mechanical Characterization of Cells

Cell Mechanics

Although the cell is considered the fundamental unit of life, it is still a highly complex structure that is difficult to mechanically describe. The mechanical models used in experiments to measure the mechanical properties of cells are greatly simplified and are only capable of approximating cell behavior under controlled conditions and assumptions. These general mechanical models are valuable and necessary for studying cell mechanics.

Mechanical models are classified into two groups: the continuum approach, in which cell materials are modeled as a continuum, and the nanostructural approach, which focuses on the cytoskeleton structure of cells [11]. Of these, the continuum approach has been used more often in the examples in this review and is briefly described here. There are several

subcategories of continuum models, including liquid-drop, solid, and power-law models [1, 12, 13]. Liquid-drop models describe a cell as a thin circular membrane with constant tension that encapsulates a liquid. These models vary in their description of the liquid [12], the simplest being a Newtonian liquid with a constant viscosity, as shown in Figure 1.1(a). Solid models are divided into elastic and viscoelastic categories. An elastic solid deforms from an applied force and instantly recovers its original shape when the force is removed. The simplest formulation is the linear-elastic solid shown in Figure 1.1(b), where a spring is used to describe the linear stress-strain relationship [11]. Viscoelastic solids exhibit the behavior of both elastic and viscous materials, where the time-dependent recovery is not always reversible. The Kelvin element shown in Figure 1.1(c) is an example of a viscoelastic model; however, many combinations of springs and dampers in series and parallel have been used to describe the mechanical behavior of cells [1, 11]. Power-law models describe the stress-strain relationship in a power-law form and work well for modeling the creep and stress relaxation behavior of cells, particularly when multiple time constants are present in the cell relaxation response [13].

Conventional Single-Cell Characterization Methods This review focuses on microfluidic devices that deform cells based on channel wall-cell interactions; however, a brief overview of well-established techniques for the mechanical characterization of cells is outlined here. Additionally, emerging techniques that integrate well with microfluidics are mentioned for completeness.

Atomic force microscopy (AFM) is a high-resolution imaging technique that involves scanning a cantilever with a sharp tip over a sample surface, measuring the interaction forces between the tip and the sample to create a detailed topographic map of the surface, with a pixel size dependent on the tip size and movement increment [14]. AFM can be performed in several force-sensing modes, but the most common method for mechanical characterization

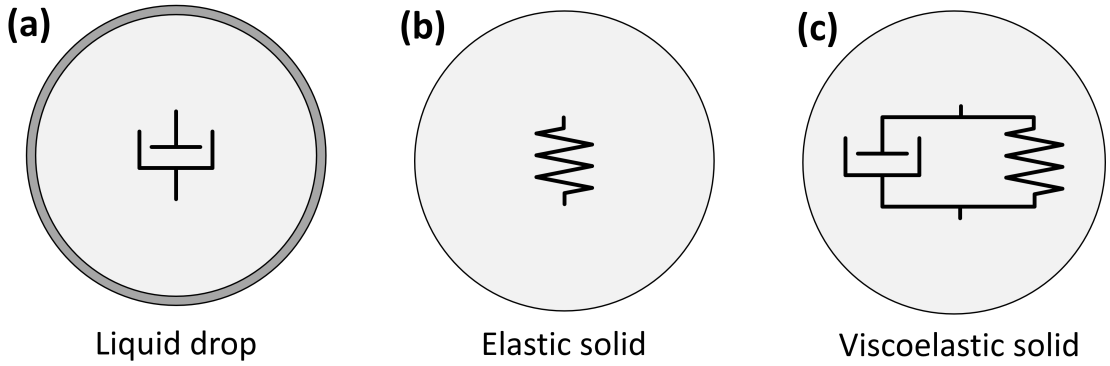


Figure 1.1: Examples of cell mechanical models. (a) The liquid-drop model has a thin membrane with constant tension encapsulating a liquid with a defined viscosity. Other forms of liquid-drop models include shear-thinning liquids and compound drops. (b) The elastic solid model represents the cell as a homogeneous, elastic solid which can be modeled with both linear and nonlinear springs. (c) The viscoelastic solid model defines the cell as a homogeneous, viscoelastic solid that can be modeled with multiple springs and dampers in series and parallel combinations.

of cells is the application of a preset force or deformation to the cell with the cantilever tip and measurement of the resisting force of the cell [15]. A laser beam is used to measure the deflection of the cantilever, and a 3D mapping of the surface is attained by precisely moving the cantilever with piezo stages. This produces a map of local cell mechanical properties, such as Young's modulus, but non-sharp cantilever tips, such as spheres, can also be used to produce global (average) cell properties [16]. It is possible for AFM to operate in fluids to provide a more natural environment for cells, but cells are typically adhered to a substrate before characterization to prevent cell migration or movement induced by the cantilever tip [17]. Although many mechanical models have been used to interpret AFM data, the linear elastic model is often implemented owing to its simplicity [18, 19]. AFM is a powerful mechanical characterization technique because of its high spatial resolution and precision; however, the two drawbacks of this technique are its high cost and low throughput.

Optical Tweezers (OT) are another high-resolution technique for cell mechanical characterization, in which a highly focused laser beam is used to trap and manipulate cells

[20, 21]. This technique relies on the radiation pressure and momentum of photons on a cell near the focus of the laser beam to create a 3D gradient trapping force [22]. The trapping light scattered by the cell is used to determine the external forces on the cell along with its position, which enables the measurement of global cell properties such as stiffness. To measure local properties, dielectric microparticles, such as polystyrene beads, are used to probe the exterior of cells, and the cell interior is mechanically characterized by injecting microspheres inside the cell [23]. Cell deformation (strain) can be used as a metric to compare cells, and several mechanical models, including viscoelastic models, have been applied to extract cell mechanical properties [24]. OT works well in combination with microfluidics and has been used in other applications such as cell sorting. As with AFM, OT systems are expensive and have a low throughput [25].

Micropipette aspiration is a well-established technique in which the surface of a cell is gently aspirated into a circular pipette with a diameter less than that of the cell of interest [26]. A typical micropipette aspiration apparatus consists of a glass pipette mounted on a micromanipulator, which brings the pipette near the cell. A well-defined negative pressure in the range of 1 Pa-100 kPa was supplied by a pressure controller to gently force the cell into the pipette. The deformed cell was viewed with an imaging system to track how the cell deforms as a function of time. Various mechanical properties, such as Young's modulus or viscoelastic relaxation time, can then be extracted, given the known pressure and measured cell deformation, depending on the mechanical model chosen [8]. Although partially automated systems have been developed to decrease the time and skill required, the throughput of this method is low, typically less than 10 cells/h [27]. Given its relative simplicity, micropipette aspiration has been adapted for microfluidic integration, as described later.

Microfluidic Integrated Methods In dielectrophoresis (DEP), cells are deformed by interacting with a non-uniform electric field [28]. DEP is widely used in cell sorting, trapping, separation, and electrical characterization assays [29–31], but it can also be used to deform single cells [32, 33]. The applied force is estimated through DEP theory and simulation, and the resulting strain is observed using an imaging system. From there, the data can be fitted into various mechanical models to estimate the cell properties [34, 35].

Acoustic force spectroscopy (AFS) is a method for manipulating cells using planar acoustic standing waves in a flow cell [36]. Similar to some OT operating modes, microspheres can be precisely manipulated with AFS, which in turn are used to deform DNA [37] or cells [38] to measure their mechanical properties. Although it is possible to parallelize cells to increase throughput, as in [39], the initial setup takes time and is not easy to repeat.

Magnetic tweezers (MT) apply controlled forces and torques to magnetic beads or particles that are tethered to biomolecules [40, 41] or cells [42]. MT has also been incorporated into microfluidic devices for mechanical characterization of cancer cells [43]. High-throughput MT in microfluidics for the mechanical characterization of cells has yet to be demonstrated.

Micro-electrical-mechanical systems (MEMS) are a well-developed technology consisting of microfabricated sensors, actuators, and transducers. A MEMS-based cell squeezer was developed by Warnat et al in a series of publications [44–46] where they measured several mechanical properties of yeast cells, including mechanical stiffness. Cells were suspended in a buffer solution and pipetted onto the device, and a MEMS actuator was used to compress the placed cell and a reference spring, allowing the stiffness of the cell to be determined. Although the cell deformation and stiffness were determined with high precision, loading the cells in place was tedious and not easily repeatable. Takayama et al [47] fabricated a device with similar working principles, but importantly, they could integrate it with a microfluidic channel. The cells were positioned between the actuator and reference spring by

a controlled flow, making cell positioning much less difficult. Although these devices provide precise measurements, the throughput will always be limited because of the difficulty of parallelizing the actuators, as the driving structures are large compared to the actuator and spring tips.

Passive Microfluidics

In this review, passive microfluidic devices refer to channels with a static geometry. Fluid flow and optical imaging can be dynamically controlled, but the channels are static. Cells are deformed by contacting the walls or the fluid within which they are suspended. Examples of passive microfluidics in this paper are single-cell characterization techniques. Some examples also integrate electrical or optical characterization, but this is outside the scope of this review.

Microfluidic Micropipette Aspiration Micropipette aspiration is a conventional mechanical characterization technique that was readily adapted to microfluidics [48]. The circular pipette is replaced with a rectangular PDMS-glass channel, as shown in Figure 1.2(a). Microfluidic channels are used to get the cells into the pipette (constriction) area, greatly decreasing cell handling times compared to the conventional technique. Cell deformation in the pipette area is monitored using a microscope. A well-defined pressure that forces the cell into the constriction is critical for mechanical analysis.

One of the first examples of microfluidic micropipette aspiration was demonstrated by Chen et al [49], who reported Young's modulus of MC-3T3 osteoblast cells using a common linear-elastic model [50]. They also described one challenge of this technique: the rectangular pipette channel does not allow the cell to form a perfect seal, possibly allowing pressure to leak around it. They posited that this may have led to a Young's modulus measurement lower than those obtained using the conventional circular glass pipette method. Guo et al [51] fabricated a PDMS device with a series of funnel constrictions of decreasing

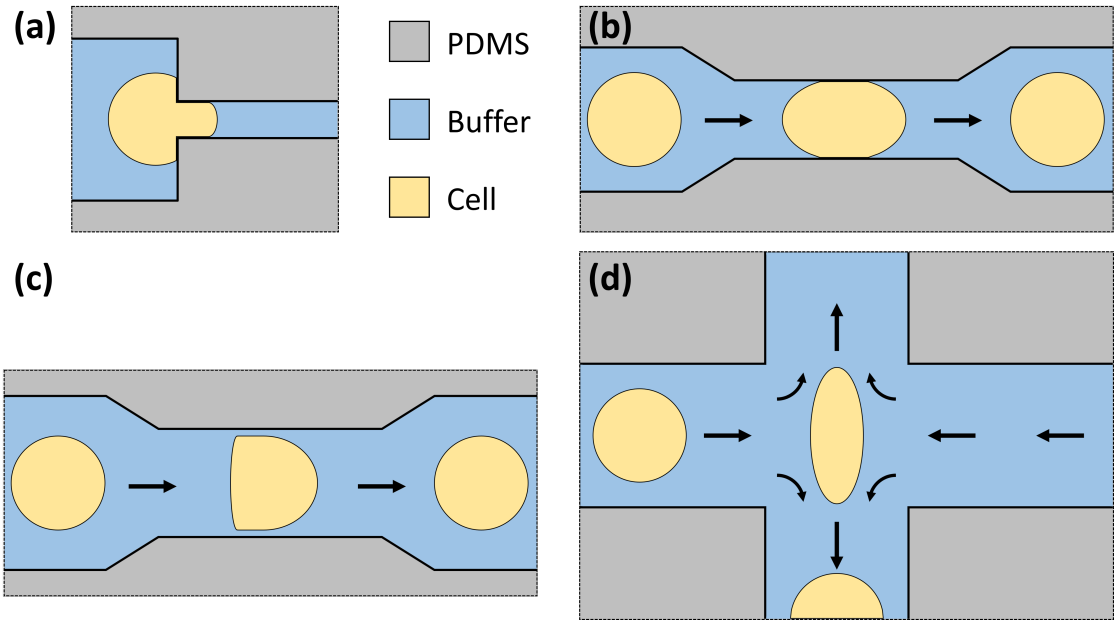


Figure 1.2: Passive microfluidic methods for mechanical characterization of cells. (a) Microfluidic micropipette aspiration, in which a cell is forced into a narrow constriction by applying pressure. (b) Constriction deformability cytometry operates similarly to microfluidic micropipette aspiration, but the constriction only slightly deforms the cell, so the passage time is quicker. (c) Shear deformability cytometry, where cells are deformed into a bullet shape by the fluid shear stress resulting from channels that are slightly larger than the cells. (d) Extensional deformability cytometry where cells are compressed and elongated by perpendicular flows.

size to help achieve optimal cell compression in their whole-cell microfluidic micropipette aspiration device. Using a liquid-drop mechanical model, they reported the cortical tension of passive human neutrophils, human lymphocytes, human bladder cancer cells, and mouse lymphoma cells, with a throughput of 30 cells/h. Lee et al [52] fabricated a PDMS device with parallelized pipette channels to increase the measurement throughput of micropipette aspiration. When unobstructed, cells preferentially travel through the short pipette channels owing to their lower fluidic resistance. However, using this method, cells need to be close to the wall containing the perpendicular pipette channel to be trapped, which results in poor trapping efficiency and potentially long capture times. Lee et al [53] updated their

design to include PDMS-membrane microvalves to decouple cell trapping and aspiration, allowing for more accurate mechanical measurements. Additionally, they achieved 100% trapping efficiency (26 pipette channels) in approximately 10 s, compared to their previous design, which required several minutes to trap cells. Using a Newtonian liquid-drop model, they found the Young's modulus of breast cancer MDA-MB-231 cells to be lower than that previously reported, but hypothesized that this was due to different cell culture conditions.

Davidson et al [54] measured the viscoelastic mechanical properties of human fibroblasts and tumor cell nuclei with another parallelized, 18-channel, PDMS microfluidic micropipette-aspiration device. A power-law model and several viscoelastic models were used to fit the data. They discussed the possibility of adding more channels to their design but stated that more channels result in less uniformity in terms of pressure. Another potential drawback, as in [52], is that cells in the main microfluidic channel can interact with trapped cells undergoing aspiration, making mechanical analysis more difficult. For cells with easily deformed nuclei, the authors reported a throughput of 100 cells/h, at least an order of magnitude higher than that of the conventional micropipette aspiration [54]. Boot et al [55] described a similar PDMS device with eight pipette channels in parallel and characterized cell spheroids using a viscoelastic-solid model. They discussed the potential problems of a pressure drop over microfluidic tubing and attempted to mitigate this effect by stopping the flow before aspiration, thus relying on static-hydrodynamic pressure for aspiration.

Deformability Cytometry In recent decades, cell deformability cytometry has emerged as a powerful tool for mechanically characterizing cells [56, 57]. This technology is essentially a tool for measuring cell deformability in microfluidic channels at high throughput, and has frequently been applied to study cancer cell stiffness changes. Deformability cytometry can be divided by the method of deforming cells: constriction, fluid shear, and extensional deformability cytometry, as shown in Figure 1.2(b-d), respectively [57, 58]. While

deformability cytometry can be extended to measure the direct mechanical properties of cells, such as the Young's modulus, many of the following examples focus on comparing and distinguishing different cell populations based on their deformability in a particular microfluidic device.

In constriction deformability cytometry (cDC), as shown in Figure 1.2(b), cells are deformed by constriction channels smaller than the cells. Compared with microfluidic micropipette aspiration channels, cells are less strained and quickly pass through the constriction. Hou et al [59] investigated breast cancer cells and compared the deformability of cancerous and benign cells using a PDMS constriction device. They measured the entry time, elongation index, and transit velocity of cells in the constriction area and found that cancerous MCF-7 cells were softer than benign MCF-10A cells based on entry times. Importantly, the two cell lines had similar transitive velocities after the channels were coated with 4% bovine serum albumin (BSA), which showed that the friction between cells and the channel walls was similar between the cell lines.

Comparing the results from different cell lines and microdevices is challenging because of the measurement dependence on cell size and friction properties. To explore the deformability-friction interaction, Byun et al [60] designed a suspended microchannel resonator (SMR) to measure the cell mass, entry velocity, and transitive velocity in the constriction area of a microfluidic channel. The SMR consisted of a microfluidic channel with a constriction area embedded in a silicon cantilever, whose resonant frequency was detected by the deflection of a laser beam. The cell mass and position were measured by detecting changes in the resonant frequency of the cantilever. Experiments with human epithelial cells and red blood cells showed that both cell deformability and friction influenced entry and transitive velocities, but friction had a greater influence on passage time. To measure the pressure drop caused by a cell transversing a constriction area, Khan et al [61] created a microfluidic manometer device with separate but identical test and reference

constriction channels. Although they could not distinguish between cancerous and benign brain cells based on passage time, elongation, or pressure drop, they concluded that the entry time was the most sensitive parameter. Luo et al [62] used a high-speed camera to record how cells deformed on entry into the constriction area to further explore cell entry time. They found that cells aspirated into the constriction in two stages, and by incorporating results from their simulations, they extracted the instantaneous Young's modulus and friction coefficient using an incompressible visco-hyperelastic solid model. Lange et al [63] increased the throughput of the constriction channel method by fabricating a microfluidic device with eight parallel constriction channels and achieved a throughput of 100's cells/min. Nyberg et al [64] calibrated the mechanical stresses experienced by cells transversing a constriction area using gel beads. They found that time-dependent strain followed a power-law model and determined the apparent Young's modulus and power-law exponent for human promyelocytic leukemia (HL-60) cells. In a later work, Nyberg et al [65] characterized six cell lines with the same method with a throughput of 100's of cells/s. Similarly, Chen et al [66] use a power-law rheology model to quantify the elasticity of cells and in a following article, described in detail how to fabricate and operate their microfluidic device [67].

Fluid shear deformability cytometry (sDC), shown in Figure 1.2(c), is a contactless approach, as the cells do not contact the channel walls, eliminating the channel wall-cell friction interaction. Instead, cells are deformed in a characteristic bullet-like shape by hydrodynamic shear stress resulting from the parabolic velocity profile of the fluid [57, 68]. Finite-element simulations incorporating linear-elastic and hyperelastic solid models were developed to predict the size-dependent cell shape during deformation [68, 69]. sDC was demonstrated by Otto et al [70] with a PDMS microfluidic channel and high-speed camera to quantify cell deformation D, defined as D = 1 – circularity, in real time, at a rate of 100 cells/s, and referred to their method as real-time deformability cytometry (RT-DC). By incorporating simulation results for shear stress and pressure on the cell, lines of constant

elastic modulus were displayed on a cell size vs. deformation graph. Their experiments showed that the label-free method was sensitive to cytoskeletal alterations, and they could distinguish cell cycle phases, track stem cell differentiation, and mechanophenotype cell populations in whole blood samples. Another iteration of the device characterized human leukemia HL-60 cells with a throughput of 1000's cells/s [71]. Clogging problems reportedly render approximately 10% of these devices unusable [70]. To address these clogging issues and potentially increase throughput, Ahmmed et al [72] presented a parallelized RT-DC device, which they called multi-sample deformability cytometry. In this method, 10 parallel channels were used to characterize multiple cells simultaneously with a throughput of 100 cells/s. Although this device was less affected by clogging issues owing to the parallel channels, the throughput was lower than that of previous RT-DC devices because the increased camera field of view limited the frame rate and, in turn, the maximum cell velocity.

Clustering and statistical analysis of deformability measurements for comparing and isolating cell populations are discussed in [73]. Fregin et al [74] determined viscoelastic cell parameters independent of cell shape, enabling the investigation of non-spherical cells. RT-DC continues to be applied at high throughput [75] and have also been integrated with fluorescence imaging [76]. As flow stability is a concern in sDC, higher-viscosity fluids are typically employed [76].

Extensional flow deformability cytometry (xDC) is another contactless method in which cells are deformed by fluid interactions, as shown in Figure 1.2(d) [57]. Unlike sDC, xDC uses cross-shaped channels with the applied flow in symmetric, opposing channels, with the two perpendicular channels allowing fluid to escape. The cells are compressed and elongated by the inlet and outlet flows in the center of the cross, and imaged using a high-speed camera. The strain experienced by the cells in the center cross is larger than that experienced in cDC and sDC [58]. A representative work was performed by Gossett et al [77] with a PDMS device and a high-speed camera system capable of quantifying deformability with a throughput of

2000 cells/s.

Further work has explored cell deformation kinetics, morphology, and other cell properties that could be extracted with xDC [78, 79]. Compared with sDC, xDC does not require high-viscosity fluids and can operate faster, providing access to a high-speed camera with a frame rate capable of capturing cell deformation. However, adjusting the fluid viscosity enables control of the applied strain rate experienced by the cells [80, 81]. Optics-free approaches to xDC have also been developed to measure cell deformability using electrical impedance sensor integration, although with a much lower throughput of 300 cells/s [82].

Active Microfluidics

Active microfluidic devices in this review refer to channels with non-static geometry. Fluid flow may be dynamically controlled, as in passive methods; however, the channel dimensions can be changed. A moving wall of the microdevice typically deforms cells. Examples include both single- and bulk-cell characterization techniques. Like the examples in deformability cytometry, these devices are utilized for comparing the mechanical responses of cells to deformation rather than measuring a mechanical property that fits the mechanical model of a cell.

Flow-through PDMS Membranes The use of thin PDMS membranes for microfluidic valves is well established [83, 84]. Several examples have used these membranes to actively deform cells, as shown in Figure 1.3(a-b). Westendorf et al [85] presented the design and fabrication of single- and double-layer PDMS membrane devices for live-cell flattening and compression. In single-layer PDMS devices, fluid is withdrawn from the channel exit to create a pressure difference that deforms the thin channel ceiling. In double-layer devices, a separate channel is pressurized to deform the PDMS membrane, which divides the actuating and lower channels. Double-layer channels are more complex to fabricate but can control

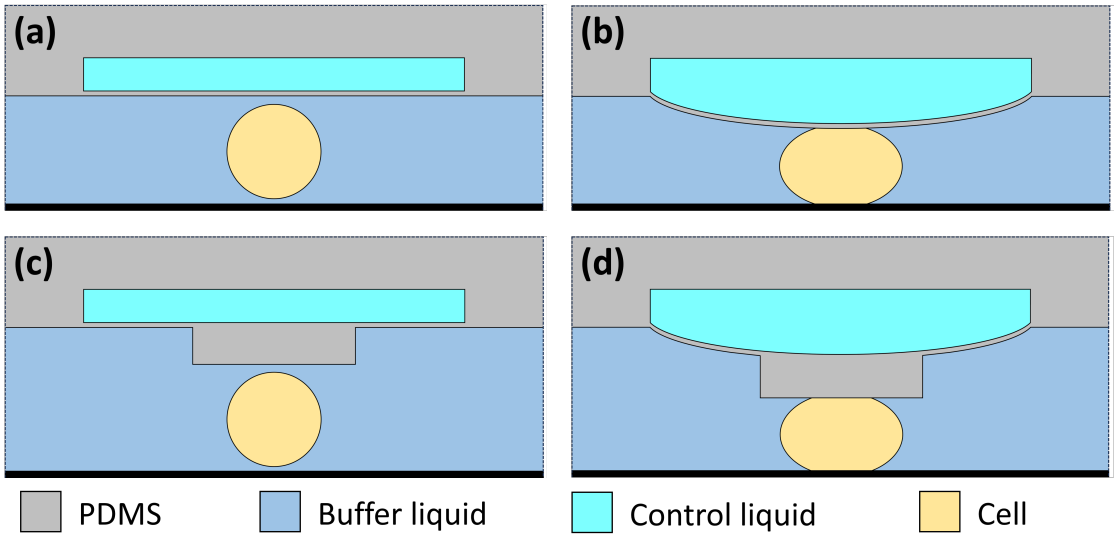


Figure 1.3: PDMS membranes for cell deformation. Typically, a membrane is deformed by a pressurized channel, called the control channel. The control channel is often filled with water because PDMS is air-permeable at elevated pressures. (a) Single-layer PDMS membrane. (b) Single-layer PDMS membrane deformed by a pressurized control channel. (c) Double-layer PDMS membrane. (d) Double-layer PDMS membrane that remains flat in the region where it contacts the cell.

the lower channel height independently of the flow rate. Du et al [86] fabricated a double-layer microfluidic device with two channels separated by a 500 µm thick PDMS membrane; one channel was loaded with cells suspended in a buffer solution, and the other channel was pressurized with water to deform the membrane and cells underneath [86]. The cells were positioned below the membrane and observed using a microscope. The membrane was deflected to deform the cells and then released while imaging the cells recovering to their undeformed state. They measured the viscoelastic recovery time of 3T3 fibroblasts and HL-60 cells by fitting the projected area to a homogeneous linear-viscoelastic model. Using a similar device, Yokokura et al [87] measured the apparent Young's modulus of spherical osteoblasts deformed by a PDMS membrane. They assumed that the top and bottom of the cells in contact with the PDMS membrane and glass coverslip, respectively, were flat, and the sides were hemispherical, so that they could relate the projected diameter

of the cells to the applied longitudinal strain. The stress exerted by the membrane was measured with a pressure sensor connected to the control channel, and this stress was used to determine the Young's modulus assuming linear-elastic behavior. Ho et al [88] compressed and aspirated artificial cells (water in oil double emulsion drops) using a PDMS microfluidic device previously described for microfluidic micropipette aspiration [52]. They showed that the middle oil phase was thinned by compression using a PDMS membrane and micropipette aspiration channels, which allowed them to mechanically regulate the transport of calcium ions to the inner aqueous phase. Robinson et al [89] used PDMS ring valves to trap model cells (giant unilamellar vesicles, or GUVs) underneath a PDMS membrane capable of applying unidirectional compression. They found that water efflux prevented membrane rupture, reorganized multicomponent phase-separated GUVs, and fused membrane domains under compression. Rather than a deforming ceiling, Shorr et al [90] developed a mesofluidic device with thin walls, 50-150 µm thick, deflected by adjacent pressurized channels, similar to previous examples. They were able to apply compression to hundreds of Drosophila embryos in parallel and measured Young's modulus of the embryos using an analytical model of PDMS wall deflection. Compared to previous examples, this device can equally deform many cells in parallel, but it is only possible because of the large channel height of approximately 200 µm.

Single-layer PDMS membranes exhibit a non-planar deflection; therefore, only the deformation applied to single or several cells is fairly uniform. Several groups have utilized multi-layer PDMS membranes to achieve planar, uniform deflection, as shown in Figure 1.3(c-d). Onal et al [91] designed a cell culture chamber for applying compression to cells using a micropiston. The structure was formed as a PDMS membrane of 300 µm diameter (or similarly sized square and triangular shapes) with a 200 µm tall block of PDMS bonded onto it. Cell viability was monitored before and after cyclic mechanical compression. Onal et al [92] extended this work by studying SKOV-3 ovarian cancer cell response to cyclical

compressions. They concluded that cell recovery depends on the magnitude of the applied compression; cell membrane bulges immediately after compression appeared as increased actin signals, and changes were recorded in mechanosensitive subcellular structures such as the actin cytoskeleton and nuclei during the 24 h post compression. Instead of a multi-layer membrane, Kim et al [93] bonded a single-layer PDMS membrane to a hemispherical PDMS well supported by a glass coverslip. The membrane could compress all the cells in the well simultaneously, but it did not result in uniform compression of the cells owing to the non-uniform deflection of the membrane. MCF7 human breast cancer cell viability was studied during and after applying static compression force.

Non-flow-through Devices Hsieh et al [94] developed a non-flow-through PDMS membrane device for studying cell-laden gradient strain hydrogels. The exit port of the device was plugged, and the uncured cell-hydrogel suspension was injected into the device to deform a circular PDMS membrane. The hydrogel was cross-linked by UV irradiation in a concentric ring pattern and the uncured hydrogel was flushed out. The plug was removed, and the PDMS membrane deflected back to its undeformed state, resulting in static compressive and radial strain to the hydrogel rings confined underneath, with maximum strain on the inner ring and decreasing away from the center. A device was used to monitor the viability of 3T3 fibroblasts over time. Rather than confine cell-laden matrix within channels of a PDMS device, Lee et al [95] created a device for applying compression to chondrocyte cells suspended in a block of alginate matrix attached to an external glass slide. The alginate block was clamped to the top of the PDMS membrane device, and the internal channels were pressurized to deform the thin PDMS membrane and alginate-chondrocyte constructs. Cell deformation from static compression was measured using a microscope, and dynamic compression (1 Hz) was applied to the cells to test cell viability under mechanical loading. Ahn et al [96] fabricated a platform to culture a 3D perfusable *in vitro* blood vessel and

applied compressive stress to the engineered vascular tissue with a PDMS membrane. The tissue exhibited several complex histological reactions to biomechanical stress, including formations of "dead zones," increased reactive oxygen species (ROS) levels, and increased vessel leakiness. Another example of cells cultured inside a device is the work of Paggi et al [97], where a PDMS membrane mechanically stimulated chondrocytes suspended in an agarose matrix inside the device. Chondrocytes remained viable after applying static and dynamic strain conditions; however, hyperphysiological stimulation caused cell membrane rupture and cell death. While non-flow-through devices are advantageous for maintaining certain cells, such as chondrocytes, in a more natural matrix environment, the throughput of these devices can not match the passive and active flow-through methods.

Another non-flow-through device is described in a sequence of US patents [98–100]. Cells mixed with rigid microspheres are dispensed onto a CMOS imager and the sample confined between the imager and a glass plate. The glass is lowered to be in contact with the microspheres and compress the cells were are slightly larger in comparison. A light source placed above the glass completes the massively parallel near-field imaging system. The main benefit of such a device is the large FOV achieved by imaging cells directly on an image sensor.

Comparing Passive and Active Methods

Microfluidic micropipette aspiration can measure elastic and viscoelastic cell properties by fitting the pressure and cell deformation to mechanical models. However, some questions remain regarding the accuracy of these measurements due to the non-circular cross-section of the constriction channel and estimation rather than the direct measurement of pressure. Deformability cytometry measures many variables, such as circularity, deformation time, and passage time, and it is possible to apply mechanical models and simulation results to fit properties, such as Young's modulus, to cells. However, these measurements are

most useful for qualitatively comparing cells, such as cancerous and healthy cells. In active methods, there are examples of measuring Young's modulus and viscoelastic recovery time by fitting deformation to mechanical models. However, instead of measuring mechanical properties, active devices are used to investigate how cells respond to mechanical stimulation. Cell viability is the most tracked metric; however, there are also examples of exploring mechanotransduction by tracking gene expression. While both passive and active methods can measure the mechanical properties of cells, passive methods focus more on comparing cell mechanical behavior, while active methods focus more on studying cell response to dynamic mechanical stimuli. In general, passive devices define the strain applied to cells based on the channel size, whereas active devices define the stress or strain applied to cells based on the pressure in the control channel.

The throughput of passive devices, particularly deformability cytometry, is currently the highest of any developed microfluidic method, on the order of 1000 cells/s. While microfluidic micropipette aspiration is similar to cDC, the throughput is significantly limited because the constriction channel size is typically significantly smaller than that of cDC, resulting in longer aspiration times. One advantage of this longer aspiration time is that a high-speed camera is not required for microfluidic micropipette aspiration, which increases its applicability in the scientific community (high camera costs). Additionally, microfluidic micropipette aspiration devices only characterize a few cells from the suspension, whereas deformability cytometry methods can measure every cell that transverses the device. The xDC method has proved the fastest among the deformability cytometry methods for a single measurement channel; however, parallelizing the channels is simpler with the cDC and sDC methods. Compared to passive devices, active device throughput is typically very low and is often not stated in publications. A possible explanation for the low throughput is that precise deflection of the channel wall is difficult to achieve quickly. Compared to the cells of interest, the channel walls and control channels are several orders of magnitude larger.

Fabricating single-layer PDMS devices, commonly used in passive methods, is a relatively simple process if access to a cleanroom facility is possible [101]. Multi-layer PDMS devices commonly used in active methods add the complexity of aligning and bonding multiple PDMS layers together. Thin PDMS membranes 35-500 µm thick are reliably produced by spin-coating uncured PDMS before crosslinking. Because PDMS is air-permeable at elevated pressures, active devices with PDMS membranes typically fill pressurized control channels with water. In the referenced articles, the groups used several chemicals to inhibit and promote cell-to-PDMS attachment. From an operational perspective, in passive constriction channels, cell clogging is a prevalent challenge, whereas in active devices, the challenge is cell attachment, designed or incidental, which makes cell removal difficult. In the latter case, the unremoved cells do not necessarily inhibit the device's usability and allow the devices to be reused. For passive devices, particularly sDC and xDC, ultra-stable flow rates and pressures are necessary for measurement accuracy. This can be addressed with more expensive pressure-driven flow systems or low-flow-rate-specific syringe pumps. In active devices, device calibration is critical for repeatable cell deformations. Fluorescent transmission intensity, confocal microscopy, and white light interferometry (WLI) are examples of tools used to calibrate channel-wall deflection.

Scaling up passive throughput devices is possible by increasing the cell velocity, which requires increasing the camera frame rate or parallelizing constriction channels. Examples of parallelizing channels were referenced for each passive method. However, there is a balance between the imaging field-of-view (FOV) and frame rate. The larger the FOV for a given pixel size, the greater the memory and processing power required by the camera system. Increasing the image pixel size by reducing the optical zoom saves memory, but costs image resolution, which is important for referenced passive microfluidic methods. The same tradeoff can be made in many active microfluidic methods; however, there is an additional consideration. Passive constriction channels need to confine the cell in two dimensions so that cells only

interact with the fluid and wall and not with neighboring cells, but active devices need only to deform cells in one dimension in the typical case where cells are stationary under deformation. Rather than making parallelized wells for single cells, a single deflecting surface can apply deformation to many parallelized cells, provided the surface can apply uniform deformation across a large area, and the cells are not physically touching.

Chondrocytes

Chondrocytes are specialized cells embedded in articular cartilage, which lines the ends of bones in diarthrodial joints. The cartilage provides cushion and lubrication between load-bearing joints and is mainly comprised of extracellular matrix (ECM) [102]. Chondrocytes maintain the ECM [103] and produce a pericellular matrix (PCM) that surrounds them and plays a role in mechanotransduction [104]. Changes to the metabolic state of chondrocytes have been linked to the onset of osteoarthritis (OA) [105], a common chronic disease affecting more than 300 million people worldwide and posing a significant economic burden on patients and healthcare providers [3, 106]. Because of the substantial impact of OA, research must be done to understand further the role of chondrocytes in maintaining articular cartilage. OA human chondrocytes are relatively easy to obtain due to the large number of joint replacements surgeries, but healthy human articular cartilage is much rarer, so cartilage from (presumably healthy) bovine is a close substitute to use as a control for experimentation [107].

Typically, this work requires harvesting cells from cartilage (human, bovine, etc.) and culturing the cells in the lab to produce the necessary number of cells for *in vitro* experiments [108]. Problematically, it is known that chondrocytes dedifferentiate under standard monolayer culture conditions and lose the round morphology associated with the *in vivo* phenotype [109]. Recent work has developed a culture system where both primary OA human and healthy bovine chondrocytes are cultured in alginate beads with the addition

of sodium L-ascorbate resulting in "chondron", chondrocytes with a complete PCM shell. It has been shown that the stiffness of the PCM of chondrocytes is reduced by OA [110, 111]. Additionally, the viscoelastic recovery time of chondrocytes differs between healthy and OA cells [112, 113].

Importantly, it has been shown that the mechanical properties of chondrocytes, including relaxation time, are different between healthy and OA chondrocytes suggesting that relaxation time is a viable biomarker for OA disease in chondrocytes [112, 113]. In addition, chondrocytes' mechanical properties also change with age [114]. These cells have also been shown to be sensitive to loading conditions [115]. Typically, these cells are harvested from articular cartilage and cultured in monolayers in the lab to produce cells for *in vitro* experimentation [108]. However, cells cultured this way do not mimic *in vivo* conditions where a pericellular matrix surrounds cells. Work has shown that encapsulating primary chondrocytes in alginate with the addition of sodium L-ascorbate during the culture process produces cells with a PCM, which better mimics the *in vivo* phenotype [116]. It seems probable that this PCM contributes to the viscoelastic properties of the cells. Due to the amount of published research and active interest in chondrocytes, they are an ideal cell for benchmarking and validating the capabilities of this device.

Knowledge Gaps

Single-cell mechanical phenotyping has promising applications in science and healthcare [117]. Cell mechanical properties can be used as biomarkers for diseases such as cancer and osteoarthritis (OA) [112, 118–120]. Mechanical phenotyping is label-free, meaning it doesn't require inconvenient and costly pretreatment of samples and is therefore preferred over biochemical phenotyping when feasible. However, exploiting these mechanical biomarkers is challenging with the available technology for mechanical characterization of cells which are generally low-throughput, mainly due to the difficulty of cell handling. Increasing throughput

beyond 10 cells/h is essential for practically implementing mechanical phenotyping of cells. Solving this problem requires the development of new technologies which decrease cell handling times and increase measurement throughput.

It has been demonstrated that the mechanical properties of cells change when they become diseased with cancer or OA, and this change can be used as disease biomarkers. Mechanical biomarkers are label-free, so they do not require slow and costly sample labeling and therefore are advantageous to more traditional biochemical biomarkers such as fluorescently-labeled antibodies [119]. However, the existence of a biomarker is only truly useful if exploited in a timely, cost-effective manner. More recent studies into mechanical biomarkers have illustrated their potential. Yet, there remains a need to advance scientific knowledge and technologies in this area as measurement strategy and efficiency still need to be improved.

A major drawback of conventional techniques is low-throughput, where it may take hours to measure just 10 cells [2, 8]. The high precision of methods such as AFM and OT is invaluable for a more thorough scientific understanding of cell mechanics. However, given the previously mentioned heterogeneity of cells in a population, and the large number of cells required to build statistically significant data, higher-throughput measurements are preferred and needed for practical applications.

Cells, specifically chondrocytes, are viscoelastic materials that exhibit a viscoelastic recovery time after undergoing deformation. Elastic moduli and viscosity of the cell influence this property. Presently, no work to the author's knowledge has shown the ability to measure this property in a high-throughput manner. While previous research has utilized low-throughput techniques for mechanical characterization, this research will develop a high-throughput characterization method using microfluidics.

Research Goals, Hypotheses, and Objectives

Broadly, this work aims to use microfluidics for mechanical characterization of cells. Specifically, this work aims to evaluate the elastic, viscoelastic, and viscous recovery of chondrocyte cells strained by a glass plate and compare bovine and primary chondrocytes from monolayer and alginate cultures. **The overarching goal** of this work is to develop a 3D-printed variable-height fluidic channel for the viscoelastic characterization of round cells with a measurement throughput of 50 cells/h. **The central hypothesis** is that a 3D-printed variable-height flow-cell is capable of viscoelastic characterization of chondrocyte cells. To test this hypothesis, a 3D-printed fluidic channel with a variable-height channel is designed and fabricated, and chondrocytes are mechanically strained, and their recovery is observed with confocal microscopy. The projected cell area is fit to a viscoelastic mechanical model to extract parameters such as viscoelastic recovery time.

To support the overarching goal of developing a 3D-printed variable-height fluidic channel, three objectives are considered:

Objective 1: Develop a 3D printing method for producing fluidic channels directly on a glass substrate. 3D printing is a versatile additive manufacturing technology. However, making fluidic channels that can be observed with a microscope is challenging because even optically transparent resins obscure microscopy due to their inherent surface roughness. This objective aims to overcome this challenge by fabricating channel structures directly on glass.

To address this objective, glass slides are treated with bind-silane, and resin printing is done directly on the glass slide. This creates microfluidic channels with glass as one of the walls. To show that the silane treatment did not negatively affect the end use of the device, proof-of-principle applications of measuring solution conductivity and electrochemical impedance of planktonic bacteria cells are performed after printing channels on microfabricated thin-film sensors. These applications are shown to be successful. This

objective is investigated in Chapter 3. Once the 3D printing method was developed, the next step is to fabricate a variable-height fluidic channel.

Objective 2: Fabricate and demonstrate the utility of a microfluidic device capable of reproducibly compressing chondrocyte cells to a defined strain and image the cells relaxing as the strain is removed. This objective aims to show that the proposed device can measure the viscoelastic recovery time of chondrocyte cells specifically, as well as spherical cells in general.

The tasks involved in this objective are: (i) design and fabricate a microfluidic device with a variable height channel; (ii) implement a pressure system to control the height of the channel; (iii) set the channel height (which defines the strain based on cell size) with a pressure controller; (iv) compress and image chondrocytes as they recover towards their undeformed shape; (v) extract the projected area of cells during relaxation and fit them to a mechanical model to measure viscoelastic recovery time. These tasks are explored in Chapter 4. The next step is to use the device to compare chondrocytes from different culture methods.

Objective 3: Characterize chondrocytes from two culture methods to determine if the culture method alters the mechanical properties of chondrocytes and their surrounding PCM shell. This objective aims to determine if the viscoelastic recovery time of bovine and primary OA chondrocytes changes when chondrocytes are grown in 2D monolayer and 3D alginate cultures.

The device and methodology from objective 2 are utilized again but with different cells. Previously, bovine chondrocytes from a monolayer culture were investigated, but here, chondrocytes are cultured in monolayer and alginate cultures with sodium L-ascorbate to promote PCM growth. The PCM of bovine and primary OA chondrocytes from the two culture methods is fluorescently stained and used to track how cells recovered following deformation. It is concluded that the recovery time of bovine and primary OA cells is

dependent on the culture method. This objective is demonstrated in Chapter 5.

THEORY

Linear Viscoelastic Models

Linear viscoelastic mechanical models are commonly used to describe materials that exhibit elastic and viscous behavior under deformation. These models help capture time-dependent responses of materials, where the stress is proportional to the strain or rate of strain and the duration over which it's applied.

In the case of non-homogeneous materials like chondrocyte cells, several assumptions are required to use these models. The most obvious is that stress and strain must be linearly proportional. Another critical assumption is the superposition principle, where the summation of several applied loads is equivalent to the combined load; this assumption justifies using Laplace transforms, which can significantly simplify derivation and analysis. A third important assumption is that the viscoelastic properties of the material do not change with the rate of loading. Otherwise, the inclusion of nonlinear behavior is necessary. Lastly, it is assumed that material properties are invariant under isothermal conditions for simplicity.

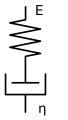
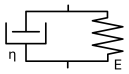
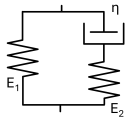
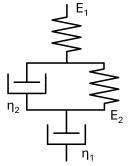
The spring and dashpot are the two essential mechanical elements in linear viscoelastic models. An elastic spring obeys Hooke's law, which states that the force exerted by a spring is proportional to its displacement from its equilibrium position. The key characteristics of an elastic spring are an instantaneous response to an applied force, potential energy storage that can be recovered entirely, and energy that can not be dissipated through a spring. A viscous dashpot describes the viscous behavior of a material where the force exerted by a dashpot is proportional to the displacement rate. A dashpot has no equilibrium position and has a flow-like response to an applied force. The key characteristics are a time-dependent response and energy dissipation. Table 2.1 shows the constitutive equations for spring and dashpot.

A creep-recovery experiment subjects a material to constant stress, while a stress relaxation experiment applies a constant load. Creep compliance is defined as the ratio of time-dependent strain to constant applied stress, while relaxation modulus is the time-dependent stress of the constant applied strain. Linear combinations of springs and dampers can describe various degrees of creep, recovery, and stress relaxation.

A parallel combination of a single spring and dashpot is called the Kelvin-Voigt solid, shown in Table 2.1. It helps describe creep behavior for a constant-stress experiment, where the material has an immediate elastic response due to the spring and a time-dependent strain due to the dashpot; upon removing the applied stress, the material returns to its undeformed state. This model can not describe stress relaxation. A series combination of a single spring and dashpot is called the Maxwell fluid model, shown in Table 2.1. This model can describe stress relaxation for a constant strain experiment and predicts an exponential stress decay over time. This model predicts an unbounded increase in strain for a constant stress experiment. When the stress is removed, the material does not return to its undeformed state.

When Kelvin-Voigt and Maxwell's models cannot describe a material, another popular choice is the Standard Linear Solid model, shown in Table 2.1. This model can explain creep and stress relaxation responses and predicts an instantaneous elastic response and a delayed, complete recovery to the undeformed state. This model can not be used to capture permanent, viscous behavior. A Burgers model combines a Kelvin-Voigt and Maxwell model in series, shown in Table 2.1. This model covers more behaviors than the Standard Linear Solid model because it can describe permanent, viscous behavior. Table 2.1 shows the previously mentioned mechanical models along with their constitutive equations. Also shown in the general recovery shape after an applied stress or strain. Note: the subscripts e, ve, and v represent elastic, viscoelastic, and viscous, respectively.

Table 2.1: Common linear viscoelastic mechanical models, including the corresponding constitutive equation, creep compliance, relaxation modulus, and general recovery equations.

Model	Name	Constitutive equation	Creep compliance	Relaxation modulus	Recovery
	Elastic Solid	$\sigma = E\varepsilon$	$\frac{1}{E}$	E	$\varepsilon = \varepsilon_e$
	Viscous Fluid	$\sigma = \eta\dot{\varepsilon}$	$\frac{t}{\eta}$		$\varepsilon = \varepsilon_v$
	Maxwell Fluid	$\sigma + \frac{\eta}{E}\dot{\sigma} = \eta\dot{\varepsilon}$	$\frac{1}{E} + \frac{t}{\eta}$	$Ee^{-(E/\eta)t}$	$\varepsilon = \varepsilon_e + \varepsilon_v$
	Kelvin-Voigt Solid	$\sigma = E\varepsilon + \eta\dot{\varepsilon}$	$\frac{1}{E}\left(1 - e^{-(E/\eta)t}\right)$	$E + \eta\delta(t)$	$\varepsilon = \varepsilon_{ve}e^{-t/\tau}$
	Standard Linear Solid	$\sigma + \frac{\eta}{E_2}\dot{\sigma} =$ $E_1\varepsilon + \eta\left(\frac{E_1+E_2}{E_2}\right)\dot{\varepsilon}$	$\frac{1}{E_1}\left(1 - \frac{E_2}{E_1+E_2}\right)e^{-t/\tau}$ where $\tau = \frac{\eta(E_1+E_2)}{E_1E_2}$	$E_1 + E_2e^{-t/\eta}$	$\varepsilon =$ $\varepsilon_e + \varepsilon_{ve}e^{-t/\tau}$
	Burgers Solid	$\sigma + \left(\frac{\eta_1}{E_1} + \frac{\eta_1}{E_2} + \frac{\eta_2}{E_2}\right)\dot{\sigma}$ $+\frac{\eta_1\eta_2}{E_1E_2}\ddot{\sigma} = \eta_1\dot{\varepsilon} + \frac{\eta_1\eta_2}{E_2}\ddot{\varepsilon}$	$\frac{1}{E_1} + \frac{t}{\eta_1}$ $+\frac{1}{E_2}\left(1 - e^{-(E_2/\eta_2)t}\right)$	Equation 2.19	$\varepsilon =$ $\varepsilon_e + \varepsilon_{ve}e^{-t/\tau} + \varepsilon_v$

Burgers Model Derivation

The following is a derivation of the Burgers model using Laplace transforms, briefly described in Appendix A. Looking at Figure 2.1, a system of equations can be written as

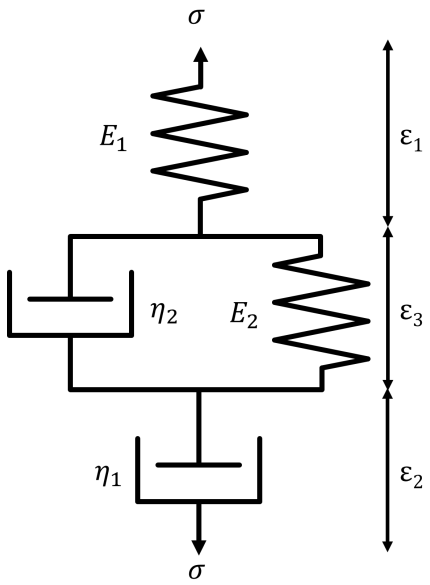


Figure 2.1: The Burgers mechanical model. The strain can be split into three components as shown. The stress in each component is equal to the total stress, as each element is in series.

Equation 2.1. Equation 2.1a is determined by considering the spring and dashpot of the Maxwell model as separate elements, and the Kelvin-Voigt model as a whole. Equations 2.1b-c are the strain in the spring and dashpot, respectively. Equation 2.1 is simply the constitutive equation of the Kelvin-Voigt model, listed in Table 2.1. This set of four equations with five unknowns can be used to eliminate ε_1, ε_2, ε_3 to find the Burgers constitutive

equation in terms of external stain, ε and stress, σ.

$$\varepsilon = \varepsilon_1 + \varepsilon_2 + \varepsilon_3 \tag{2.1a}$$

$$\varepsilon_1 = \frac{\sigma}{E_1} \tag{2.1b}$$

$$\dot{\varepsilon_2} = \frac{\sigma}{\eta_1} \tag{2.1c}$$

$$\dot{\varepsilon_3} + \frac{E_2}{\eta_2}\varepsilon_2 = \frac{\sigma}{\eta_2} \tag{2.1d}$$

The first step is to apply the Laplace transform to each equation, resulting in Equations 2.2a-d.

$$\hat{\varepsilon} = \hat{\varepsilon_1} + \hat{\varepsilon_2} + \hat{\varepsilon_3} \tag{2.2a}$$

$$\hat{\varepsilon_1} = \frac{\hat{\sigma}}{E_1} \tag{2.2b}$$

$$s\hat{\varepsilon_2} = \frac{\hat{\sigma}}{\eta_1} \tag{2.2c}$$

$$s\hat{\varepsilon_3} + \frac{E_2}{\eta_2}\hat{\varepsilon_2} = \frac{\hat{\sigma}}{\eta_2} \tag{2.2d}$$

Next, substitute Equations 2.2b-c into Equation 2.2a as shown below,

$$\hat{\varepsilon} = \frac{\hat{\sigma}}{E_1} + \frac{\hat{\sigma}}{s\eta_1} + \frac{\hat{\sigma}}{\eta_2\left(s + \frac{E_2}{\eta_2}\right)}, \tag{2.3}$$

and then multiply both sides by $\frac{\eta_1\eta_2}{E_2}s\left(s + \frac{E_2}{\eta_2}\right)$, rearrange, and finally perform the inverse laplace transform to get the constitutive equation,

$$\sigma + \left(\frac{\eta_1}{E_1} + \frac{\eta_1}{E_2} + \frac{\eta_2}{E_2}\right)\dot{\sigma} + \frac{\eta_1\eta_2}{E_1E_2}\ddot{\sigma} = \eta_1\dot{\varepsilon} + \frac{\eta_1\eta_2}{E_2}\ddot{\varepsilon}. \tag{2.4}$$

A creep experiment is the application of a constant stress, $\sigma = \sigma_0$ at $t = t_1$. The creep behavior is found by plugging the following initial conditions into the constitutive equation

(2.4),

$$\varepsilon = \frac{\sigma_0}{E_1}, \text{ for } t = 0 \tag{2.5a}$$

$$\dot{\varepsilon} = \frac{\sigma_0}{\eta_1} + \frac{\sigma_0}{\eta_2}, \text{ for } t = 0 \tag{2.5b}$$

resulting in

$$\sigma_0 = \eta_1 \dot{\varepsilon} + \frac{\eta_1 \eta_2}{E_2} \ddot{\varepsilon}. \tag{2.6}$$

Apply the Laplace transform,

$$\frac{\sigma_0}{s} = \eta_1 s \hat{\varepsilon} - \eta_1 \varepsilon(0) + \frac{\eta_1 \eta_2}{E_2} s^2 \hat{\varepsilon} - \frac{\eta_1 \eta_2}{E_2} s \varepsilon(0) - \frac{\eta_1 \eta_2}{E_2} \dot{\varepsilon}(0), \tag{2.7}$$

rearrange and simplify to get

$$\hat{\varepsilon} = \frac{1}{E_2/\eta_2 + s} \left[\frac{1}{s^2} \frac{E_2}{\eta_1 \eta_2} + \frac{1}{E_1} + \frac{1}{s} \left(\frac{\eta_1}{E_1} + \frac{1}{\eta_1} + \frac{1}{\eta_2} \right) \right] \sigma_0. \tag{2.8}$$

Now apply the inverse Laplace transform to finally get the creep equation,

$$\varepsilon = \frac{\sigma_0}{E_1} + \frac{\sigma_0}{\eta_1} t + \frac{\sigma_0}{E_2} \left(1 - e^{-(E_2/\eta_2)t} \right). \tag{2.9}$$

The creep recovery equation can be derived by adding a stress of $\sigma = -\sigma_0$ at $t = t_1$,

$$\begin{aligned} \varepsilon(t) = & \frac{\sigma_0}{E_1} + \frac{\sigma_0}{\eta_1} t + \frac{\sigma_0}{E_2} \left(1 - e^{-(E_2/\eta_2)t} \right) \\ & - \frac{\sigma_0}{E_1} + \frac{\sigma_0}{\eta_1} (t - t_1) + \frac{\sigma_0}{E_2} \left(1 - e^{-(E_2/\eta_2)(t-t_1)} \right) \text{ for } t > t_1 \end{aligned} \tag{2.10}$$

and can be simplified to

$$\varepsilon = \frac{\sigma_0}{\eta_1} t_1 + \frac{\sigma_0}{\eta_2} \left(e^{(E_2/\eta_2)t_1 - 1} \right) e^{-(E_2/\eta_2)t} \text{ for } t > t_1. \tag{2.11}$$

For a stress relaxation experiment a step strain of $\varepsilon = \varepsilon_0$ at $t = 0^+$ is applied, where $t = 0^+$ refers to the time immediately after the application of the strain. The initial strain

and time derivatives of strain are,

$$\varepsilon = \varepsilon_0 H(t) \tag{2.12a}$$

$$\dot{\varepsilon} = \varepsilon_0 \delta(t) \tag{2.12b}$$

$$\ddot{\varepsilon} = \varepsilon_0 \dot{\delta}(t), \tag{2.12c}$$

where $H(t)$ and $\delta(t)$ are the Heavyside and Dirac Delta functions, respectively. Plugging these equations into the constitutive equation yields

$$\sigma + p_1 \dot{\sigma} + p_2 \ddot{\sigma} = q_1 \varepsilon_0 \delta(t) + q_2 \varepsilon_0 \dot{\delta}(t), \tag{2.13}$$

with

$$p_1 = \frac{\eta_1}{E_1} + \frac{\eta_1}{E_2} + \frac{\eta_2}{E_2} \tag{2.14a}$$

$$p_2 = \frac{\eta_1 \eta - 2}{E_1 E_2} \tag{2.14b}$$

$$q_1 = \eta_1 \tag{2.14c}$$

$$q_2 = \frac{\eta_1 \eta_2}{E_2} \tag{2.14d}$$

Apply the Laplace transform to get

$$\hat{\sigma} = \frac{\varepsilon_0 \left(q_1 + q_2 s\right)}{1 + p_1 s + p_2 s^2}. \tag{2.15}$$

Partial fractions are required, so the roots of $p_2 s^2 + p_1 + 1$ need to be found,

$$\frac{\varepsilon_0 \left(q_1 + q_2 s\right)}{1 + p_1 s + p_2 s^2} = \frac{B}{s - z_1} + \frac{C}{s - z_2} \tag{2.16}$$

where

$$z_1 = \frac{-p_1 + \sqrt{p_1^2 - 4p_2}}{2p_2} = -r_1 \tag{2.17a}$$

$$z_2 = \frac{-p_1 - \sqrt{p_1^2 - 4p_2}}{2p_2} = -r_2. \tag{2.17b}$$

Now solving for B and C,

$$B = \frac{-\varepsilon_0 q_2 r_1 + \varepsilon_0 q_1}{r_2 - r_1} \tag{2.18a}$$

$$C = \frac{\varepsilon_0 q_2 r_2 - \varepsilon_0 q_1}{r_1 - r_2} \tag{2.18b}$$

and taking the inverse Laplace transform the stress for a stress relaxation experiment is found,

$$\varepsilon(t) = \frac{\varepsilon_0}{\sqrt{p_1^2 - 4p_2}} \left[(q_1 - q_2 r_1)\, e^{r_1 t} - (q_1 - q_2 r_2)\, e^{-r_2 t} \right]. \tag{2.19}$$

3D PRINTING ON GLASS FOR DIRECT SENSOR INTEGRATION

Contribution of Authors and Co-Authors

Manuscript in Chapter 3

Author: Michael Neubauer

Contributions: Investigation, Conceptualization, Methodology, Formal analysis, Data curation, Writing — original draft.

Author: Matthew McGlennen

Contributions: Conceptualization, Methodology, Data curation, Writing — review and editing

Author:Sawyer Thomas

Contributions: Investigation, Conceptualization

Author: Stephan Warnat

Contributions: Investigation, Conceptualization, Writing — review and editing.

Manuscript Information

Michael Neubauer, Matthew McGlennen, Sawyer Thomas, Stephan Warnat

Engineering Research Express

Status of Manuscript:
____ Prepared for submission to a peer-reviewed journal
____ Officially submitted to a peer-reviewed journal
____ Accepted by a peer-reviewed journal
_X_ Published in a peer-reviewed journal

IOP Publishing
Published 13 December 2019
DOI: 10.1088/2631-8695/ab5e9f

Abstract

Significant improvements are being made in 3D printed microfluidics. 3D printing of microfluidic prototypes gained importance due to the fabrication flexibility compared to conventional techniques. Applications using these devices often require optical access to internal channels but even clear resins create translucent channels due to surface roughness and imperfections. This paper describes a 3D printing approach to form fluidic channels directly onto glass substrates that allows optical access to fluidic channels without distortion from 3D printing material. The glass substrate is itself a part of the flow channel which guarantees optical transparency. Micro-fabricated conductivity and impedance spectroscopy sensors were fabricated on glass substrates and placed in a custom made 3D printer build plate before fluidic structures are directly printed on top of the sensors. The effects on sensor performance and properties were evaluated using co-linear four-point probe resistance measurements, Raman spectroscopy, and impedance spectroscopy. It was shown that no resin or other chemicals are left behind from the printing procedure and sensor performance was unaffected. A proof of concept impedance-conductivity sensor was integrated with a 3D printed flow channel and shown to work as both conductivity and bacterial cells detection sensor.

Introduction

Additive manufacturing (AM) is becoming an increasingly viable option for the creation of fluidic devices [121–126]. Vat polymerization printing (VPP) such as stereolithography (SLA) and digital light processing (DLP) are popular techniques for creating 3D printing microfluidics due to their high resolution [127, 128]. The resolution of various printing techniques such as VPP, material extrusion, and material jetting are compared in [121–123, 125, 127]. 3D printing allows one-step creation of fluidic devices with high throughput

and straightforward device parameter adjustment in Computer-Aided Design (CAD) software. Designs and devices can be distributed and replicated in different facilities by merely sharing the design files [121]. Commercial availability of printers and resins capable of truly microfluidic (sub 100 μm features) devices is somewhat limited [129]. In this paper, we demonstrate the integration of micro-fabricated sensors on glass with a high-resolution 3D printing technique.

Optically transparent surfaces within microfluidic devices are essential for accurate quantification of chemical, biological, and mechanical interactions [130]. Many 3D printing resins, however, are not clear, and while the use of clear resins theoretically allow for the creation of transparent devices, inherent surface imperfections can cause light diffusion creating translucent channels. There are several examples in the literature of devices printed on glass to create a very smooth surface using SLA and DLP techniques. Urrios *et al* utilized a glass build plate and glass vat to decrease surface roughness and increase print transparency in bio-microfluidic devices [131]. Gong *et al* constructed a custom printer to create microfluidic devices on glass substrates in order to avoid using an anodized aluminum build plate and to provide optical access to internal microfluidic components [132–134]. Parker *et al* 3D printed microfluidic devices with immunoaffinity monoliths on glass allowing for fluorescence measurements for the extraction of preterm birth biomarkers [135]. Lee *et al* 3D printed Quake style valves using glass as a build plate to increase channel visibility, eliminating the need to remove the device from the build plate, and to provide a flat, stable surface for a microscope stage [136]. Kim *et al* printed multiple designed microchannels on glass for convenient optical access [137, 138]. Beauchamp *et al* characterized the 3D printing of sub-100 μm external and internal, positive and negative resolution features and additionally created a particle trapping device with the particles clearly seen as viewed through glass [139]. Beauchamp *et al* again printed on glass to create visible microfluidic channels and fluorescent emission of preterm birth biomarkers inside the

channel was collected [140]. Rogers *et al* fabricated 3D printed microfluidic channels with valves, and claimed that their ability to print directly on glass opened the possibility for direct integration of printing on materials with patterned electrodes [141]. The previous examples of printing on glass utilized base layers to ensure proper attachment, limiting the possibility of direct interaction between sensor material and fluids. Rather than printing directly on glass, Plevniak *et al* used an SLA printer to print a 50 μm open channel and then covalently bonded to glass post-printing resulting in a closed hollow channel [142]. Notably, Kou *et al* printed microfluidic channels directly on glass without the use of base layers to create an optical window for phase-contrast microscopy and fluorescence microscopy. [143]. However, a direct sensor integration in the 3D printed fluidic channel was not shown.

Integrating sensors for 3D printed fluidics is reviewed by Li *et al* [144]. Banna *et al* embedded pH and conductivity sensors into a fused deposition modeling (FDM) 3D print post-print allowing for sensor removal and replacement [145]. Using a print-pause-print technique, Gaal *et al* demonstrated a process for directly integrating an FDM printed structure with an electronic sensor by printing directly on the sensor rather than inserting the sensor post-print. Gold interdigitated electrodes (IDEs) were evaporated on a transparency sheet and a polydimethylsiloxane (PLA) channel was printed directly onto the transparency sheet creating an integrated electronic tongue sensor with optical window for increased channel visibility [146]. Pol *et al* described a fully integrated screen-printed sulfide-selective sensor on a 3D printing potentiometric microfluidic platform accomplished by a screen-printing step between two main FDM printing stages [147]. Di Nova *et al* designed, fabricated and tested a fully aerosol jet printed (AJP) electrochemical microfluidic sensor. Dispensed and cured silver-silver chloride and carbon ink formed electrochemical sensing elements on an alumina substrate while UV-curable polymer ink created a flow channel surrounding the sensing elements [148]. While these techniques work well for sensor integration, none utilize a glass substrate for optically clear channels.

Glass substrates are a viable method for creating optically transparent channels using high resolution printing techniques such as VPP or material jetting described above, however sensor integration often requires a multi-step integration process. In this paper, a glass based impedance-conductivity sensor is directly integrated with a 3D printed flow channel as a proof of concept device. This device is shown to work as both a conductivity sensor and bacterial cells detector. This is accomplished by printing directly on a glass substrate with patterned electrodes without the use of base layers using a DLP resin printer. Build plate modification and glass silane treatment facilitated this direct integration. The motivation for optical access in flow channels is well documented above and further explored below. Resin-printer deficiencies were overcome and sensor performance and properties were quantified both before and after device printing. Finally, sensor functionality is demonstrated with various conductivity and bacterial cells solutions. This work is significant because the advancement and advantages of 3D printed microfluidics described above can be directly integrated with sensors to study biological processes.

Methods

A MiiCraft 50 was the 3D printer utilized in this work. This printer uses 405 nm light to selectively cure polymer to form 3D structures by area-projecting light using DLP as described in [127]. Clear BV007 resin (MiiCraft) was chosen for its advertised low viscosity, transparency, and printer compatibility.

A build plate was manufactured with a 20 x 25 mm insert, shown in Figure 3.1. Using a silicone gasket and a diaphragm vacuum pump (Masis, GZ35-12) a glass slide could be held in place during the printing process and quickly released afterwards. The glass slide protruded slightly from the plane of the build plate; this distance was measured and accounted for in the printer software. Mounting the glass flush with the edge of the insert made it possible to reference the edge of the glass in the software so that prints could be precisely aligned to

the edges of the glass itself with better than 100 μm repeatability.

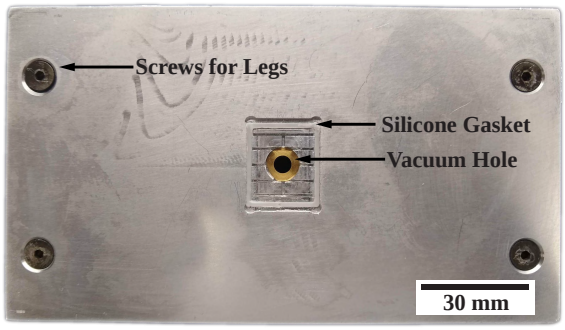


Figure 3.1: Modified build plate with insert for glass slide and silicone gasket and vacuum hole to hold glass substrate in place during printing.

Diced borosilicate glass (BSG) substrates (Borofloat 33, University Wafer), 20 mm x 25 mm x 700 μm, were submerged in a 2.0 vol% solution of 3-(trimethoxysily) propyl methacrylate in ethanol (Bind-Silane, GE Healthcare, 17-1330-01) for five minutes, then submerged in ethanol for five minutes, and finally held at 105°C for five minutes. This silane treatment protocol has been used to couple polymerizing hydrogel to a glass surface [149], but also worked to couple the resin used in this work to the glass without using an initial base layer.

Upon printing completion, the print was submerged in a solution of Resin Away (Monocure PTY LTD) and sonicated for 1 minute, or until all uncured resin was removed. The print and substrate were rinsed with deionized water and post-cured in B9 Model Cure (B9Creations, USA) for 20 seconds. Lab grade isopropanol was found to be less effective than Resin Away, as it would often cause the print to crack.

Physical vapor deposition (PVD) with thermal evaporation was used to deposit 10 nm of Cr adhesion layer, followed by electron-beam evaporation to deposit a 100 nm layer of Au onto a 700 µm thick, 100 mm BSG wafer. A positive photolithography process and wet chemical etch defined the patterned sensor, seen in Figure 3.2. The wafer was diced into nine 20 x 25 mm sensors. These sensors were designed originally as temperature and

electrochemical impedance spectroscopy (EIS) sensors, however in this work the temperature function was not utilized.

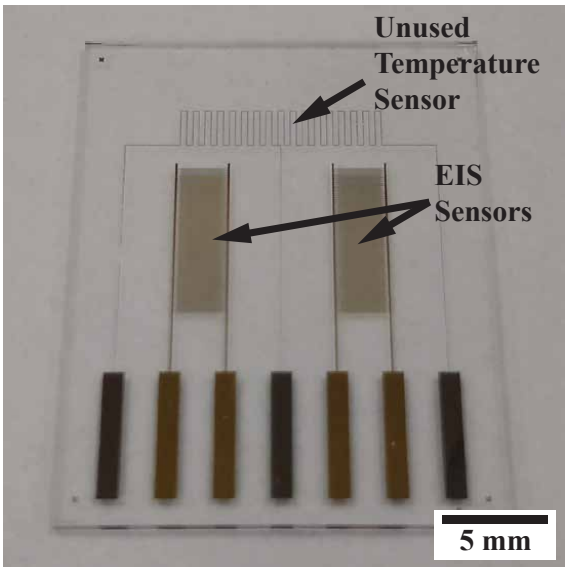


Figure 3.2: Image of micro-machined sensor used in this work.

A flow chart outlining the fabrication process is shown in Figure 3.3(a). Due to the limitation of the resin used in this work, printing closed channels was not deemed feasible. Instead, channels were printed open and a second print was used as a cover. The open channel and cover were each printed on glass and alignment features were designed on the open channel. A #3 round brush was used to lightly coat the contact surface of the open channel with uncured resin and then the cover was aligned and held firmly in place with a clamp during a post-cure process which fused the two prints together, resulting in a well-defined closed channel seen in Figure 3.3(b). While using two prints to create closed channels was possible and repeatable, using a resin capable of closed channels would still be preferred in order to create a higher precision, single-step device.

Replaceable 3D printed barb style adapters allowed tubing (1 mm ID, 3 mm OD, Tygon R-3603) to be connected to the flow channel for fluid introduction. Double-sided Kapton tape was used as an intermediate layer between the channel inlet/outlet and the barb adapter.

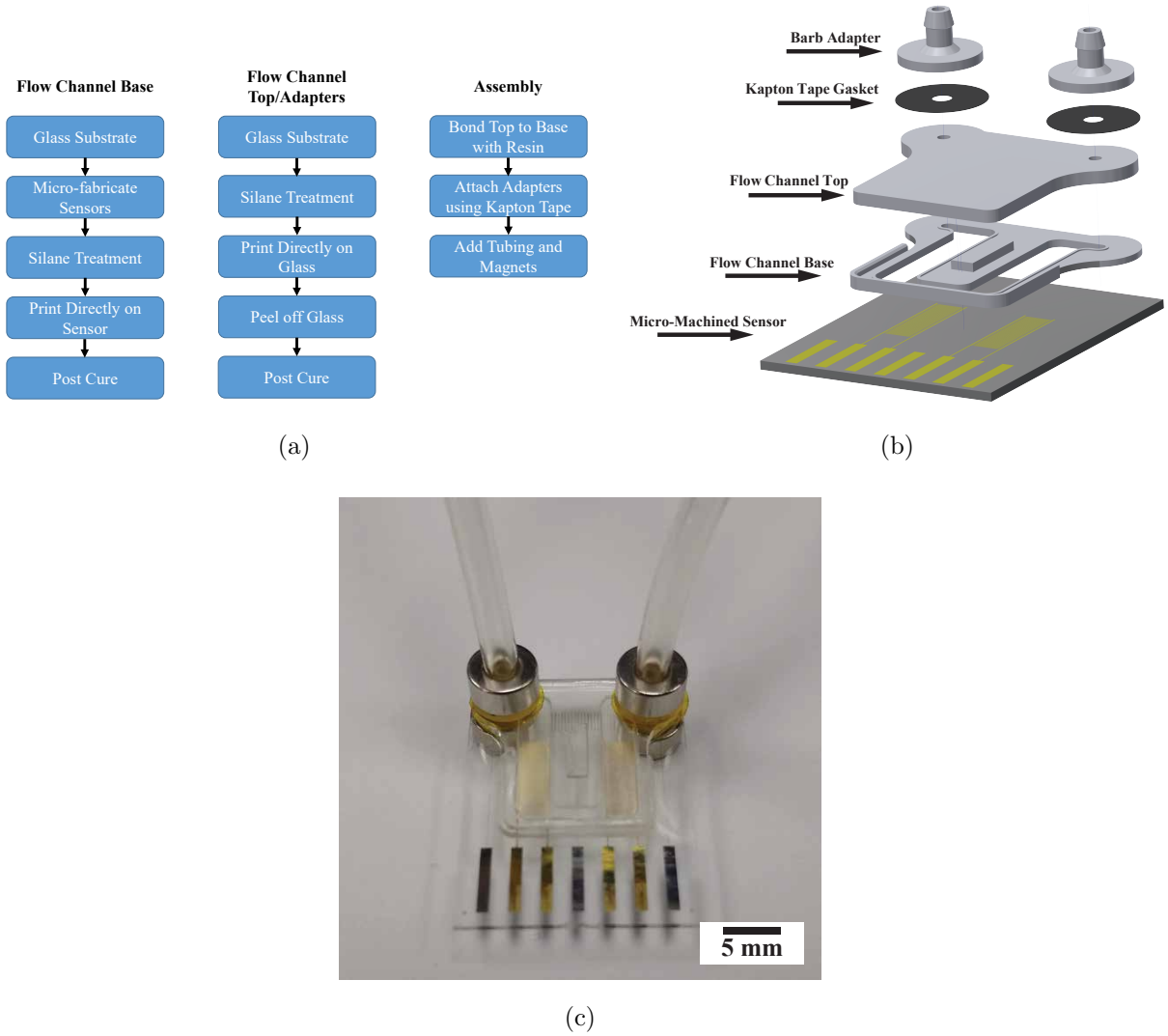
While this was enough to secure the adapter for a short period of time, magnets (R422-N52, K&J Magnets) were used to secure the adapters for longer intervals with higher bursting pressure. These replaceable adapters seen in Figure 3.3(b) and Figure 3.3(c) resembled those used by Atencia *et al* but rather than a blunt needle, a barb connector was printed [150]. One of the advantages of printing adapters is that it can be assured that the liquid from the tube never interacts with the surface of the magnet.

The adapters were printed on glass without the use of base layers so that the sealing face of the adapters was smooth and consistent print to print. A 1 mm hollow punch was used to create a consistently sized hole in the tape and then the adapter was centered and pressed onto the tape. A 7 mm hollow punch was used to cut out the tape in a circle slightly larger than the adapter. When ready for use the protective sheet was removed from the backside of the tape and pressed onto the flow channel inlet/outlet. The tubing was attached to the barb adapter and a ring magnet fit around the tubing onto the adapter. A second, disc magnet (D42-N52, K&J Magnets) provided the clamping magnetic force from the backside of the substrate.

Component Characterization

Light transmission through sample printed on glass was measured with a spectrophotometer (FastSpec 528, MicroLab, USA) to quantify optical clarity of printing on glass. The transmittance, defined as the ratio of light which passed through the sample to the incident light, was recorded in this manner. 502 nm and 660 nm light was emitted from an LED towards a light detector and the intensity was measured. Measurements were taken by placing a 3D printed sample between the LED and detector. One sample of each thickness was measured 5-10 times at these two wavelengths.

To demonstrate the improved image clarity provided by printing directly on a glass substrate, 275 μm microbeads (REDPMS-1.080 250-300μm, Cospheric, USA) were placed in



(a) (b)

(c)

Figure 3.3: Fabrication process and image of device. (a) Flow chart of device fabrication. (b) Exploded view of designed sensor packaging. (c) Assembled device with tubing and magnets.

a suspension solution and directed through the integrated flow channel on the sensor under a microscope. Images were collected viewing the microbeads through both the glass substrate and through the printed flow channel.

The bursting pressure of the magnetic adapters was tested in a similar manner to

[150]. A printed solid cylinder and adapter were attached with a piece of Kapton tape. The printed cylinder simulated the flow channel to which adapters were attached. For consistency, cylinders were printed on glass and peeled off and post-cured with the glass side being the side to which the tape was affixed. Tubing connected the adapter to a 10 mL Becton Dickson syringe placed in a Kent Scientific GenieTouch syringe pump. The adapter end of the tubing was submerged in water so that the appearance of bubbles marked the point at which the connection began to leak. The volume of air in the tubing and syringe was noted. Approximating air as an ideal gas, the ideal gas law could be rearranged into Equation 3.1

$$P = P_a V_i/(V_i - dV) \tag{3.1}$$

where P_a is atmospheric pressure, V_i is the initial volume recorded, and dV is the volume dispensed by the syringe pump, respectively. The guaranteed pressure applied by the syringe pump for this specific syringe according to the manufacturer was approximately 6 atm. Atencia *et al* found a bursting pressure of approximately 5 atm using a similar procedure with Kapton tape and magnets [150].

Device Characterization

Resistance measurements were performed on Au samples with identical deposition parameters in order to quantify the effect of the silane treatment on sensor performance. A custom-built co-linear four-point probe with 1.3 mm needle tip spacing and a Keithley 2450 SMU were used to conduct the measurements. Spherical spring-loaded testing tips with a diameter of 0.6 mm were used to guarantee a good electrical contact (uxcell P11J). Ten consecutive readings of each current polarity were acquired and averaged. This was repeated ten times for two samples before and after silane treatment.

In order to confirm no resin or other chemicals are left behind from the printing process

or silane treatment, three sensors from the same process wafer were investigated with Raman spectroscopy. One sensor was left untreated, a second received the silane treatment, and the third received the silane treatment and the base of the flow channel was printed on the sensor. A spectra was collected from a spot both on the glass and the gold from each sensor with a Horiba Labram HR Evolution Raman spectrometer. Additionally, a scan of the cured resin was captured.

The impedance spectra of a conductivity standard (Biopharm 84 μS/cm) collected before and after printing, with and without magnets was obtained in order to confirm the sensor performance remained unchanged due to printing. Before applying the silane treatment and packaging the sensor, a flow channel with the same dimensions (not printed on glass) was printed and clamped on top of the sensor using a silicone gasket to seal the channel. Three spectra were obtained using a Hioki IM3536 LCR in the range of 1 kHz - 8 MHz, rinsing the flow channel with deionized water between measurements. Another three spectra were obtained with the magnets for the barb adapters in place. Three more spectra with and without magnets were obtained after printing was complete.

Sample Applications

As a proof of concept application, various conductivity solutions were synthesized using conductivity standards (Biopharm) and deionized milli-Q water (GenPure xCAD Plus, Thermo Scientific, 18.2 MΩ cm). Solutions of 21, 42, 63, 84, 141 and 353 μS/cm were created using milli-Q water to dilute 84 and 1413 μS/cm conductivity standards with the assumption that the milli-Q water had an insignificant conductivity relative to the conductivity standards. Impedance spectra from 1 kHz - 8 MHz were collected in the same manner as described previously. A frequency of 100 kHz was chosen to calculate the conductivity. Using a linear model for the conductivity-temperature relationship shown in

Equation 3.2, a temperature coefficient α was calculated using Equation 3.3

$$\kappa = \kappa_{ref}(1 + \alpha(T - T_{ref})) \quad \mu\text{S/cm} \tag{3.2}$$

$$\alpha = \frac{\kappa - \kappa_{ref}}{\kappa_{ref}(T - T_{ref})} * 100 \quad \%/^{\circ}\text{C} \tag{3.3}$$

where κ and T were the measured conductance and temperature and κ_{ref} and T_{ref} were the advertised conductivity at the reference temperature of 25 °C, respectively.

As another proof of concept application, Escerichia coli K12 cells were suspended in milli-Q water and different dilutions were analyzed using impedance spectroscopy. A Petri dish was removed from refrigerator stock, and a single colony of *E. coli* K12 was scraped from a Petri dish, and introduced into a 50 mL Falcon tube containing 25 mL of 1X tryptic soy broth (TSB; BD Bacto). The Falcon tube was inserted into an incubator (37 °C) with orbital shaker (150 RPM) for 19 Hours. Subsequently, the Falcon tube was centrifuged at 4700 RPM for 10 min. TSB media was replaced from the Falcon tube with 25 mL of autoclaved milli-Q water and thoroughly mixed. Nine 1.5 mL micro-centrifuge tubes were arranged in linear sequence for dilution series. 1 mL of media containing *E. coli* K12 was pipetted from undiluted Falcon tube into a first micro-centrifuge tube, and was thoroughly mixed. Next, 100 μL of media was pipetted from first mixture, and combined with 900 μL of milli-Q water into second micro-centrifuge tube creating a $1{:}10^1$ dilution of *E. coli* K12 cells to milli-Q water. This procedure was repeated until a dilution of $1{:}10^8$ (ninth micro-centrifuge tube) from the original was reached. All steps were performed inside a biosafety cabinet to ensure sterile conditions.

To obtain cell counts, 100 μL of the final four dilution mixtures were pipetted onto Petri dishes containing tryptic soy agar (TSA; BD Bacto) and spread using glass spreaders. The Petri dishes were sealed with parafilm and left for 24 hours at room temperature to incubate. Cell concentrations were performed by counting the individual colony-forming units (CFU)

established on each plate, multiplying by the level of dilution, and dividing by the amount of media pipetted.

Yang *et al* performed a similar experiment where Salmonella cells were suspended both water and phosphate-buffered saline (PBS) and the impedance response over a range of frequencies were recorded using interdigitated microelectrodes. It was found that cell concentrations could be distinguished down to 10^6 CFU/mL and higher in water, while cells suspended in PBS could not be distinguished [151].

Results and Discussion

Component Characterization

The transmittance of a blank glass slide yielded a value within 1 % of the theoretical transmission of approximately 92 % [152]. Parts printed directly onto glass resulted in transmission values less than that of glass, as seen in Figure 3.4, but still averaged higher than 90 %. These data suggest that the 3D prints are not significantly scattering or absorbing the incident light, as the average transmittance is still within 5 % to that of glass.

The packaged sensor can be seen in Figure 3.3(b) and again in Figure 3.5(a) with the barb adapters and yellow Kapton tape with magnets and tubing attached. Figure 3.5(b) shows how the relative position of the microbeads to each finger of the impedance sensor and channel wall is well-defined. In addition, the bead diameter is more easily determined which may be of interest with objects of unknown size. Note: The diameter of the used beads has an advertised variation of 50 μm and our measurements with a calibrated optical microscope were within this tolerance. In contrast, in Figure 3.5(c) the relative microbead position and diameters are more challenging to determine.

During testing of the magnetic connectors, the syringe pump compressed the syringe past the advertised guaranteed force of the syringe pump with one or two exceptions. It's possible the syringe pump is capable of applying more force than advertised, or

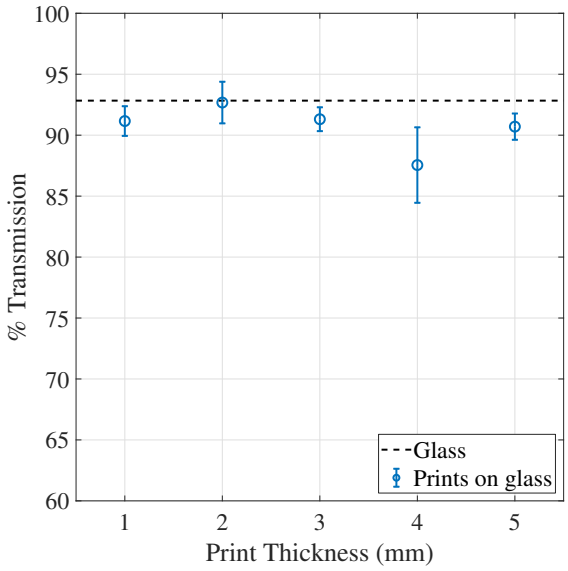


Figure 3.4: Plot showing mean transmission of 502 nm and 660 nm light. Note: Error bars represent standard deviation.

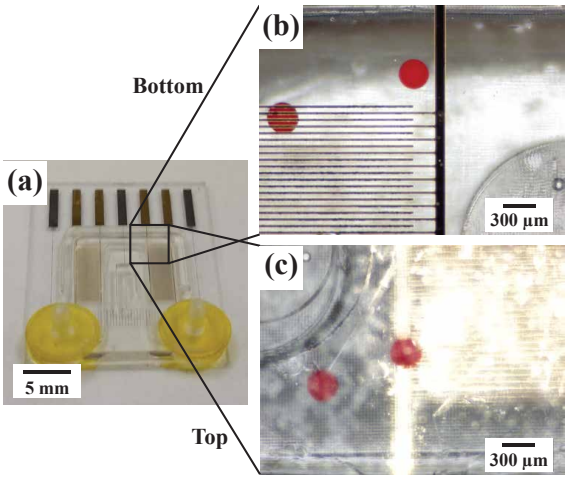


Figure 3.5: 275 μm microbeads viewed through (b) bottom of sensor (via glass substrate) and (c) through the top (via printed structure).

approximating air as an ideal gas breaks down below 6 atm. In any case, the syringe pump was unable to cause the magnetic adapters to leak by nearly fully compressing 10 mL of air. This was deemed more than adequate for this work.

Device Characterization

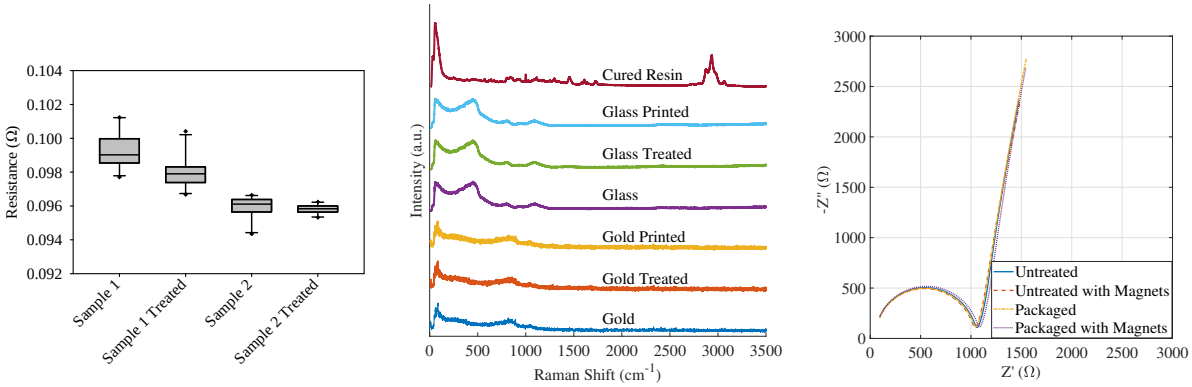
After performing the resistance measurements on two gold samples before and after silane treatment, a paired t-test with a double tail p-value of 0.048 and 0.740 was found for sample 1 (pre- and post-treatments) and sample 2 respectively, using the set of ten means. A boxplot showing these data is shown in Figure 3.6(a). The p-values suggest the silane treatment has minimal effect on the resistance of Au used for the sensors in this work.

The Raman spectra are shown in Figure 3.6(b) with the cured resin spectra shown first followed by the glass and gold surfaces pre- and post-silane treatment and post-printing. All gold and glass substrates look alike regardless of silane treatment or printing and none show the peaks of the cured resin around 3000 cm^{-1}. This suggests that no resin or other chemicals are left on surfaces.

Impedance spectroscopy measurements were performed to evaluate sensor performance before and after the printing on the sensor. These data are plotted in a Nyquist diagram, which shows the real resistance versus the negative imaginary resistance. The curves of the Nyquist plot overlap in Figure 3.6(c) suggesting that sensor performance is negligibly affected by the printing process.

Sample Applications

The six conductivity solutions can be clearly distinguished in a Nyquist plot in Figure 3.7(a). The experimental cell constant of 0.0832 cm^{-1} was found by comparing a commercial conductivity meter (Omega, CDS107). Using the linear temperature conductivity model described in Equation 3.2 and Equation 3.3, the conductivity of the various solutions was calculated and plotted in Figure 3.7(b). The error bars show the min-max uncertainty due to temperature uncertainty. Also plotted is the measured conductivity by the commercial meter. The sensor measured conductivity values within 8 % of the meter with the exception of the lowest and highest conductivity solutions which each varied by more than 12 % from



(a) (b) (c)

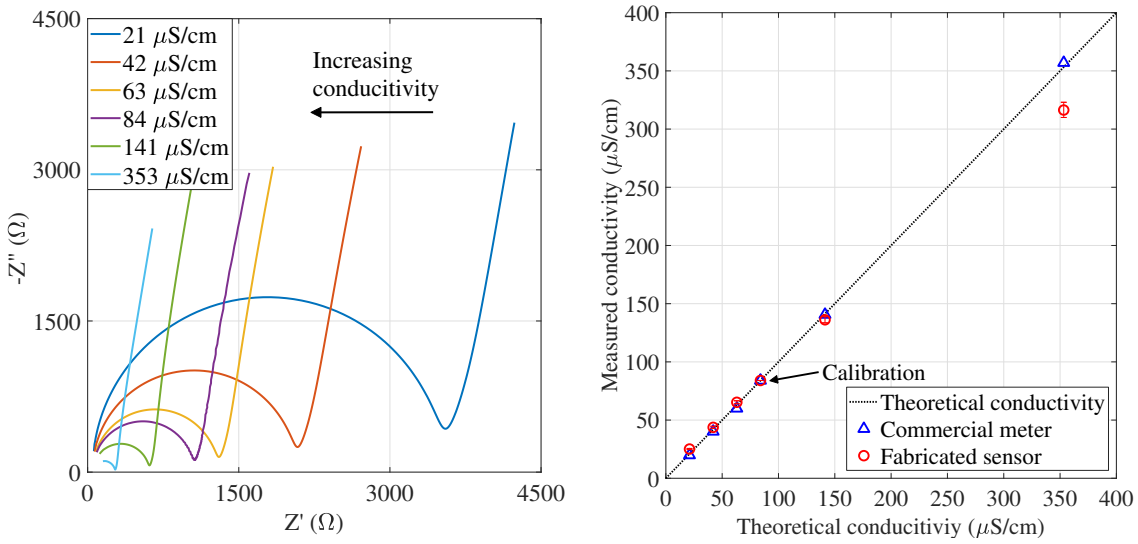
Figure 3.6: Results of device characterization. (a) A boxplot showing the resistance of the two samples pre- and post-silane treatment. A paired t-test with a double tail p-value of 0.048 and 0.740 for sample 1 - sample 1 treated and sample 2 - sample 2 treated respectively. (b) Raman spectra of substrates which were untreated, treated, and printed on including a spectra of cured resin. Scans are offset for viewing convenience. (c) Nyquist plot of 84 μS/cm conductivity standard with and without magnetic connectors, pre- and post-printing on sensor and silane treatment.

the meter. The working range of the sensor is affected by both the cell constant and the linear temperature compensation model.

Impedance spectra were collected from 4 Hz - 5 MHz on three dilutions (2.4 x 10^6, 2.4 x 10^7 and 2.4 x 10^8 CFU/mL) of suspended *E. coli* K12 cells and the Nyquist curves are shown in Figure 3.8. The three dilutions are clearly distinguished in this plot and show that this packaged sensor is capable of distinguishing concentrations of bacterial cells down to 2.4 x 10^6 CFU/mL. It was found that lower concentrations of cells could not be distinguished, therefore the detection limit for this sensor is 2.4 x 10^6 CFU/mL for *E. coli* K12 cells suspended in water.

Discussion

The described procedure demonstrates how printing on glass can be applied to an arbitrary micro-machined sensor for integrating 3D printing and sensors. The sample



(a) (b)

Figure 3.7: Results of measuring various conductivity solutions. (a) Nyquist plot of different conductivity solutions. (b) Theoretical vs measured conductivity with a commercial conductivity sensor and the packaged device. Note: Error bars showing min-max uncertainty due to temperature uncertainty.

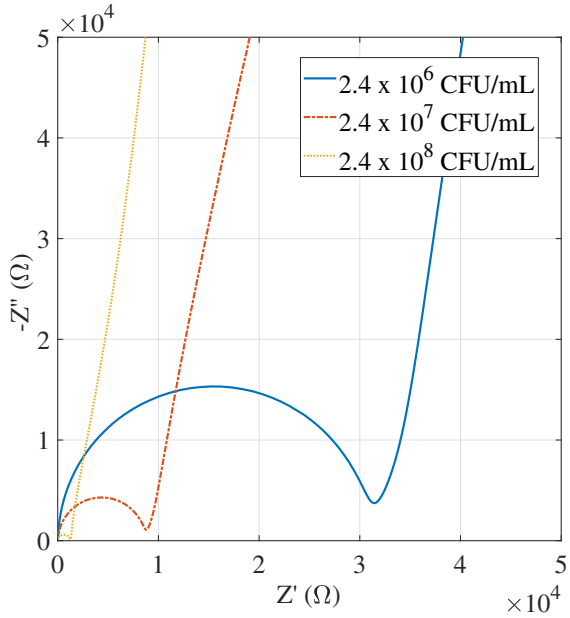


Figure 3.8: Nyquist plot of three different dilutions of *E. coli* K12 cells in milli-Q water.

applications were chosen to suit the sensors, however similar micro-fabricated sensors could be designed for many other applications. The procedure of build plate modification and silane treatment are compatible with the higher resolution printers and resins described above, and therefore recent advancements of 3D printed microfluidics can be integrated with micro-fabricated sensors in this described manner.

Conclusion

In this work, a procedure for direct integration of glass substrate sensing platforms with complex and precise packaging is outlined. The glass substrate is itself a part of the channel and guarantees ideal optical access. Resistance measurements, Raman spectroscopy, and impedance spectra show that sensor properties are unaffected and no resin or chemicals are left on the sensing surface after printing on the sensor. Viability of materials other than Au could be tested for other applications with similar techniques. Microbeads were imaged through the glass substrate to show the improved optical properties compared to imaging through a thin printed channel wall using clear resin. As proof of concept applications, a simple impedance-conductivity micro-machined sensor was directly integrated with a 3D printed flow channel with a well-defined sensing area and was shown to work as a conductivity sensor and *E. coli* K12 dilution detector with a detection limit of 2.4 x 10^6 CFU/mL. Applying the same methods for device realization, any number of devices can be integrating with a 3D printed structure. The limitations on device design generally are associated with the 3D printer, its resolution and compatible resins. These issues will become less prevalent as the technology in this rapidly advancing field improves and becomes available. Overall, this process will benefit from all advances in 3D printing technologies, becoming an increasingly viable avenue for sensor-packaging integration for bio-sensing.

VISCOELASTIC RECOVERY TIMES OF CHONDROCYTES MEASURED USING A NOVEL 3D-PRINTED DEVICE

Contribution of Authors and Co-Authors

Manuscript in Chapter 4

Author: Michael Neubauer

Contributions: Investigation, Conceptualization, Methodology, Formal analysis, Data curation, Writing — original draft.

Author: Priyanka Brahmachary

Contributions: Conceptualization, Methodology, Writing — original draft.

Author: Alan Fine

Contributions: Investigation, Conceptualization, Writing — review and editing.

Author: Ron June

Contributions: Investigation, Conceptualization, Writing — review and editing.

Author: Stephan Warnat

Contributions: Investigation, Conceptualization, Writing — review and editing.

Manuscript Information

Michael Neubauer, Priyanka Brahmachary, Alan Fine, Ron June, Stephan Warnat

Biomedical Microdevices

Status of Manuscript:
_X_ Prepared for submission to a peer-reviewed journal
____ Officially submitted to a peer-reviewed journal
____ Accepted by a peer-reviewed journal
____ Published in a peer-reviewed journal

Springer

Abstract

Here, we introduce the design, fabrication, and operation of a 3D-printed microfluidic device to measure the viscoelastic recovery times of cartilage cells, chondrocytes. Bovine chondrocytes were imaged using a confocal microscope and compressed by a dynamic/movable glass plate. Their recovery was tracked using their time-series projected area, which was converted into a linear strain and fitted to a Burgers mechanical model. Strains ranging from 10% to 60% were applied to the cells, and model parameters, including viscoelastic recovery time, were extracted. Cells that experienced strains greater than 40% exhibited radially-asymmetric deformations. This observed radially-asymmetric deformation occurred as a short-term effect, where the cell fully recovered its initial shape and as permanent disruption to the cell shape. Overall, this work demonstrates the proof-of-concept of a 3D-printed microfluidic device as a tool for viscoelastic characterization of cells.

Introduction

Biological cells are protected from mechanical loading by their cytoskeleton, which is crucial in determining the cell shape and mechanical properties [153]. Because of the diversity of environments, many different types of cells have a broad range of viscoelastic properties. Many cells sense their mechanical environment and respond or adapt to it through the process called mechanotransduction [154, 155]. One example of this type of cell is chondrocytes, which are embedded with articular cartilage which lines the ends of bones in diarthrodial joints. These cells maintain the extracellular matrix (ECM), the predominant component of cartilage, and produce a pericellular matrix (PCM) shell around themselves for mechanical protection, chemical exchange, and biochemical signaling [102–105]. Changes to the metabolic state of chondrocytes have been linked to the onset of osteoarthritis (OA) [105], a common chronic disease affecting more than 300 million people worldwide and posing

a significant economic burden on patients and healthcare providers [3, 106].

Measuring mechanical biomarkers provides insight into cell health and adaptation to the environment because mechanical properties are closely tied to the structural and functional integrity of cells. Investigating cells at the single-cell scale is typically preferred because even genetically identical populations often express multiple phenotypes, the set of observable characteristics. Four conventional approaches are (i) atomic force microscopy (AFM), which involves moving a small probe in contact with a single cell [156–159]. The specific force or indentation depth is precision controlled, and the cell response force is recorded. (ii) Optical tweezers (OT) use highly focused laser beams to manipulate single cells in a non-contact manner [22, 160, 161]. (iii) In micropipette aspiration (MPA), negative pressure forces cells to enter small glass pipette tips [8, 26, 27, 162]. Light microscopy tracks the cells' deformation when entering the pipette. Micropipette aspiration is relatively inexpensive compared to the higher-resolution AFM and OT methods. (iv) Microplate manipulation involves placing single cells between two cantilever beams and compressing the cell while measuring the force and displacement, similar to the AFM methods [163–165]. The high spatial resolution of the AFM and OT techniques allows for local characterization, where the individual components or regions of cells can be investigated individually. MPA and microplate manipulation measure cells' global or bulk mechanical properties, where the entire cell is characterized as a whole.

A significant drawback of the described techniques is the low throughput, 1-10 cells/hour [7]. The main reason for a low throughout is the difficulty of handling and positioning cells at the single-cell scale. The main reason for the low throughput is the difficulty in handling and positioning cells at the single-cell scale. The high precision of methods such as AFM and OT is invaluable for a more thorough scientific understanding of cell mechanics. However, given the previously mentioned heterogeneity of cells in a population and the large number of cells required to build statistically significant data, higher-throughput measurements are

preferred and needed for practical applications.

Recently, many of these methods have been adapted to microfluidic platforms. Microfluidics is the manipulation of fluids at the micrometer scale in channels dimensioned at the same length as the scale of biological cells. This technology enables precise handling and manipulation of cells at high speeds. Several examples of microfluidic micropipette aspiration devices demonstrate throughputs of up to 100 cells/h, which is typically accomplished by fabricating multiple channels in parallel within the field-of-view (FOV) of a microscope camera [48, 52–55]. Scaling up the number of channels beyond roughly 20 is difficult because of the pressure drop variability of the parallel channels and the space constraint of the camera [54].

In this study, we present the fabrication and use of a novel microfluidic device to measure the viscoelastic recovery time of bovine chondrocytes at a rate of 50 cells/h. The concept of a variable-height flow channel for imaging cells has been previously explored [98], but this work applies it for measuring mechanical properties of cells. The device is cost-effective and accessible to many researchers because it is fabricated primarily through 3D printing, rather than requiring PDMS mold fabrication facilities. The device is flexible in that it can, in principle, characterize cells of 1- 75 µm by simply changing the pressure applied to modulate the position of the glass clamping plate.

Materials and Methods

3D-printed Flow Cell Fabrication and Assembly

A conceptual overview of the device is shown in Figure 4.1. The flow cell consisted of two channels: one variable-height channel with a movable piece of glass, which compressed the cells, and one control chamber, which was pressurized to actuate the movable glass surface. The device was assembled in multiple stages including multiple 3D prints and silicone/glue curing steps.

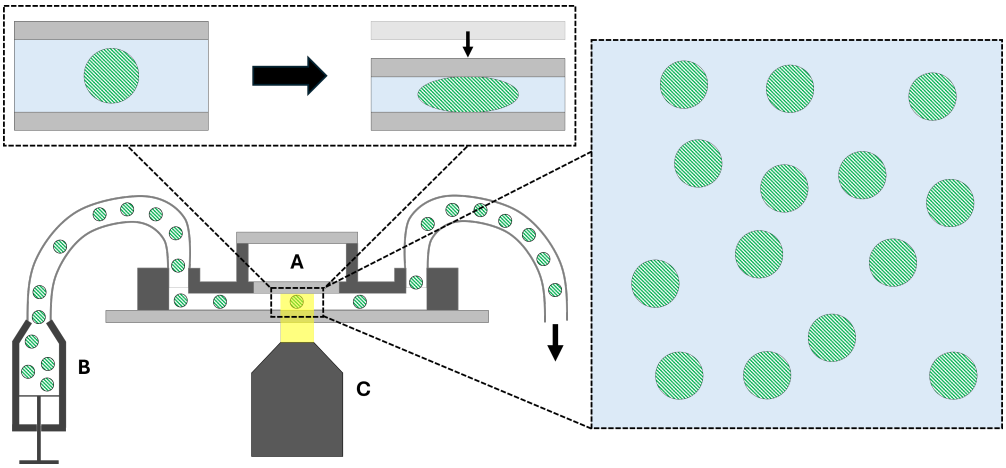


Figure 4.1: A conceptual overview of the device. Cells (striped, green circles) are suspended in a buffer solution in a syringe (labeled B) and flown through a 3D printed microfluidic device which is mounted in a microscopy system (labeled C). Cells in the field-of-view are compressed between two pieces of glass and released while their apparent diameters are imaged. To compress the cells, the air pressure in the control chamber (labeled A) is adjusted with a feedback-controlled pressure system.

The first stage of 3D printing, shown in Figure 4.2, formed the deformable channel that was printed directly onto No. 1.5 coverslip (24 x 50 x 0.17 mm) using an Epax X1 4k printer and eSun PLA-Pro resin. The coverslip was treated with bind-silane (3-(trimethoxysilyl) propyl methacrylate 17-1330-01; GE Healthcare, USA) to improve the adhesion of the resin to the coverslip, as described in [166]. A coverslip increases the imaging resolution, as the microscope objectives are commonly corrected for the No. 1.5 coverslips. However, the resin shrinks when cross-linked by 405 nm light and causes the thin coverslip to deform. To prevent this, the 3D-printed structure was designed to be as thin as possible (1 mm) to reduce the internal stress in the resin, and the coverslip was reinforced by a microscope slide (25 x 75 x 1 mm) connected to the coverslip with thermal-release-doubled-sided tape (RevAlpha 319Y-4M, Nitto, USA). The microscope slide, tape, and coverslip stack were attached to the build plate of the 3D printer with double-sided polyimide tape (Kapton, DuPont, USA), and the thickness of the stack was accounted for in the 3D printer software

by adjusting the build plate offset. Treating the coverslip with bind-silane eliminates the necessity for overexposed base layers, which are typically required for proper adhesion when printing on the build plate. This allows the channel to be printed open on the glass so that the coverslip forms one wall of the channel and the other three are defined by the cured resin. After printing was completed, the stack was removed from the build plate and sonicated in 99% isopropyl alcohol (IPA) for 1 min, followed by rinsing with IPA and deionized water (DIW). Compressed air was used to dry the print, and the microscope slide stiffener was left attached to the coverslip until the final assembly was complete.

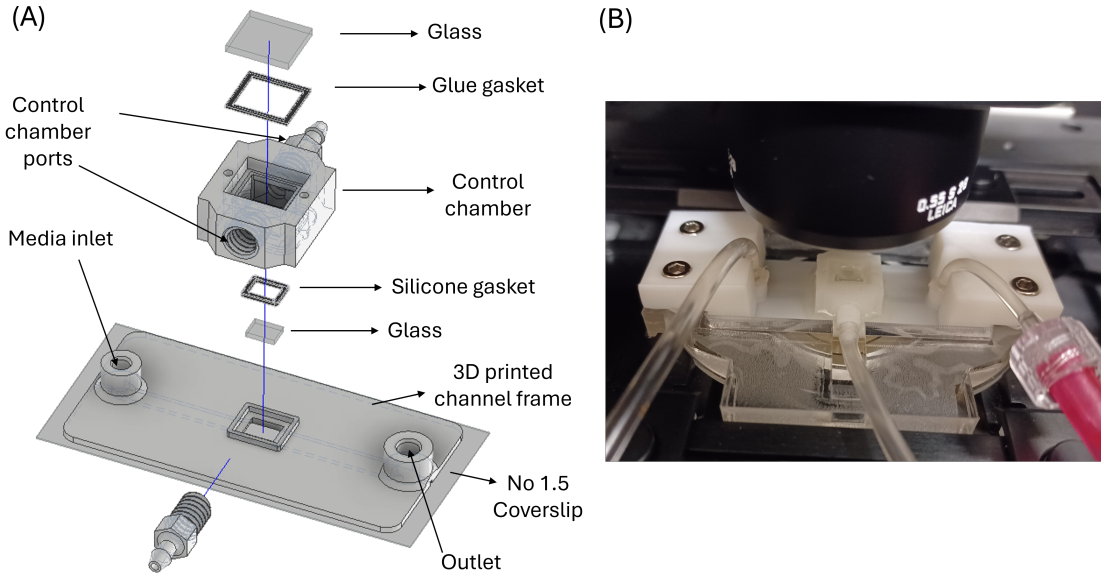


Figure 4.2: Exploded view of the 3D-printed device, showing all the components of the device. (B) An image of the assembled device clamped in the acrylic flattening jig and mounted in the inverted confocal microscope.

The movable glass was made from a 700 µm thick borosilicate glass wafer (Borofloat 33, University Wafer, USA) diced into 3 x 4 mm rectangles with a Disco DAD 3221 dicing saw. After dicing, the individual glass pieces were attached to a single-sided water-soluble tape (5414, 3M, USA) to set the initial gap between the movable glass and the coverslip. The movable glass was placed into a designed cutout in the 3D-printed channel with water-soluble

tape in contact with the coverslip. A custom-built dispenser was used to apply aquarium-grade silicone over the interface of the movable glass and the 3D-printed frame. Aquarium-grade silicone was chosen for this application owing to its high mechanical compliance and low chemical leaching. The alignment features on the 3D-printed channel frame allow a separate 3D-printed structure to be affixed to the first 3D print with silicone and epoxy centered over the movable glass. The second 3D print defines the control chamber, which, when pressurized, actuates the movable glass, changing the height of the deformable channel. A 7 x 8 mm glass window was hand-scribed from a microscope slide and attached to the top of the control chamber with silicone and reinforced with epoxy, as shown in Figure 4.2. 3D-printed barb fittings were threaded into the control chamber and sealed with silicone. The deformable channel's inlet and outlet tubing (1/32 in I.D, 3/32 in O.D, Tygon E-3603) were press fitted into openings in the 3D-printed channel frame, and silicone was used to secure them in place.

The water-soluble tape was removed by flushing the device with warm water. Fourier transformed infrared spectroscopy (FTIR) was used once to confirm complete removal, as described in the Supplemental Materials and shown in Figure B.1. The last step before mounting on a microscope was to remove the microscope slide stiffener by using a heat gun to warm the microscope slide and activate the heat release tape. Once the tape and microscope slide were removed, the assembly was clamped into a custom-built stiffener jig, as shown in Figure 4.2(B), which kept the coverslip flat during imaging. The acrylic for the jig was laser-cut and assembled with double-sided tape and M3 hardware.

Cell Culture

Bovine chondrocytes were harvested from knee joints of 18-22 month old cattle obtained, from a local abattoir. Briefly, tissue was digested with Collagenase Type I (2 mg/mL) (Gibco, Waltham, MA, USA) for 14 h at 37 °C using a previously established protocol [108]. Isolated

chondrocytes were cultured for 10 days in Dulbecco's Modified Eagle's medium (DMEM) (Gibco, Waltham, MA, USA) supplemented with Fetal Bovine Serum (FBS) (10% v/v) (Bio-Techne, Minneapolis, MN, USA), penicillin (10,000 I.U./mL), and streptomycin (10,000 µg/mL) (Sigma, St. Louis, MO, USA) in 5% CO2 at 37 °C and first passage population was used for experiments.

$1x10^6$ cells/ml of bovine chondrocytes were resuspended in Phosphate Buffer Saline (PBS, 1X) and Calcein AM (eBioscienceTM Calcein Blue AM Viability Dye, Invitrogen) was added at a 5 µM final concentration. The cells were incubated in 5% CO2 at 37 °C in the dark for 30 min.

Cell Compression Procedure

To reduce cell adhesion to the glass and 3D-printed channel, a 1% by volume solution of Pluronic F-127 (Sigma-Aldrich) in DIW was flushed through the deformable channel for 24 h before injecting cells into the device, similar to [86]. Syringe pumps (GenieTouch, Kent Scientific, USA) controlled by a custom LabVIEW 2017 VI were used to inject the chondrocyte cells and control the pressure in the control chamber. This feedback-controlled pressure controller is desribed in the Supplemental Materials and shown in Fig. B.2. The response time of the controller is shown in Figure B.3.

The cells were injected into the device while the movable glass plate was lowered by increasing the pressure in the control chamber. The cells continued to flow through the channel until the movable glass surface was lowered sufficiently to initiate clamping. The uncompressed diameter of the cells was measured immediately after stopping them in the channel. Several pressures were chosen with different groups of cells vary the applied strain. This point was defined as the maximum compression at which the flow was turned off. Compression was maintained for 30 s for all experiments, and then the pressure in the control chamber was quickly lowered. The diameter of the cells was measured frame-by-frame as

the cells relaxed back to their initial diameters over an additional 180 s.

Microscopy

Cells were imaged with a confocal microscope (Stellaris DMi8, Leica, USA) using a 20x objective (HC PL APO 20x/0.75 CS2, dry objective, Leica, USA). A time-series Z-stack was recorded at a 0.68 µm step height and of 2.3 s stack frequency. Cells suspended in 1x PBS mixed were injected into the device using a Genie Touch syringe pump (Kent Scientific, USA). The flow was stopped when the cells were in the compression area and the control chamber was pressurized to lower the glass plate onto the cells. The compression of the cells was held for approximately 30 s before quickly releasing the applied pressure, allowing the cells to relax towards their undeformed state. Cells were imaged before, during, and after compression.

Image Analysis

To calculate the total projected area (shadow) of the cells before, during, and after compression, each Z-stack of the time series was reduced to a single image using the mean intensity projection (MIP) operation in Imaris (Oxford Instruments). The time series was then imported into MATLAB (Mathworks, USA), and each frame of the compressed time series was analyzed using a custom Sobel edge detection script to extract the total projected area of each cell during compression and recovery. The recovery curves of the individual cells were fitted using Equation 4.4 using a non-linear least squares method in the Curve Fitting Toolbox of MATLAB to extract the relaxation time.

Cells touching the edges of the FOV or other cells were excluded from the analysis. To limit the dataset to viable cells, dim cells with an intensity of less than 75% of the brightest cells were omitted. Some cells showed blebbing behavior when compressed and were treated as a separate cell population.

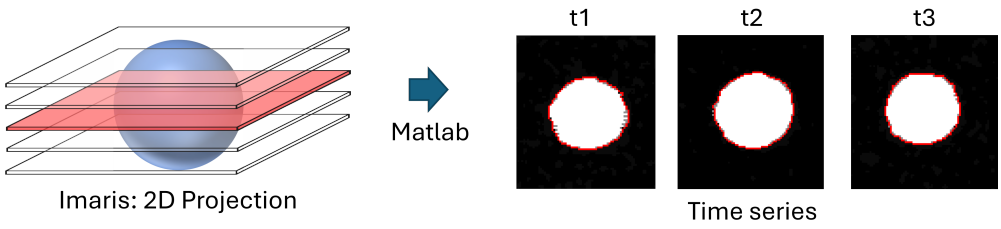


Figure 4.3: Each Z-stack in the time-series is converted to a single image by a MIP 2D projection in Imaris. Then the time-series is imported into Matlab and the projected area of each cell is found by an edge detection algorithm. The time series shows a single cell with the edge marked in red.

Theory

The projected area shown in Figure 4.3 is the parameter measured in the image analysis; however, it is not simple to fit to an equivalent circuit model. Therefore, it is converted to a linear strain by assuming that the cell deforms as a perfect spheroid, with Rx and Ry deforming at the same rate and magnitude as Rz, as described by [86]. In practice, the contact area between a cell and either glass plate is larger than a infinitesimal point, so the rigid spheroid assumption underestimates linear strain of a cell compressed between two plates.

Viscoelastic models such as the standard linear solid (spring-dashpot series in parallel to another spring) have been applied to chondrocytes previously in micropipette aspiration studies [26, 27, 48, 50]. However, this model fails to capture any permanent strain characteristics. Therefore, the four-element Burgers model (Figure 4.4) was used in this study. This model is a series combination of the Maxwell (spring and dashpot in series) and Kelvin-Voigt (spring and dashpot in parallel) models. The constitutive equation for this model is,

$$\sigma + \left(\frac{\eta_1}{E_1} + \frac{\eta_1}{E_2} + \frac{\eta_2}{E_2}\right)\dot{\sigma} + \frac{\eta_1\eta_2}{E_1E_2}\ddot{\sigma} = \eta_1\dot{\varepsilon} + \frac{\eta_1\eta_2}{E_2}\ddot{\varepsilon} \tag{4.1}$$

where σ Is the stress, ε is the strain, E_1 and E_2 are elasticity elements and η_1 and η_2 are viscosity elements. For a constant applied stress, the creep behavior is described as,

$$\varepsilon = \frac{\sigma_0}{E_1} + \frac{\sigma_0}{\eta_1}t + \frac{\sigma_0}{E_2}\left(1 - e^{-(E_2/\eta_2)t}\right) \tag{4.2}$$

and when the applied stress is removed at $t = t_1$, the creep recovery is,

$$\frac{\sigma_0}{\eta_1}t_1 + \frac{\sigma_0}{\eta_2}\left(e^{(E_2/\eta_2)t_1 - 1}\right)e^{-(E_2/\eta_2)t} \text{ for } t > t_1. \tag{4.3}$$

The unconstrained recovery takes the general form shown in Figure 4.4 and written as,

$$\varepsilon = \varepsilon_{elastic} + \varepsilon_{ve}e^{-t/\tau} + \varepsilon_{viscous} \tag{4.4}$$

where τ is the viscoelastic recovery time and the $\epsilon_{elastic}$, ε_{ve}, and $\varepsilon_{viscous}$ terms describe the instantaneous elastic recovery, the constant of exponentially decaying recovery, and the permanent strain due to the viscous flow of the dashpot η_1 [167].

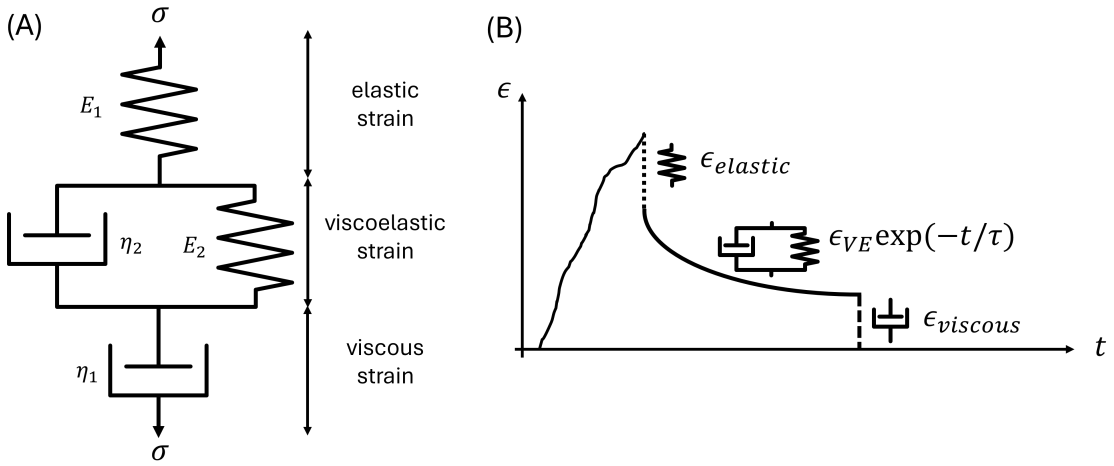


Figure 4.4: (A) Burgers model with the elastic, viscoelastic, and viscous strain labeled. (B) General recovery shape for an arbitrary strain. The viscoelastic strain takes the shape of an exponential function, and the total recovered strain is the sum of the elastic, viscoelastic, and viscous strains.

Results and Discussion

Image Analysis and Curve Fitting

Although a threshold edge detection method was initially attempted, the position of the cell edge was inconsistent cell-to-cell as the intensity of the cells varied. The Sobel edge detection method is based on the intensity gradient, which results in a consistent cell edge when analyzing cells with varying intensities.

An example of the measured projected area of a cell and the calculated linear strain over time is shown in Figure 4.5(A) and (B), respectively. This cell showed permanent deformation, but not all cells demonstrated this behavior.

Cell Deformation and Recovery

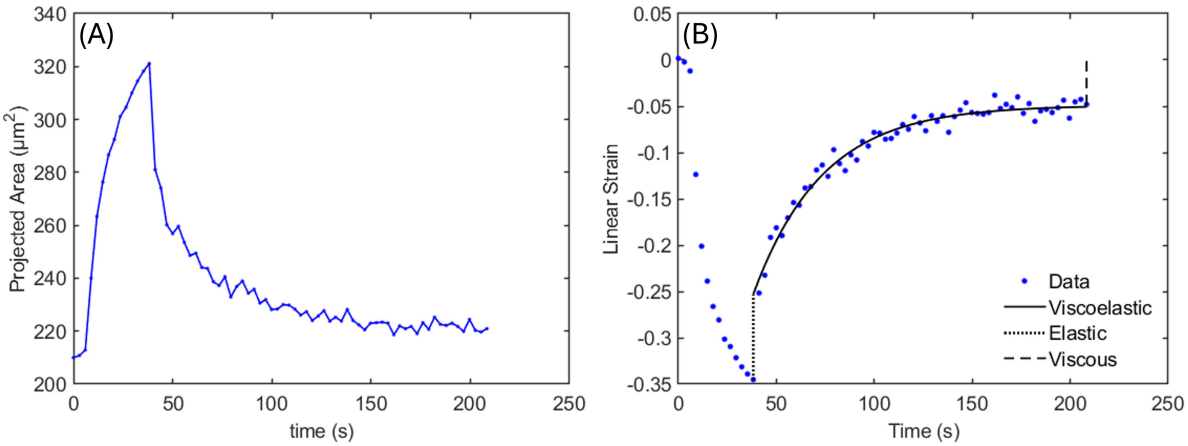


Figure 4.5: (A) Projected area of a single cell during a compression experiment. (B) The converted linear strain of the same cell with the elastic, viscoelastic, and viscous recovery strains labeled.

The typical response of the bovine cells strained in these experiments is radially-symmetric deformation in the transverse plane, where the projected area shown in Figure 4.6(A) is a circle that increases and then decreases with the application and removal of the strain, respectively. However, some cells studied in this experiment demonstrated

short- and long-term radially-asymmetric deformation. The short-term radially-asymmetric deformation recovered within 3 min, whereas the long-term effects persisted longer than the cells were imaged. This radially-asymmetric deformation is shown in Figure 4.6(B)-(C).

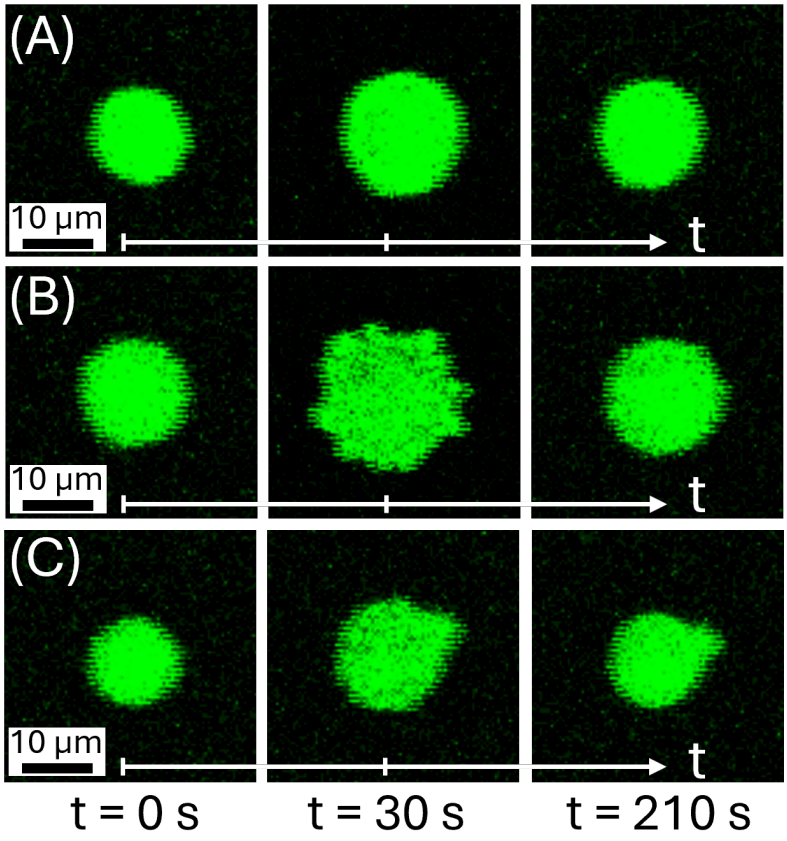


Figure 4.6: Images of three cells at three time points; prior to applied strain, at maximum strain, and after 3 minutes of recovery, respectively. Examples of (A) radially-symmetric deformation and full recovery to original shape immediately following the release of the applied strain, (B) radially-asymmetric cell membrane deformation during applied strain but full recovery to original shape, and (C) permanent radially-asymmetric deformation.

Compressive strains in the range of 10-60% were applied, and it was found that more than 40% of the cells showed short-term radially-asymmetric membrane deformation, as shown in Figure 4.7. The cells that experienced temporary radially-asymmetric membrane deformation fully recovered their original spherical shape. The resulting permanent strain

generally increased with the magnitude of the applied strain. The viscoelastic recovery time of bovine chondrocytes was an average of 42 s with a standard deviation of 11 s. The recovery time did not depend on the total applied strain, as shown in Figure 4.8. Additionally, cells with radially-asymmetric deformation recovered similarly to cells with radially-symmetric, with a mean of 38 s and a standard deviation of 8 s.

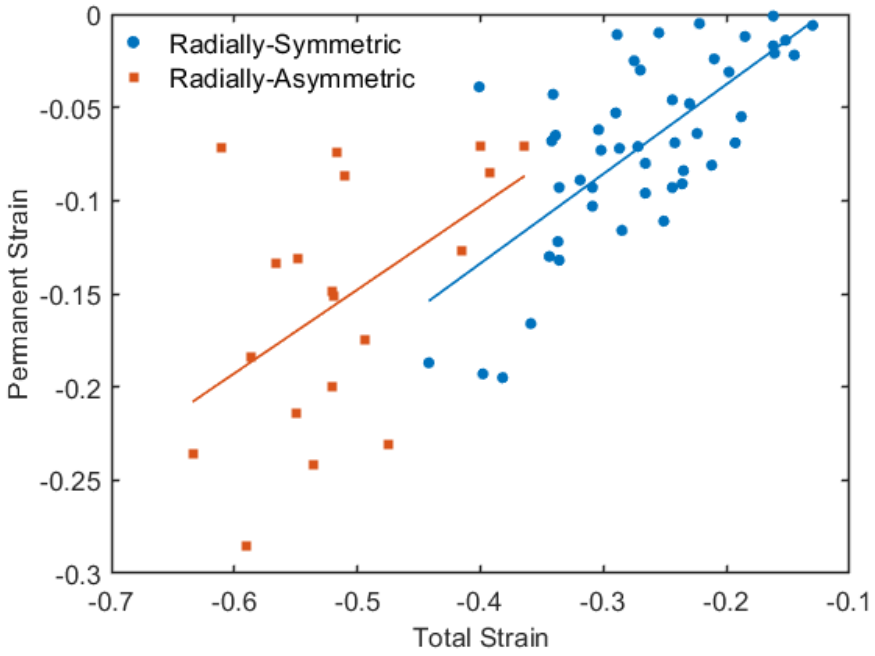


Figure 4.7: Total vs permanent strain of cells. Cells with radially-symmetric deformation are shown as blue circles (n=48), while cells with short-term radially-asymmetric deformation are shown as red squares (n=19). The solid lines are the linear regression fits. The R-squared values are 0.50 and 0.25 for the radially-symmetric and -asymmetric cells, respectively.

For curve fitting, only cells that showed an R-squared value greater than 0.85 for the viscoelastic exponential were included in the dataset presented in this work. The mean R-squared values for the radially-symmetric and -asymmetric data sets were 0.92 and 0.98, respectively, and the standard deviations were 0.04 and 0.01, respectively.

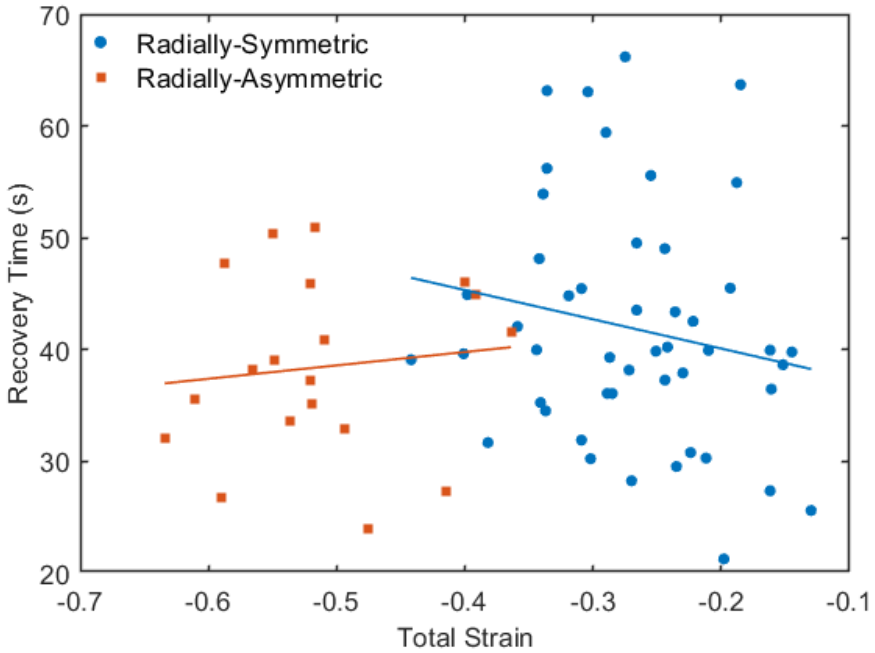


Figure 4.8: Recovery time of bovine chondrocytes as a function of total applied compressive strain. The blue circles represent the radially-symmetric deformed cells (n=48) while the red squares are cells (n=19) which experienced short-term radially-asymmetric deformation. The solid lines are the linear regression fits. The R-squared values are 0.03 and 0.01 for the radially-symmetric and -asymmetric cells, respectively.

Discussion

The recovery time of chondrocytes that displayed radially-symmetric deformation was measured at 42 s. In comparison, cells that displayed radially-asymmetric deformation had a recovery time of 38 s, which is in agreement with previous micropipette aspiration and AFM characterization in [112, 114, 168–171]. An applied strain magnitude greater than 40% seemed to demarcate radially-symmetric and -asymmetric deformed cells. This radially-asymmetric was only a temporary phenomenon, and the cells from this data set all recovered to their original circular shapes. In cases of greater than 40% strain magnitude, roughly 20% had radially-asymmetric deformation which was not recovered within the experiment time and their recovery time was not measured. It was determined that the permanent strain was independent of cell size, as shown in Figure B.4.

The measurement throughput in this method was 50 cells/h, but there are several ways which this could be significantly improved. The cell suspension concentration and imaging FOV are the two limiting factors. The cell concentration in this study could be optimized to increase the number of cells visualized in parallel. In practice, cell concentration increases the chance that cells would be in contact, making image analysis more challenging. For simplicity, all cells in contact with neighboring cells were not investigated. The FOV in this study was 450 x 450 µm. If a larger FOV microscopy system could be utilized, adding rigid glass or polystyrene microspheres to the cell suspension would enable a fluidic chamber of constant height capable of compressing all cells in the FOV. The strain magnitude applied to each cell would depend on the individual cell diameter compared to the microspheres. In theory, the throughput should be linearly proportional to the FOV.

One explanation for the radially-asymmetric cell deformation is blebbing. Blebbing is a process in which the plasma membrane of a cell forms spherical protrusions or bulges. Blebbing can be a normal physiological response, such as during cell movement [172, 173] and division [174], or it can be associated with pathological conditions like apoptosis [175, 176]. Blebs typically form in 30 s before shrinking over 120 s, and reach a size of approximately 2 µm [177].

Blebbing has been observed during MPA in various cells, including chondrocytes [178–181]. Sliogeryte *et al* found a critical pressure threshold where bovine chondrocytes began blebbing in MPA experiments [181]. The results in this study show a similar phenomenon: chondrocytes subjected to a critical linear strain of over 40% showed short-term radially-asymmetric deformation. This suggests that the radially-asymmetric deformation observed in this study is cell blebbing.

There are many possible applications to use this device for the viscoelastic characterization of healthy and diseased cells. It has been shown that some types of cancer cells have different mechanical properties compared to their healthy counterparts [52, 159, 160, 182].

Similarly, red blood cell deformability has been linked to diseases [183, 184]. The elastic modulus of chondrocytes and chondrocyte PCM from healthy and OA cartilage may be altered with the onset and development of OA [110, 112, 185]. The methodology could be directly applied to study chondrocytes from OA cartilage to explore how viscoelastic properties are altered compared to their normal counterparts.

Conclusion

The device developed in this work shows demonstrated ability to reproducibly and accurately deform spherical cells in a way compatible with microscopy. The deformed cells' projected area was imaged with confocal microscopy and measured with an edge detection algorithm. This projected area was fit to a Burgers viscoelastic model, and the elastic, viscoelastic, and permanent strains were measured. The viscoelastic recovery times of bovine chondrocytes were consistent with previous micropipette aspiration characterization.

The main advantage of this device compared to micropipette aspiration or other techniques is the ability to strain multiple cells at once. The number of cells characterized in parallel is determined by the FOV of the imaging system, assuming an appropriate cell concentration is chosen. In this work, the FOV was 450 x 450 µm, but this system could be adapted to other microscopy systems to increase FOV and, therefore, the overall characterization throughput.

Supporting Information to this Chapter is presented in Appendix B.

VISCOELASTIC PROPERTIES OF CHONDROCYTES FROM MONOLAYER AND ALGINATE CULTURES

Contribution of Authors and Co-Authors

Manuscript in Chapter 5

Author: Michael Neubauer

Contributions: Investigation, Conceptualization, Methodology, Formal analysis, Data curation, Writing — original draft.

Author: Priyanka Brahmachary

Contributions: Conceptualization, Methodology, Writing — original draft.

Author: Ron June

Contributions: Investigation, Conceptualization, Writing — review and editing.

Author: Stephan Warnat

Contributions: Investigation, Conceptualization, Writing — review and editing.

Manuscript Information

Michael Neubauer, Priyanka Brahmachary, Ron June, Stephan Warnat

Journal of Biomechanics

Status of Manuscript:
_X_ Prepared for submission to a peer-reviewed journal
____ Officially submitted to a peer-reviewed journal
____ Accepted by a peer-reviewed journal
____ Published in a peer-reviewed journal

Elsevier

Abstract

This study uses a previously reported 3D-printed variable-height flow cell to investigate the viscoelastic properties of chondrocytes from 2D monolayer and 3D alginate cultures. It was hypothesized that chondrocytes could be distinguished by their viscoelastic recovery time due to the variation of the pericellular matrix (PCM) produced by chondrocytes from different culture methods. The PCM surrounding the chondrocytes was fluorescently stained and imaged with confocal microscopy during applied deformation and subsequent recovery. The projected area of the cells was fit with a Burgers mechanical model to extract the viscoelastic recovery time. No difference between bovine and primary OA cells from monolayer cultures was observed. However, a statistically significant difference in recovery time was found between cells from monolayer and alginate cultures within both bovine (31 s vs. 14 s) and primary OA (34 s vs. 12 s) groups, respectively. This work shows that viscoelastic recovery time is influenced by the culture method used for chondrocyte proliferation and further demonstrates the role of the PCM as a mechanical protector of chondrocytes.

Introduction

Osteoarthritis (OA) is the most common degenerative joint disease, impacting more than 500 million people worldwide. Of these cases, over 300 million involve the knee joint, a particularly vulnerable site due to its high load-bearing function [186]. OA leads to the breakdown of the articular cartilage that lines bone surfaces within joints, which results in pain, stiffness, and reduced mobility over time [187]. Articular cartilage primarily comprises an extracellular matrix (ECM), a supportive and flexible network that provides structural integrity and shock absorption. Chondrocytes, the only resident cells within the cartilage, are crucial for cartilage health, functioning, and sustaining this matrix [103]. Surrounding each

chondrocyte is a thin, 2–4 µm layer of pericellular matrix (PCM), forming what is known as a chondron[188]. The PCM acts as a buffer between chondrocytes and the ECM, facilitating essential cell functions such as mechanotransduction, where cells convert mechanical stimuli into biochemical signals [188–190]. The PCM plays a vital role in protecting chondrocytes from mechanical stress. Through mechanotransduction, chondrocytes can sense and respond to mechanical forces by adjusting their gene expression and metabolic activity, which is critical for maintaining cartilage homeostasis and potentially slowing OA progression [191].

Chondrocytes cultured in a monolayer environment often undergo dedifferentiation, shifting from their native spherical shape *in vivo* to a flattened, elongated 2D morphology [192]. Additionally, monolayer cultures do not produce chondrocytes with well-defined PCM layers. Evidence suggests that the PCM is crucial for maintaining chondrocyte phenotype, as studies have shown that isolated chondrons (chondrocytes with intact PCM) generate a more cartilage-like extracellular matrix (ECM) compared to monolayer-cultured chondrocytes, which produce a less authentic cartilage matrix [193, 194]. To promote a more *in vivo*-like phenotype, chondrocytes are often cultured within millimeter-scale alginate beads or hydrogels [195–197]. This 3D environment encourages the cells to retain their rounded shape, closely resembling the morphology of *in vivo* chondrocytes. However, chondrocytes grown in alginate beads either lack a well-developed PCM or exhibit a reduced PCM stiffness [198–202]. Ideally, chondrocytes or chondrons used in experimentation should mimic the *in vivo* phenotype and possess similar biophysical properties so that results can directly be applied to cells in their natural state and environment.

The PCM directly transfers the load from the ECM to the chondrocyte [203–205]. Chondrocyte cells have been suspended in high-stiffness agarose gel to study *in vitro* cellular response to mechanical loading [206–209]. Viscoelastic mechanical properties of chondrocytes have been previously measured with micropipette aspiration (MPA) [110, 112–114, 169, 171, 181] and atomic force microscopy (AFM) [111, 168, 210, 211], but typically these cells have

been cultured in 2D monolayers. The PCM of chondrons was measured with AFM [197, 212] and MPA [213], and the elastic modulus of the PCM was found to be up to 10 times higher than the chondrocyte [104, 190, 214]. The effect of OA on the chondrocyte PCM is not agreed upon in the literature, as studies with MPA measured an increased chondrocyte stiffness with the progression of OA [110, 112, 171]. In contrast, studies with AFM [111, 185] and confined compression [215] find the opposite. A more thorough explanation of the chondrocyte isolation and culture in these studies could explain the discrepancy in the results.

This work used a previously reported 3D-printed variable-height microfluidic device for viscoelastic characterization of bovine and primary OA chondrocyte cells from 2D monolayer and 3D alginate cultures [216]. Bovine chondrocytes were used as a healthy control for primary OA cells, and a standard monolayer culture was a control for a recently reported alginate culture method [116]. Both monolayer and alginate cultures include sodium L-ascorbate, which promotes increased PCM production. The alginate culture was previously shown to produce a more robust PCM shell than cells cultured in monolayers. It was hypothesized that the viscoelastic properties of cells from monolayer and alginate cultures would be distinct, given the increased stiffness of PCM compared to chondrocytes. Cells of each type and culture method were loaded into the device and underwent mechanical compression and relaxation while imaged with confocal laser scanning microscopy (CLSM). The projected area of the cells was fit to a Burgers four-element mechanical model, and the viscoelastic recovery time was compared between the groups of N=3 donors each.

Methodology

Flow-cell and CLSM Imaging

Previous work [216] describes the fabrication of the variable-height 3D-printed device used in this study. Briefly, a channel structure was 3D printed directly on a No. 1.5 glass coverslip treated with bind silane, as in [166]. A 3 x 4 mm piece of glass was placed in a

cutout in the 3D-printed channel and sealed with silicone. Another 3D-printed structure, the control chamber, encloses the area above the glass piece, and a custom pressure controller controls the pressure inside. The height of the fluidic channel between the glass coverslip and the top glass piece is controlled by adjusting the pressure of the control chamber. For each experiment, cells are injected through tubing and flown into the variable height region, where they are compressed between the two pieces of glass and imaged with a confocal microscope (Stellaris DMi8, Leica, USA) using a 20x objective (HC PL APO 20x/0.75 CS2, dry objective, Leica, USA). The compression time for each experiment was 30 s, and cell recovery was observed for another 180 s.

Chondrocyte Harvest and Culture

Four different groups of chondrocyte cells were used for experimentation: (i) bovine chondrocytes from monolayer cultures, (ii) bovine-alginate, (iii) primary OA-monolayer, and (iv) primary OA-alginate, as shown in Figure 5.1. Three donors (N=3) comprised each group. Human Primary Chondrocytes (HPC) were obtained from discarded arthroplasty tissue from Stage-IV osteoarthritis patients undergoing total joint replacement under IRB approval. Bovine chondrocytes were harvested from knee joints of 18-22-month-old cattle obtained from a local abattoir. Briefly, tissue was digested with Collagenase Type I (2 mg/mL) (Gibco, Waltham, MA, USA) for 14 h at 37 ^{o}C using a previously established protocol [108]. Isolated chondrocytes were cultured for 10 days in Dulbecco's Modified Eagle's medium (DMEM) (Gibco, Waltham, MA, USA) supplemented with Fetal Bovine Serum (FBS) (10% v/v) (Bio-Techne, Minneapolis, MN, USA), penicillin (10,000 I.U./mL), and streptomycin (10,000 µg/mL) (Sigma, St. Louis, MO, USA) (hereby referred to as Complete Media) in 5% CO2 at 37 ^{o}C and first passage population was used for experiments.

For monolayer studies, chondrocytes were cell cycle synchronized by 12 h serum starvation followed by culturing in Complete media and incubated in 5% CO2 at 37 °C

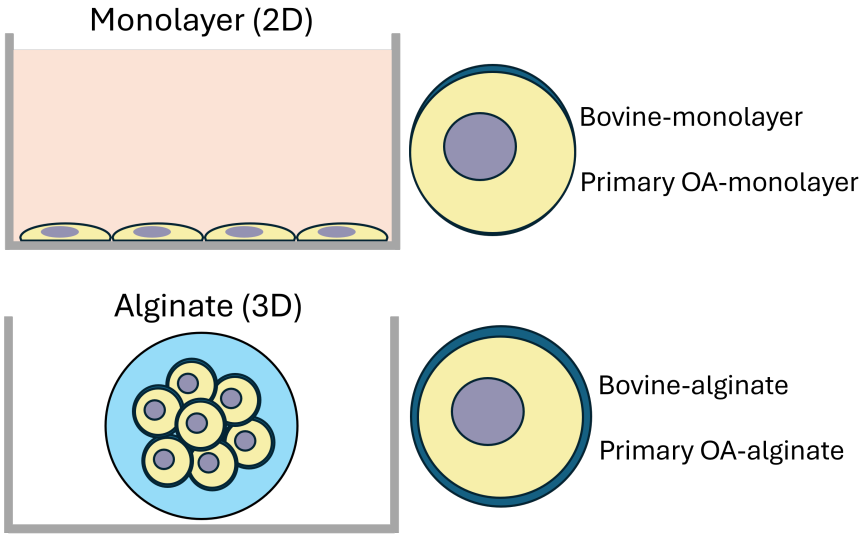


Figure 5.1: Monolayer vs alginate culture. Both cultures contain the addition of sodium L-ascorbate. Bovine and primary OA cells are produced from each culture methods, resulting in four different populations of chondrocytes for experimentation.

for 7 days with 50 µg/mL sodium L-ascorbate (Sigma), and the media changed every other day. For alginate encapsulation, cells that were cell cycle synchronized were resuspended at a density of $4x10^6$ cells/mL in sterile-filtered 1.2%, w/v, sodium alginate (Sigma). The cell suspension was then slowly dispensed through a 22 gauge needle in a dropwise fashion into a 102 mM CaCl2 solution. After near-instantaneous gelation, the alginate beads were allowed to crosslink for 15 min. The beads were then washed 4 times with 150 mM NaCl and once with Complete media before being cultured with complete media containing 50 µg/mL sodium L-ascorbate in 5% CO2 at 37 °C for 7 days, following which the alginate beads were dissolved with an EDTA-citrate buffer (150 mM NaCl in 55 mM sodium citrate with 50 mM EDTA, pH6.8).

Calcein AM and Wheat Germ Agglutinin Staining

$1x10^6$ cells/ml monolayer and alginate-released cells that were previously cultured with 50 µg/mL sodium L-ascorbate for 7 days were resuspended in Phosphate Buffer Saline (PBS,

1X) and Calcein Blue AM Viability Dye (Invitrogen) was added at a final concentration of 5 µM. Cells were incubated in 5% CO2 at 37 °C in the dark for 30 min. Cells were washed twice with 1X PBS and incubated with 5 µM final concentration of Wheat Germ Agglutinin, Alexa Fluor 594 conjugate (Life Technologies Corporation) in 5% CO2 at 37 °C in the dark for 10 min. Cells were washed with 1X PBS and were kept ready for visualization.

Data Analysis

The microscopy data is analyzed similarly to a previous study [216]. Every Z-stack of images in the time series of an experiment is first converted to a single image but using a mean-intensity projection (MIP) in Imaris (Oxford Instruments, USA). The time series is imported into Matlab (Mathworks, USA), and each frame is fed into a custom Sobel edge detection method to extract the border of each cell in the field-of-view, FOV. The projected area of each cell is recorded and then converted to linear strain, as described in [216].

A four-element Burgers mechanical model fits the time-dependent linear strain, shown in Equation 5.1. The Burgers model consists of four elements of a spring in series with a parallel spring-dashpot, in series with another dashpot. The time-dependent strain, $\epsilon(t)$, is equal to the sum of the magnitudes of elastic, viscoelastic, and viscous strains. The viscoelastic portion of the recovery is a decaying exponential with the time constant, τ, which represents the viscoelastic recovery time. Previous work has demonstrated that the interior cell stain can be used to track cell recovery and find the viscoelastic recovery time [216], but in this study, the cell membrane stain is used to define the cells' projected area.

$$\varepsilon(t) = \varepsilon_{elastic} + \varepsilon_{ve} e^{(-t/\tau)} + \varepsilon_{viscous} \tag{5.1}$$

The projected area of each chondron, taken as the border of the PCM, is used to fit the recovery to the Burgers model, illustrated in Figure 5.2. The projected area is first converted to linear strain as described in [216], but the general shape of the recovery is the same.

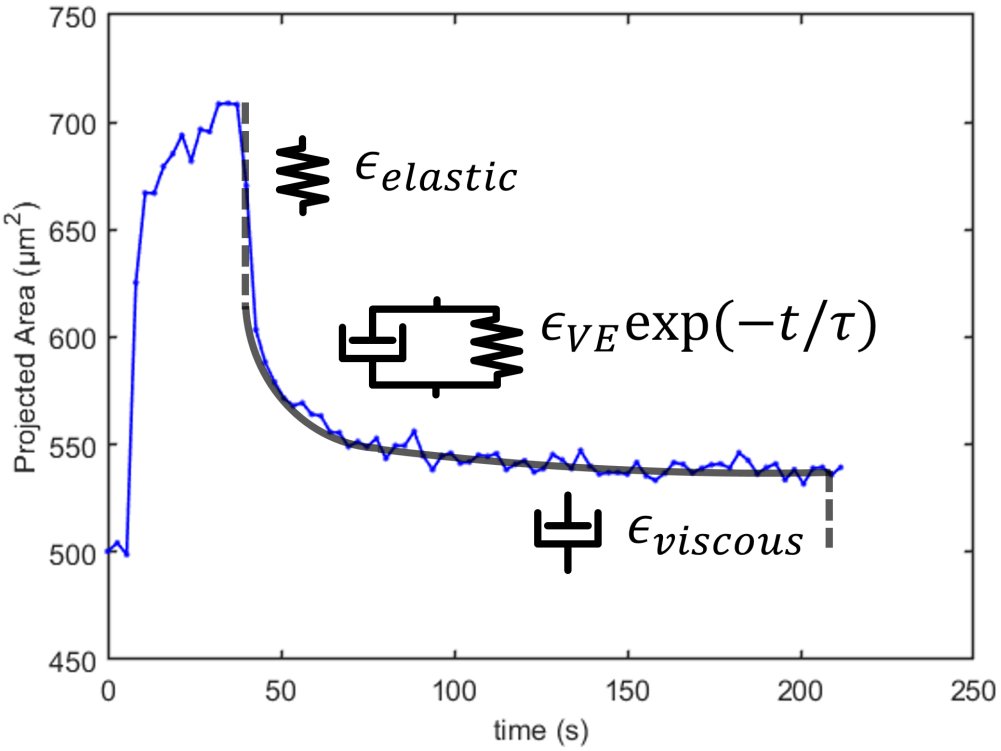


Figure 5.2: An illustration how the projected area of a chondron during recovery from an applied strain is fit to each mechanical element from a Burgers model. The chondrons have a nearly instantaneous elastic recovery, following by an exponentially decaying viscoelastic recovery, characterized by the recovery time, τ. Any permanent deformation is accounted for by the dashpot element, representing the viscous strain.

Results and Discussion

Cell Appearance

Bovine chondrocytes from monolayer and alginate cultures are shown in Figure 5.3. The blue viability dye and red collagen (PCM) dye channels are overlaid in the first row and viewed separately in rows two and three, respectively. The two cells from each culture shown are representative of the cells analyzed during a recovery experiment. The PCM surrounding bovine chondrocytes is consistent between the monolayer and alginate cultures. However, there is some heterogeneity within the populations of cells, as demonstrated in Figure 5.4,

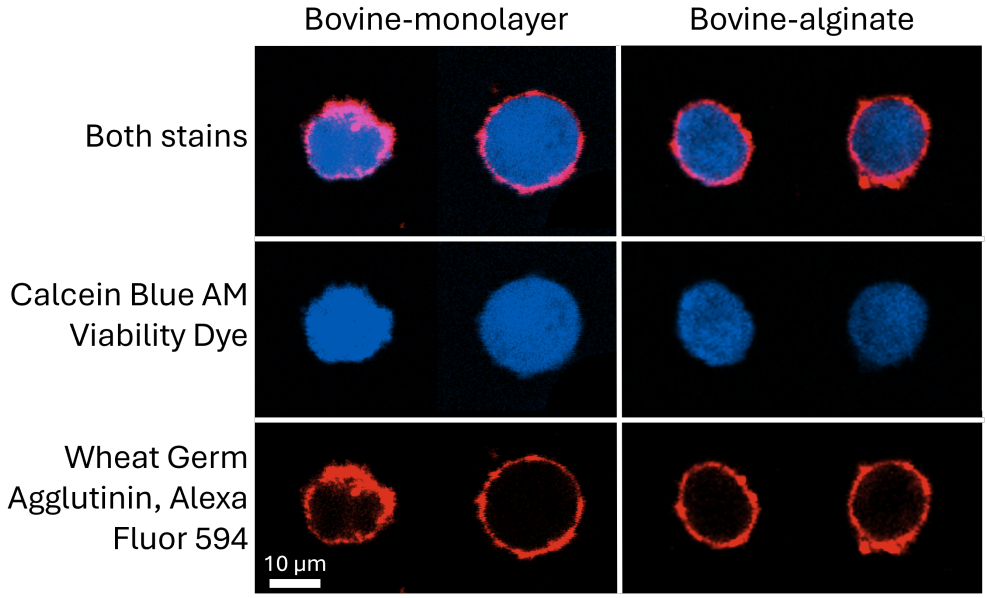


Figure 5.3: Confocal images (single slice from a Z-stack) of bovine chondrocytes from monolayer (left column) and alginate (right column) cultures. The scale bar in the bottom left corner is accurate for all images in this figure. The calcein blue AM viability dye stains the chondrocyte (center row) while the wheat germ agglutin stains the collagen in the PCM surrounding the chondrocyte (bottom row). The top row shows the two stains overlaid. The two cells from each culture are representative of the cells analyzed during a recovery experiment. In general, the PCM was visually similar between the monolayer and alginate cultured cells.

where a group of monolayer cultured bovines is displayed. Here, it is apparent that there are differences in chondrocyte size, shape, viability, and PCM thickness and uniformity. This image is representative of the heterogeneity observed in the bovine populations in this work. Similar heterogeneity was observed with primary OA cells.

Similarly, representative primary OA chondrocytes and surrounding PCM from monolayer and alginate cultures are displayed in Figure 5.5. Unlike the bovine groups, the PCM thickness appears to be increased and more uniform from primary OA-alginate cultured chondrocytes, compared to monolayer cultures.

A thorough investigation of the PCM thickness and uniformity for all cell populations used in this work was not conducted. Still, it could be of interest to further characterize the

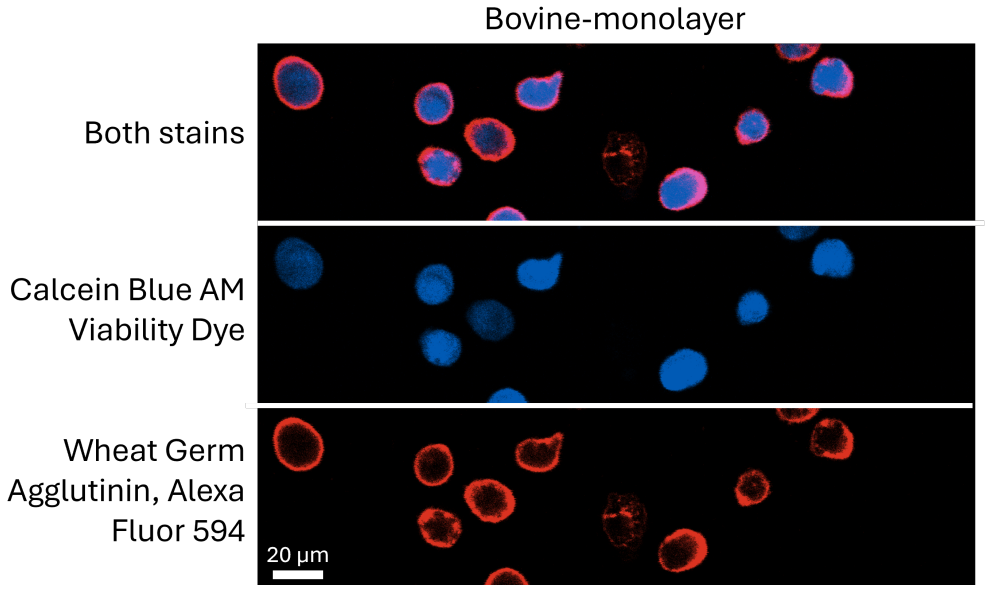


Figure 5.4: Confocal images of bovine chondrocytes from a monolayer culture. The scale bar in the bottom left corner is accurate for all images in this figure. The calcein blue AM viability dye stains the chondrocyte (center row) while the wheat germ agglutin stains the collagen in the PCM surrounding the chondrocyte (bottom row). The top row shows the two stains overlaid. This image is representative of the diversity of the chondron appearance. There are brighter and dimmer cells from the viability stain and the PCM thickness and uniformity varies from cell-to-cell. Note that this is a single Z-slice at one height and the cells shown are not all in the same plane. The apparent thickness of the PCM is influenced by the curvature of the cell within focus in the 0.68 µm thick Z-slice.

culture methods. Previously, chondrocyte PCM thickness has been measured with optical microscopy [197, 217], confocal microscopy [218], and transmission electron microscopy (TEM) [219]. It has also been reported that OA increased PCM thickness by up to 50% [110, 217]. The confocal microscope used in this work would be capable of measuring PCM thickness. However, this work's image acquisition mode and Z-slice thickness were chosen for speed and are not ideal for performing this task.

Viscoelastic Recovery Time

The permanent strain as a function of total applied strain for bovine and primary OA chondrons from monolayer cultures is shown in Figure 5.6(a). In general, larger permanent

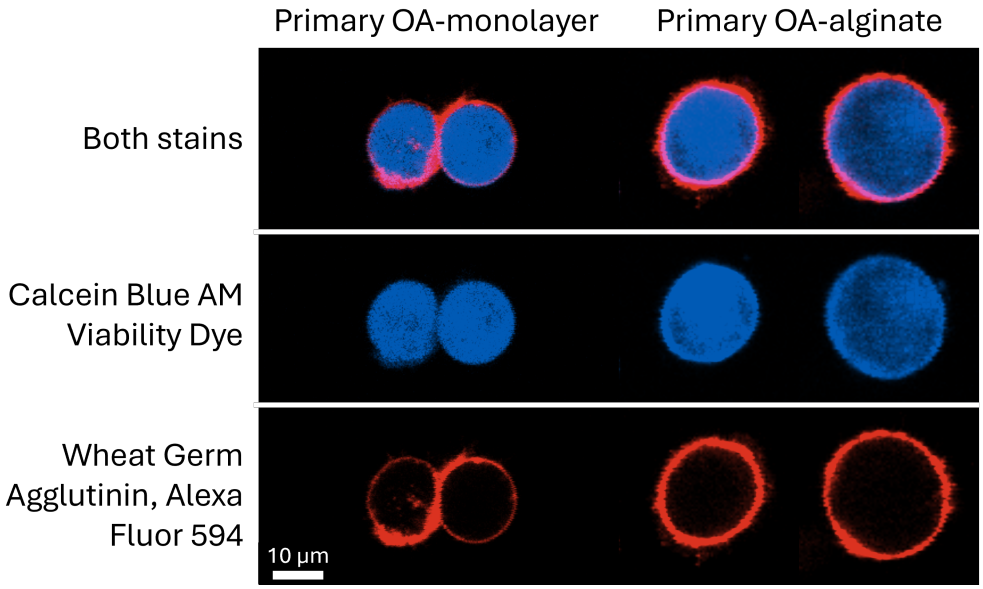


Figure 5.5: Confocal images (single slice from a Z-stack) of primary OA chondrocytes from monolayer (left column) and alginate (right column) cultures. The scale bar in the bottom left corner is accurate for all images in this figure. The calcein blue AM viability dye stains the chondrocyte (center row) while the wheat germ agglutin stains the collagen in the PCM surrounding the chondrocyte (bottom row). The top row shows the two stains overlaid. The two cells from each culture are representative of the cells analyzed during a recovery experiment. In general, the PCM produced from the alginate cultures appeared thicker and covered the chondrocytes more uniformly.

strains result from higher applied strains. A previous study using the same device and general method found a similar result, but the data was from chondrocytes without a stained PCM [216]. Figure 5.6(b) shows the viscoelastic recovery time of the same chondrons, and no dependence on total applied strain is observed. The recovery time for bovine (mean=31 s, standard deviation (std)=13 s, n=64) and primary OA (mean=34 s, std= 15 s, n=13) chondrons from monolayer cultures is compared in Figure 5.7. A two-sample t-test resulted in a p-value of 0.46, indicating no statistically significant difference between the two groups.

A statistically significant difference in recovery time was found between monolayer and alginate cultures for both bovine and primary OA cells, shown in Figures 5.8(a)-(b), respectively. The recovery time of bovines from monolayer (mean=31 s, std=13 s, n=64)

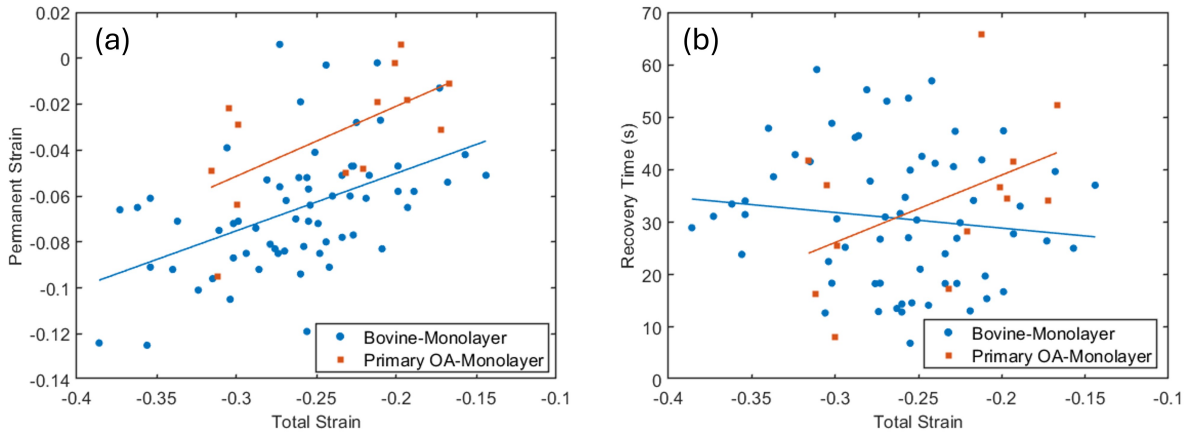


Figure 5.6: (a) Total strain vs permanent strain for bovine and primary OA chondrons from monolayer cultures. There appears to be a rough correlation, the higher the applied strain, the greater the magnitude of the permanent strain. The solid lines are the linear regression fits. The R-squared values are 0.24 and 0.40 for the bovine and primary OA cells, respectively. (b) the viscoelastic recovery time as a function of total applied strain. The solid lines are the linear regression fits. The R-squared values are 0.01 and 0.23 for the bovine and primary OA cells, respectively.

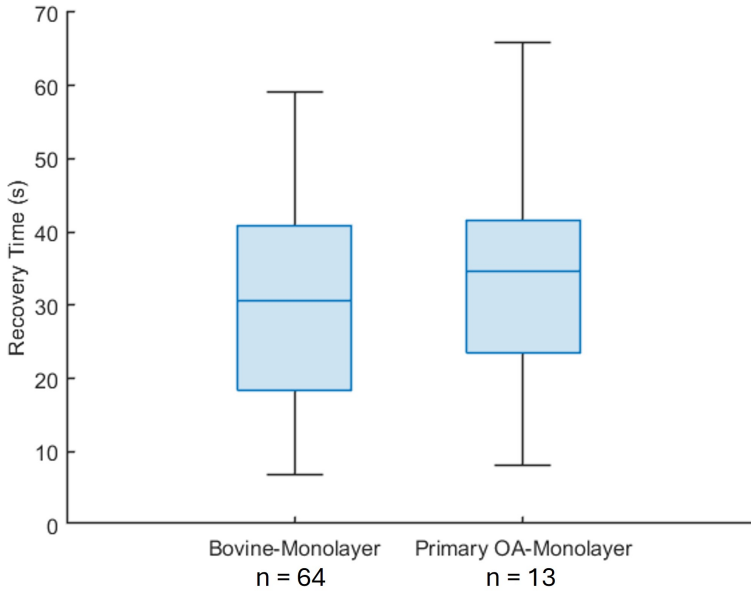


Figure 5.7: A boxplot of the viscoelastic recovery time for bovine and primary OA chondrocytes from monolayer cultures. The high p-value (0.46) from a two-sample t-test suggests no statistically significant difference.

and alginate (mean=13 s, std=7 s, n=15) were compared with another two-sample t-test and the difference was deemed statistically significant with a p-value of 0.0000020. Similarly, the recovery time of primary OA chondrons from monolayer (mean=34 s, std= 15 s, n=13) and alginate (mean=13 s, std=7 s, n=8) cultures were distinct with a p-value of 0.0023.

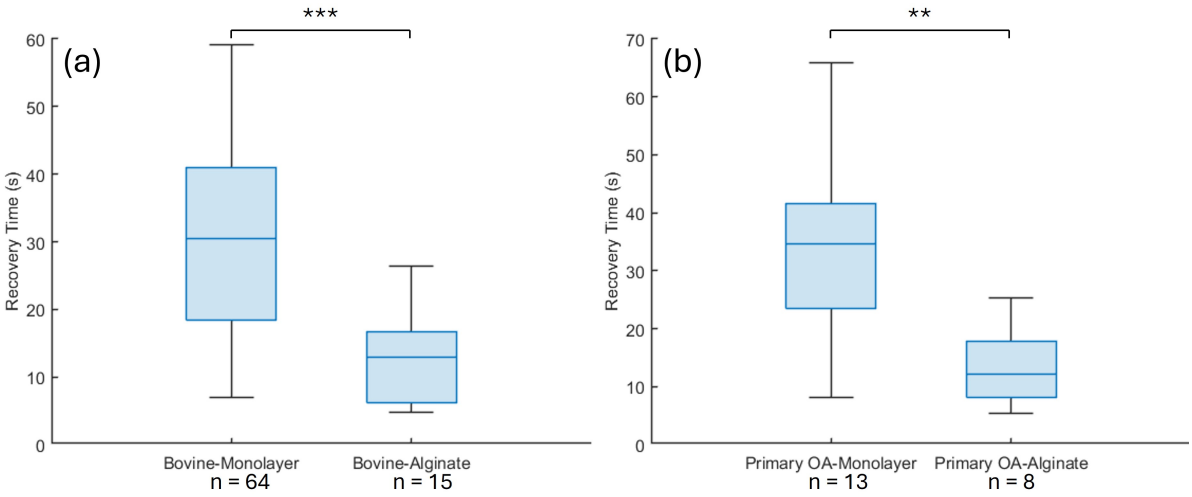


Figure 5.8: (a) A boxplot of the viscoelastic recovery time for bovine chondrocytes from monolayer and alginate cultures. The low p-value (0.0000020) from a two-sample t-test suggests a statistically significant difference. (b) A boxplot of the viscoelastic recovery time for bovine chondrocytes from monolayer and alginate cultures. Similarly, a low p-value (0.0023) suggests a statistically significant difference between primary OA cells from monolayer and alginate cultures.

While the sample size was large enough to differentiate between cells from the two cultures, it was limited by the short recovery time of cells from alginate cultures. Each Z-stack in the CLSM time series spans roughly 2.7 s, making it challenging to fit a recovery curve when the recovery time is low. The bovine and primary OA data sets for the alginate cultures could be doubled if the measurement frequency could be increased.

Discussion

There was no difference in viscoelastic recovery time between bovine and primary OA chondrons. It has been reported that the elastic modulus of the PCM of primary

chondrocytes changes with the onset of OA [110–112, 171, 185]. In this study, bovine chondrocytes were used in place of healthy primary chondrocytes due to limited access to healthy primary cells. While the recovery time was measured in this work, it is theoretically a function of both spring constants in the Burgers model, which both contribute to the bulk elastic modulus [167]. Given that no difference in the recovery time was observed, it suggests that the bulk elastic modulus were similar between monolayer bovine and primary OA chondrons.

In contrast, a different recovery time was found between cells from different culture methods. Monolayer and alginate bovine chondrons had different recovery times, and the same was valid for monolayer and alginate primary OA chondrons. This finding is reasonable given the previously cited literature demonstrating that culture methods produce chondrocytes with different PCMs.

The previously reported use of this device and method showed a throughput of roughly 50 cells/h. This study's throughput was lower, as seen by the generally low sample size. One explanation for this is the staining of the PCM, and using it to define the cell border excluded more cells that did not possess a nearly spherical shape due to the variation in the PCM. The increased PCM on chondrocytes in this work compared to [216] added an additional challenge as the cells were more likely to stick together when nearby a neighboring cell. All cells in contact with other cells were excluded from the analysis.

Another reason is that cell concentration was not adequately accounted for in the final cell suspension. Primary OA chondrocytes grow and multiply slower than healthy bovine chondrocytes, and therefore, a lower final cell concentration was produced as the culturing method and timescale were identical. Similarly, cells cultured in alginate also reproduce slower compared to monolayer cultures. It was found that a cell concentration of $3\text{x}10^6$ cells/ml was an ideal concentration to maximize throughput. The overall throughput using this device and method is limited firstly by the field-of-view (FOV) of the microscopy system,

in this work 0.455 x 0.455 mm, and secondly by the number of cells within that FOV.

Conclusion

This work reports on using a previously developed 3D-printed variable-height flow cell. CLSM imaging and data fitting to a Burgers mechanical model are performed similarly, but in this case, the PCM surround chondrocyte cells were fluorescently stained and used instead of the cytoplasm viability stain. The main goal of this work was to explore if monolayer and alginate cultures produced mechanically distinct chondrons. It has been previously demonstrated that 3D culture methods using alginate or hydrogels produce chondrocytes with increased PCM production compared to 2D monolayer cultures. The 3D cultures allow chondrocytes to grow more naturally, like the *in vivo* environment where the chondrocytes have a spherical shape with a surrounding PCM. Given the prevalence of osteoarthritis and the significant ongoing work to understand its cause and find better treatment and prevention measures, producing chondrocytes for research of the same phenotype as those *in vivo* is paramount. This work provides a method for evaluating the viscoelastic properties of chondrocytes from different cultures.

The viscoelastic recovery time from bovine and primary OA chondrocytes from monolayer cultures was indistinguishable. However, the recovery time of chondrons from alginate cultures was reduced compared to chondrons from monolayer cultures. This is demonstrated for bovine and primary OA chondrons. This suggests that the PCM, which transfers forces to the chondrocyte, is mechanically distinct from different cultures.

CONCLUSION AND FUTURE OUTLOOK

This study describes the design, fabrication, and use of a 3D-printed variable-height flow cell for measuring viscoelastic properties such as chondrocyte cell recovery time. Each of the following conclusions correlates with the objectives stated in chapter 1.

1. A severe limitation for resin 3D printed microfluidic flow-through channels is the difficulty of optically viewing inside the channels. Even with clear resin, which doesn't absorb visible light, the surface roughness of 3D-printed channels causes unacceptable blurring due to light diffraction at the interface. This work developed a method for 3D printing open-faced channels directly on glass. The improvement in optical viewing quality was demonstrated by visualizing microspheres with a microscope and measuring visible light transmission with a spectrometer. 3D printed channels were created on glass substrates with microfabricated gold electrodes, and before-and-after surface resistivity, Raman spectroscopy, and electrochemical impedance spectroscopy (EIS) measurements to show the glass and gold were unaffected by the silane surface treatment, enabling the resin to adhere to the glass. The impedance-conductivity sensor was integrated into a 3D-printed flow channel, and its use was demonstrated to be a proof-of-principle application.

2. The design, fabrication, and use of the 3D-printed variable-height flow cell are described in detail. This work further develops the 3D printing on glass method to enable printing on No. 1.5 glass coverlip (170 µm thick). The warping of the coverslip due to the cure shrinking of the resin is eliminated with a jig that holds the glass flat on a microscope stage. A custom feedback-controlled pressure system is implemented to vary the height of the top glass plate forming the microfluidic channel. Chondrocyte cells were imaged with a CLSM microscope while a deformation was applied, held, and then removed from the cells. Each z-stack in the time series was converted to a single image by max intensity projection. Then, an edge detection scheme was used to extract the projected area of individual cells

for every time point. The projected area was converted to linear strain and fit to a four-element Burgers mechanical model. Viscoelastic parameters were quantified, including recovery time and elastic, viscoelastic, and viscous strain magnitudes. The measurement throughput was 50 cells/h. It was concluded that the recovery time of chondrocytes (42 s) was consistent with existing literature using other measurement techniques. Radially-asymmetric deformation was apparent for cell when the applied strain exceeded 40%. The recovery time of these cells was 38 s. It was argued these temporary extrusions were blebs observed by other researchers under micropipette aspiration measurements.

3. Primary osteoarthritic and bovine chondrocyte cells from monolayer and alginate cultures with added sodium L-ascorbate were characterized similarly as in objective 2. It was hypothesized that the monolayer and alginate cultures would have a different viscoelastic recovery time as the alginate cultures produce chondrocytes with a more apparent PCM. The PCM was fluorescently stained and used to find the projected area of the cells during recovery from applied strain. Bovine and primary OA chondrons from monolayer cultures could not be distinguished by recovery time. However, chondrons recovery time did depend on culture method for both bovine and primary OA cells. Bovine chondrons from monolayer cultures had a recovery time of 31 s, while bovine chondrons from alginate cultures had a recovery time of 14 s. Similarly, primary OA chondrons from monolayer cultures had a recovery time of 34 s, compared to 12 s for chondrons from alginate cultures. A two-sample t-test was used to argue that monolayer and alginate cultured cells were distinct, with a p-value of 0.000014 and 0.0047 for bovine and primary OA cells, respectively. These results show that the mechanical properties of chondrocytes and surrounding PCM are dependent on culture method.

Future work should focus on measuring other mechanical properties of cells, such as elastic modulus. A crucial parameter needed for this is the force applied to the individual

cells. One method could be to estimate the force on each cell by calibrating the device with well-defined elastic spheres to build a force mapping model based on the supplied pressure in the control chamber. Another method is to add PDMS pillars to the top glass plate and calibrate their deformation as a function of pressure in the control chamber. Then, their relative deformation compared to the cell clamped by each pillar could be used to extract each cell's elastic modulus or stiffness.

The current work has demonstrated the device integrated with a confocal microscope and fluorescent cells. Future work could be done to use more commonly available light microscopy techniques, potentially eliminating the need for cell staining and access to a high-cost confocal microscope. This would expand the device's usability for other researchers and allow the possibility of future use of the device platform for point-of-care diagnostics in healthcare and medicine. The most straightforward and most available light microscopy is brightfield microscopy. The challenge of this technique is that edge detection of cells, particularly under cells undergoing compression and moving out of plane, will be difficult unless the microscope's point spread function is investigated. Differential interference contrast (DIC) microscopy is a less commonly available light microscopy technique but has the advantage of clearly defining sample boundaries, making edge detection easier.

Although chondrocytes were chosen as the model organism to demonstrate the capabilities of the developed microfluidic device, the same method could be applied to other cells. A spherical cell type is required to use this work's methodology and mechanical model. Many human cells are spherically shaped, including lymphocytes [220], stem cells [221], and some cancerous cells [222]. Additionally, other cell types also exhibit spherical shapes, including fungi (yeast) [223], algae (diatoms) [224], and cocci bacteria [225].

Beyond measuring viscoelastic parameters as done in this work, the application of the developed device could be extended further. For example, the current device platform can immobilize cells for live-cell imaging [226, 227] as it is already designed to be used with a

microscope system. In principle, adapting the device platform for mechanical deformation of solid substances such as cells suspended in agar gel or cartilage is also feasible. Alternatively, biofilm could be grown and mechanically stimulated or characterized in the chamber.

The most significant advantage of this device platform compared to other technologies, such as micropipette aspiration, is the potential for increased throughput. The device's current configuration is designed for microscope integration, which limits the measurement throughput due to limited FOV, in this work 0.20 mm^2. This FOV could be increased to 11 mm^2 if the entire area of the top glass plate could be imaged, amplifying the theoretical throughput by a factor of 55. While the realized throughput of 50 cells/h is already better than micropipette aspiration, expanding the FOV of the imaging system would bring the throughput to over 2750 cells/h

Lens-less microscopy is one example of an imaging system that achieves a large FOV. While optical microscopy uses lenses to magnify images of a sample and project them into eye-pieces or a camera for visualization, lens-less microscopy removes the lenses and images a sample directly with the pixel area on a camera. Perhaps the most straightforward lens-less imaging technique is shadow-projection imaging, where the sample is in contact with the camera sensor and illuminated by a light source [228–230]. The diffraction of the sample's shadow is limited by its proximity so that a clear image is formed. The FOV is defined by the size of the sensor and the resolution by the size of the pixels. Super-resolution methods using shifting light sources [231, 232] or machine learning [233] have been demonstrated to decrease the effective pixel size of images. The device developed in this work is well-suited for integration with a camera sensor to achieve lens-less imaging. The channel frame could be 3D printed onto a camera sensor and assembled as described.

In conclusion, this work demonstrates the capabilities of a 3D-printed variable-height flow cell for measuring the viscoelastic properties of chondrocytes. The device has a throughput greater than typical characterization techniques such as AFM and

micropipette aspiration and is specifically designed in a manner where the throughput could be significantly increased. Researchers should use this device to explore the mechanical properties of cells, and it has the potential for development as a point-of-care diagnostic platform for the healthcare industry.

REFERENCES CITED

[1] H. Huang, C. Dai, H. Shen, M. Gu, Y. Wang, J. Liu, L. Chen, and L. Sun. Recent advances on the model, measurement technique, and application of single cell mechanics. *Int J Mol Sci*, 21(17), 2020.

[2] Yansheng Hao, Shaokoon Cheng, Yo Tanaka, Yoichiroh Hosokawa, Yaxiaer Yalikun, and Ming Li. Mechanical properties of single cells: Measurement methods and applications. *Biotechnology Advances*, 45:107648, 2020.

[3] Zihao Li, Ziyu Huang, and Lunhao Bai. Cell interplay in osteoarthritis. *Frontiers in Cell and Developmental Biology*, 9, 2021.

[4] Hiroaki Ito and Makoto Kaneko. On-chip cell manipulation and applications to deformability measurements. *ROBOMECH Journal*, 7(1):3, 2020.

[5] Amir M. Esfahani, Grayson Minnick, Jordan Rosenbohm, Haiwei Zhai, Xiaowei Jin, Bahareh Tajvidi Safa, Justin Brooks, and Ruiguo Yang. Microfabricated platforms to investigate cell mechanical properties. *Medicine in Novel Technology and Devices*, 13:100107, 2022.

[6] Shan-Shan Li, Chun-Dong Xue, Yong-Jiang Li, Xiao-Ming Chen, Yan Zhao, and Kai-Rong Qin. Microfluidic characterization of single-cell biophysical properties and the applications in cancer diagnosis. *ELECTROPHORESIS*, n/a(n/a), 2023.

[7] B. N. Narasimhan, M. S. Ting, T. Kollmetz, M. S. Horrocks, A. E. Chalard, and J. Malmström. Mechanical characterization for cellular mechanobiology: Current trends and future prospects. *Front Bioeng Biotechnol*, 8:595978, 2020.

[8] Blanca González-Bermúdez, Gustavo V. Guinea, and Gustavo R. Plaza. Advances in micropipette aspiration: Applications in cell biomechanics, models, and extended studies. *Biophysical Journal*, 116(4):587–594, 2019.

[9] Ling An, Fenglong Ji, Enming Zhao, Yi Liu, and Yaling Liu. Measuring cell deformation by microfluidics. *Frontiers in Bioengineering and Biotechnology*, 11, 2023.

[10] Sevgi Onal, Maan M. Alkaisi, and Volker Nock. Microdevice-based mechanical compression on living cells. *iScience*, 25(12):105518, 2022.

[11] Y. Gu, C. Zhang, Y. Zhang, W. Tan, X. Yu, T. Zhang, L. Liu, Y. Zhao, and L. Hao. A review of the development and challenges of cell mechanical models. *IEEE Transactions on NanoBioscience*, 22(3):673–684, 2023.

[12] C. T. Lim, E. H. Zhou, and S. T. Quek. Mechanical models for living cells—a review. *Journal of Biomechanics*, 39(2):195–216, 2006.

[13] Philip Kollmannsberger and Ben Fabry. Linear and nonlinear rheology of living cells. *Annual Review of Materials Research*, 41(1):75–97, 2011.

[14] Kristina Haase and Andrew E. Pelling. Investigating cell mechanics with atomic force microscopy. *Journal of The Royal Society Interface*, 12(104):20140970, 2015.

[15] Pei-Hsun Wu, Dikla Raz-Ben Aroush, Atef Asnacios, Wei-Chiang Chen, Maxim E. Dokukin, Bryant L. Doss, Pauline Durand-Smet, Andrew Ekpenyong, Jochen Guck, Nataliia V. Guz, Paul A. Janmey, Jerry S. H. Lee, Nicole M. Moore, Albrecht Ott, Yeh-Chuin Poh, Robert Ros, Mathias Sander, Igor Sokolov, Jack R. Staunton, Ning Wang, Graeme Whyte, and Denis Wirtz. A comparison of methods to assess cell mechanical properties. *Nature Methods*, 15(7):491–498, 2018.

[16] Di Chang, Takahiro Hirate, Chihiro Uehara, Hisataka Maruyama, Nobuyuki Uozumi, and Fumihito Arai. Evaluating young's modulus of single yeast cells based on compression using an atomic force microscope with a flat tip. *Microscopy and Microanalysis*, 27(2):392–399, 2021.

[17] Michael Krieg, Gotthold Fläschner, David Alsteens, Benjamin M. Gaub, Wouter H. Roos, Gijs J. L. Wuite, Hermann E. Gaub, Christoph Gerber, Yves F. Dufrêne, and Daniel J. Müller. Atomic force microscopy-based mechanobiology. *Nature Reviews Physics*, 1(1):41–57, 2019.

[18] Jason I. Kilpatrick, Irène Revenko, and Brian J. Rodriguez. Nanomechanics of cells and biomaterials studied by atomic force microscopy. *Advanced Healthcare Materials*, 4(16):2456–2474, 2015.

[19] Núria Gavara. A beginner's guide to atomic force microscopy probing for cell mechanics. *Microscopy Research and Technique*, 80(1):75–84, 2017.

[20] Hu Zhang and Kuo-Kang Liu. Optical tweezers for single cells. *Journal of The Royal Society Interface*, 5(24):671–690, 2008.

[21] C. Arbore, L. Perego, M. Sergides, and M. Capitanio. Probing force in living cells with optical tweezers: from single-molecule mechanics to cell mechanotransduction. *Biophys Rev*, 11(5):765–782, 2019.

[22] J. Guck, R. Ananthakrishnan, H. Mahmood, T. J. Moon, C. C. Cunningham, and J. Käs. The optical stretcher: A novel laser tool to micromanipulate cells. *Biophys. J.*, 81(2):767, 2001.

[23] Y. Jun, S. K. Tripathy, B. R. Narayanareddy, M. K. Mattson-Hoss, and S. P. Gross. Calibration of optical tweezers for in vivo force measurements: how do different approaches compare? *Biophys J*, 107(6):1474–84, 2014.

[24] T. Yang, F. Bragheri, and P. Minzioni. A comprehensive review of optical stretcher for cell mechanical characterization at single-cell level. *Micromachines (Basel)*, 7(5), 2016.

[25] F. Català-Castro, E. Schäffer, and M. Krieg. Exploring cell and tissue mechanics with optical tweezers. *J Cell Sci*, 135(15), 2022.

[26] R. M. Hochmuth. Micropipette aspiration of living cells. *J. Biomech.*, 33(1):15, 2000.

[27] Ehsan Shojaei-Baghini, Yi Zheng, and Yu Sun. Automated micropipette aspiration of single cells. *Annals of Biomedical Engineering*, 41(6):1208–1216, 2013.

[28] Erin A. Henslee. Review: Dielectrophoresis in cell characterization. *ELECTROPHORESIS*, 41(21-22):1915–1930, 2020.

[29] Rodrigo Martinez-Duarte. A critical review on the fabrication techniques that can enable higher throughput in dielectrophoresis devices. *ELECTROPHORESIS*, 43(1-2):232–248, 2022.

[30] H. Zhang, H. Chang, and P. Neuzil. Dep-on-a-chip: Dielectrophoresis applied to microfluidic platforms. *Micromachines (Basel)*, 10(6), 2019.

[31] Renny E. Fernandez, Ali Rohani, Vahid Farmehini, and Nathan S. Swami. Review: Microbial analysis in dielectrophoretic microfluidic systems. *Analytica chimica acta*, 966:11–33, 2017.

[32] Cheng Qian, Haibo Huang, Liguo Chen, Xiangpeng Li, Zunbiao Ge, Tao Chen, Zhan Yang, and Lining Sun. Dielectrophoresis for bioparticle manipulation. *International Journal of Molecular Sciences*, 15(10):18281–18309, 2014.

[33] Zachary R. Gagnon, Blanca H. Lapizco-Encinas, and Frantisek Foret. Cellular dielectrophoresis: Applications to the characterization, manipulation, separation and patterning of cells. *Electrophoresis*, 32:2466–2487, 2011.

[34] Yao Teng, Kui Zhu, Chunyang Xiong, and Jianyong Huang. Electrodeformation-based biomechanical chip for quantifying global viscoelasticity of cancer cells regulated by cell cycle. *Analytical Chemistry*, 90(14):8370–8378, 2018.

[35] Guohua Bai, Ying Li, Henry K. Chu, Kaiqun Wang, Qiulin Tan, Jijun Xiong, and Dong Sun. Characterization of biomechanical properties of cells through dielectrophoresis-based cell stretching and actin cytoskeleton modeling. *Biomedical engineering online*, 16(1):41–41, 2017.

[36] Gerrit Sitters, Douwe Kamsma, Gregor Thalhammer, Monika Ritsch-Marte, Erwin J. G. Peterman, and Gijs J. L. Wuite. Acoustic force spectroscopy. *Nature Methods*, 12(1):47–50, 2015.

[37] Douwe Kamsma, Ramon Creyghton, Gerrit Sitters, Gijs J. L. Wuite, and Erwin J. G. Peterman. Tuning the music: Acoustic force spectroscopy (afs) 2.0. *Methods*, 105:26–33, 2016.

[38] R. Sorkin, G. Bergamaschi, D. Kamsma, G. Brand, E. Dekel, Y. Ofir-Birin, A. Rudik, M. Gironella, F. Ritort, N. Regev-Rudzki, W. H. Roos, and G. J. L. Wuite. Probing cellular mechanics with acoustic force spectroscopy. *Mol Biol Cell*, 29(16):2005–2011, 2018.

[39] Valentin Romanov, Giulia Silvani, Huiyu Zhu, Charles D. Cox, and Boris Martinac. An acoustic platform for single-cell, high-throughput measurements of the viscoelastic properties of cells. *Small*, 17(3):2005759, 2021.

[40] Hyun-Kyu Choi, Hyun Gyu Kim, Min Ju Shon, and Tae-Young Yoon. High-resolution single-molecule magnetic tweezers. *Annual Review of Biochemistry*, 91(1):33–59, 2022.

[41] Rupa Sarkar and Valentin V. Rybenkov. A guide to magnetic tweezers and their applications. *Frontiers in Physics*, 4, 2016.

[42] Christian Aermes, Alexander Hayn, Tony Fischer, and Claudia Tanja Mierke. Environmentally controlled magnetic nano-tweezer for living cells and extracellular matrices. *Scientific Reports*, 10(1):13453, 2020.

[43] X. Tang, X. Liu, P. Li, D. Liu, M. Kojima, Q. Huang, and T. Arai. Efficient single-cell mechanical measurement by integrating a cell arraying microfluidic device with magnetic tweezer. *IEEE Robotics and Automation Letters*, 6(2):2978–2984, 2021.

[44] S. Warnat, H. King, C. Forbrigger, and T. Hubbard. Polymumps mems device to measure mechanical stiffness of single cells in aqueous media. *Journal of Micromechanics and Microengineering*, 25(2), 2015.

[45] B. Barazani, S. Warnat, A. Fine, and T. Hubbard. Mems squeezer for the measurement of single cell rupture force, stiffness change, and hysteresis. *Journal of Micromechanics and Microengineering*, 27(2), 2017.

[46] Bruno Barazani, Stephan Warnat, Ted Hubbard, and Andrew J. MacIntosh. Mechanical characterization of individual brewing yeast cells using microelectromechanical systems (mems): Cell rupture force and stiffness. *Journal of the American Society of Brewing Chemists*, 75(3):236–243, 2018.

[47] Yuki Takayama, Grégoire Perret, Momoko Kumemura, Manabu Ataka, Samuel Meignan, Stanislav L. Karsten, Hiroyuki Fujita, Dominique Collard, Chann Lagadec, and Mehmet Cagatay Tarhan. Developing a mems device with built-in microfluidics for biophysical single cell characterization. *Micromachines*, 9(6):275, 2018.

[48] Lap Man Lee and Allen P. Liu. The application of micropipette aspiration in molecular mechanics of single cells. *Journal of Nanotechnology in Engineering and Medicine*, 5(4), 2014.

[49] Jian Chen, Yi Zheng, Qingyuan Tan, Yan Liang Zhang, Jason Li, William R. Geddie, Michael A. S. Jewett, and Yu Sun. A microfluidic device for simultaneous electrical and mechanical measurements on single cells. *Biomicrofluidics*, 5(1), 2011.

[50] D. P. Theret, M. J. Levesque, M. Sato, R. M. Nerem, and L. T. Wheeler. The application of a homogeneous half-space model in the analysis of endothelial cell micropipette measurements. *J Biomech Eng*, 110(3):190–9, 1988.

[51] Quan Guo, Sunyoung Park, and Hongshen Ma. Microfluidic micropipette aspiration for measuring the deformability of single cells. *Lab on a Chip*, 12(15):2687–2695, 2012.

[52] Lap Man Lee and Allen P. Liu. A microfluidic pipette array for mechanophenotyping of cancer cells and mechanical gating of mechanosensitive channels. *Lab on a Chip*, 15(1):264–273, 2015.

[53] Lap Man Lee, Jin Woo Lee, Danielle Chase, Daniel Gebrezgiabhier, and Allen P. Liu. Development of an advanced microfluidic micropipette aspiration device for single cell mechanics studies. *Biomicrofluidics*, 10(5), 2016.

[54] Patricia M. Davidson, Gregory R. Fedorchak, Solenne Mondésert-Deveraux, Emily S. Bell, Philipp Isermann, Denis Aubry, Rachele Allena, and Jan Lammerding. High-throughput microfluidic micropipette aspiration device to probe time-scale dependent nuclear mechanics in intact cells. *Lab on a Chip*, 19(21):3652–3663, 2019.

[55] Ruben C. Boot, Alessio Roscani, Lennard van Buren, Samadarshi Maity, Gijsje H. Koenderink, and Pouyan E. Boukany. High-throughput mechanophenotyping of multicellular spheroids using a microfluidic micropipette aspiration chip. *Lab on a Chip*, 23(7):1768–1778, 2023.

[56] Chengcheng Xue, Junbo Wang, Yang Zhao, Deyong Chen, Wentao Yue, and Jian Chen. Constriction channel based single-cell mechanical property characterization. *Micromachines*, 6(11), 2015.

[57] Hanxu Chen, Jiahui Guo, Feika Bian, and Yuanjin Zhao. Microfluidic technologies for cell deformability cytometry. *Smart Medicine*, 1(1):e20220001, 2022.

[58] Marta Urbanska, Hector E. Muñoz, Josephine Shaw Bagnall, Oliver Otto, Scott R. Manalis, Dino Di Carlo, and Jochen Guck. A comparison of microfluidic methods for high-throughput cell deformability measurements. *Nature Methods*, 17(6):587–593, 2020.

[59] H. W. Hou, Q. S. Li, G. Y. Lee, A. P. Kumar, C. N. Ong, and C. T. Lim. Deformability study of breast cancer cells using microfluidics. *Biomed. Microdevices*, 11(3):557, 2009.

[60] S. Byun, S. Son, D. Amodei, N. Cermak, J. Shaw, J. H. Kang, V. C. Hecht, M. M. Winslow, T. Jacks, P. Mallick, and S. R. Manalis. Characterizing deformability and surface friction of cancer cells. *Proc. Natl. Acad. Sci.*, 110(19):7580, 2013.

[61] Z. S. Khan and S. A. Vanapalli. Probing the mechanical properties of brain cancer cells using a microfluidic cell squeezer device. *Biomicrofluidics*, 7(1), 2013.

[62] Y. N. Luo, D. Y. Chen, Y. Zhao, C. Wei, X. T. Zhao, W. T. Yue, R. Long, J. B. Wang, and J. Chen. A constriction channel based microfluidic system enabling continuous characterization of cellular instantaneous young's modulus. *Sensors and Actuators B: Chemical*, 202:1183–1189, 2014.

[63] Janina R Lange, Julian Steinwachs, Thorsten Kolb, Lena A Lautscham, Irina Harder, Graeme Whyte, and Ben Fabry. Microconstriction arrays for high-throughput quantitative measurements of cell mechanical properties. *Biophysical Journal*, 109(1):26–34, 2015.

[64] Kendra D. Nyberg, Kenneth H. Hu, Sara H. Kleinman, Damir B. Khismatullin, Manish J. Butte, and Amy C. Rowat. Quantitative deformability cytometry: Rapid, calibrated measurements of cell mechanical properties. *Biophysical Journal*, 113(7):1574–1584, 2017.

[65] Kendra D. Nyberg, Samuel L. Bruce, Angelyn V. Nguyen, Clara K. Chan, Navjot K. Gill, Tae-Hyung Kim, Erica K. Sloan, and Amy C. Rowat. Predicting cancer cell invasion by single-cell physical phenotyping. *Integrative Biology*, 10(4):218–231, 2018.

[66] Zhenlin Chen, Yonggang Zhu, Dong Xu, Md Mahbub Alam, Lingling Shui, and Huaying Chen. Cell elasticity measurement using a microfluidic device with real-time pressure feedback. *Lab on a Chip*, 20(13):2343–2353, 2020.

[67] Zhenlin Chen, Tsz Fung Yip, Yonggang Zhu, Joshua W. K. Ho, and Huaying Chen. The method to quantify cell elasticity based on the precise measurement of pressure inducing cell deformation in microfluidic channels. *MethodsX*, 8:101247–101247, 2021.

[68] A. Mietke, O. Otto, S. Girardo, P. Rosendahl, A. Taubenberger, S. Golfier, E. Ulbricht, S. Aland, J. Guck, and E. Fischer-Friedrich. Extracting cell stiffness from real-time deformability cytometry: Theory and experiment. *Biophys J*, 109(10):2023–36, 2015.

[69] M. Mokbel, D. Mokbel, A. Mietke, N. Träber, S. Girardo, O. Otto, J. Guck, and S. Aland. Numerical simulation of real-time deformability cytometry to extract cell mechanical properties. *ACS Biomaterials Science and Engineering*, 3(11):2962–2973, 2017.

[70] O. Otto, P. Rosendahl, A. Mietke, S. Golfier, C. Herold, D. Klaue, S. Girardo, S. Pagliara, A. Ekpenyong, A. Jacobi, M. Wobus, N. Topfner, U. F. Keyser, J. Mansfeld, E. Fischer-Friedrich, and J. Guck. Real-time deformability cytometry: on-the-fly cell mechanical phenotyping. *Nature Methods*, 12(3):199–202, 4 p following 202, 2015.

[71] Stefan Golfier, Philipp Rosendahl, Alexander Mietke, Maik Herbig, Jochen Guck, and Oliver Otto. High-throughput cell mechanical phenotyping for label-free titration assays of cytoskeletal modifications. *Cytoskeleton*, 74(8):283–296, 2017.

[72] Shamim M. Ahmmed, Swastika S. Bithi, Adity A. Pore, Noshin Mubtasim, Caroline Schuster, Lauren S. Gollahon, and Siva A. Vanapalli. Multi-sample deformability cytometry of cancer cells. *APL Bioengineering*, 2(3):032002, 2018.

[73] M. Herbig, A. Mietke, P. Müller, and O. Otto. Statistics for real-time deformability cytometry: Clustering, dimensionality reduction, and significance testing. *Biomicrofluidics*, 12(4):042214, 2018.

[74] Bob Fregin, Fabian Czerwinski, Doreen Biedenweg, Salvatore Girardo, Stefan Gross, Konstanze Aurich, and Oliver Otto. High-throughput single-cell rheology in complex samples by dynamic real-time deformability cytometry. *Nature Communications*, 10(1):415, 2019.

[75] Maik Herbig, Angela Jacobi, Manja Wobus, Heike Weidner, Anna Mies, Martin Kräter, Oliver Otto, Christian Thiede, Marie-Theresa Weickert, Katharina S. Götze, Martina Rauner, Lorenz C. Hofbauer, Martin Bornhäuser, Jochen Guck, Marius Ader, Uwe Platzbecker, and Ekaterina Balaian. Machine learning assisted real-time deformability cytometry of cd34+ cells allows to identify patients with myelodysplastic syndromes. *Scientific Reports*, 12(1):870, 2022.

[76] Hector E. Muñoz, Jonathan Lin, Bonnie G. Yeh, Tridib Biswas, and Dino Di Carlo. Fluorescence imaging deformability cytometry: integrating nuclear structure with mechanical phenotyping. *Med-X*, 1(1):10, 2023.

[77] Daniel R. Gossett, Henry T. K. Tse, Serena A. Lee, Yong Ying, Anne G. Lindgren, Otto O. Yang, Jianyu Rao, Amander T. Clark, and Dino Di Carlo. Hydrodynamic stretching of single cells for large population mechanical phenotyping. *Proceedings of the National Academy of Sciences*, 109(20):7630, 2012.

[78] J. Lin, D. Kim, H. T. Tse, P. Tseng, L. Peng, M. Dhar, S. Karumbayaram, and D. Di Carlo. High-throughput physical phenotyping of cell differentiation. *Microsyst. Nanoeng.*, 3:17013, 2017.

[79] Mahdokht Masaeli, Dewal Gupta, Sean O'Byrne, Henry T. K. Tse, Daniel R. Gossett, Peter Tseng, Andrew S. Utada, Hea-Jin Jung, Stephen Young, Amander T. Clark, and Dino Di Carlo. Multiparameter mechanical and morphometric screening of cells. *Scientific Reports*, 6(1):37863, 2016.

[80] Fern J. Armistead, Julia Gala De Pablo, Hermes Gadêlha, Sally A. Peyman, and Stephen D. Evans. Cells under stress: An inertial-shear microfluidic determination of cell behavior. *Biophysical Journal*, 116(6):1127–1135, 2019.

[81] L. Guillou, J. B. Dahl, J. G. Lin, A. I. Barakat, J. Husson, S. J. Muller, and S. Kumar. Measuring cell viscoelastic properties using a microfluidic extensional flow device. *Biophys J*, 111(9):2039–2050, 2016.

[82] R. Reale, A. De Ninno, T. Nepi, P. Bisegna, and F. Caselli. Extensional-flow impedance cytometer for contactless and optics-free erythrocyte deformability analysis. *IEEE Trans Biomed Eng*, 70(2):565–572, 2023.

[83] Anthony K. Au, Nirveek Bhattacharjee, Lisa F. Horowitz, Tim C. Chang, and Albert Folch. 3d-printed microfluidic automation. *Lab Chip*, 15(8):1934–1941, 2015.

[84] Narayan Sundararajan, Dongshin Kim, and Andrew A. Berlin. Microfluidic operations using deformable polymer membranes fabricated by single layer soft lithography. *Lab on a Chip*, 5(3):350–354, 2005.

[85] Christian Westendorf, Albert J. Bae, Christoph Erlenkamper, Edouard Galland, Carl Franck, Eberhard Bodenschatz, and Carsten Beta. Live cell flattening - traditional and novel approaches. *PMC biophysics*, 3(1):9–9, 2010.

[86] Guansheng Du, Agnese Ravetto, Qun Fang, and Jaap M. J. den Toonder. Cell types can be distinguished by measuring their viscoelastic recovery times using a micro-fluidic device. *Biomedical Microdevices*, 13(1):29–40, 2011.

[87] Tairo Yokokura, Yuta Nakashima, Yukihiro Yonemoto, Yuki Hikichi, and Yoshitaka Nakanishi. Method for measuring young's modulus of cells using a cell compression microdevice. *International Journal of Engineering Science*, 114:41–48, 2017.

[88] Kenneth K. Y. Ho, Lap Man Lee, and Allen P. Liu. Mechanically activated artificial cell by using microfluidics. *Scientific Reports*, 6(1):32912, 2016.

[89] Tom Robinson and Petra S. Dittrich. Observations of membrane domain reorganization in mechanically compressed artificial cells. *ChemBioChem*, 20(20):2666–2673, 2019.

[90] Ardon Z. Shorr, Utku M. Sönmez, Jonathan S. Minden, and Philip R. LeDuc. High-throughput mechanotransduction in drosophila embryos with mesofluidics. *Lab on a Chip*, 19(7):1141–1152, 2019.

[91] Sevgi Onal, Maan M. Alkaisi, and Volker Nock. A flexible microdevice for mechanical cell stimulation and compression in microfluidic settings. *Frontiers in Physics*, 9, 2021.

[92] Onal Sevgi, M. Alkaisi Maan, and Nock Volker. Application of sequential cyclic compression on cancer cells in a flexible microdevice. *bioRxiv*, page 2022.01.07.475458, 2022.

[93] Yu Chang Kim, Joo H. Kang, Sang-Jin Park, Eui-Soo Yoon, and Je-Kyun Park. Microfluidic biomechanical device for compressive cell stimulation and lysis. *Sensors and Actuators B: Chemical*, 128(1):108–116, 2007.

[94] Hsin-Yi Hsieh, Gulden Camci-Unal, Tsu-Wei Huang, Ronglih Liao, Tsung-Ju Chen, Arghya Paul, Fan-Gang Tseng, and Ali Khademhosseini. Gradient static-strain stimulation in a microfluidic chip for 3d cellular alignment. *Lab on a Chip*, 14(3):482–493, 2014.

[95] Donghee Lee, Alek Erickson, Taesun You, Andrew T. Dudley, and Sangjin Ryu. Pneumatic microfluidic cell compression device for high-throughput study of chondrocyte mechanobiology. *Lab on a Chip*, 18(14):2077–2086, 2018.

[96] Jungho Ahn, Hyeok Lee, Habin Kang, Hyeri Choi, Kyungmin Son, James Yu, Jungseub Lee, Jungeun Lim, Dohyun Park, Maenghyo Cho, and Noo Li Jeon. Pneumatically actuated microfluidic platform for reconstituting 3d vascular tissue compression. *Applied Sciences*, 10(6):2027, 2020.

[97] Carlo Alberto Paggi, Bastien Venzac, Marcel Karperien, Jeroen C. H. Leijten, and Séverine Le Gac. Monolithic microfluidic platform for exerting gradients of compression on cell-laden hydrogels, and application to a model of the articular cartilage. *Sensors and Actuators B: Chemical*, 315:127917, 2020.

[98] A.M. Fine. Sample processing for microscopy, U.S. Patent 10,317,662, Jun. 11, 2019.

[99] A.M. Fine. Sample processing for microscopy, U.S. Patent 10,606,059, Mar. 31, 2020.

[100] A.M. Fine. Sample processing for microscopy, U.S. Patent 11,112,593, Sep. 7, 2021.

[101] S. M. Scott and Z. Ali. Fabrication methods for microfluidic devices: An overview. *Micromachines (Basel)*, 12(3), 2021.

[102] C. B. Carballo, Y. Nakagawa, I. Sekiya, and S. A. Rodeo. Basic science of articular cartilage. *Clin Sports Med*, 36(3):413–425, 2017.

[103] H. Muir. The chondrocyte, architect of cartilage. biomechanics, structure, function and molecular biology of cartilage matrix macromolecules. *Bioessays*, 17(12):1039–48, 1995.

[104] Bac V. Nguyen, Qi Guang Wang, Nicola J. Kuiper, Alicia J. El Haj, Colin R. Thomas, and Zhibing Zhang. Biomechanical properties of single chondrocytes and chondrons determined by micromanipulation and finite-element modelling. *Journal of The Royal Society Interface*, 7(53):1723–1733, 2010.

[105] J. A. Martin and J. A. Buckwalter. Aging, articular cartilage chondrocyte senescence and osteoarthritis. *Biogerontology*, 3(5):257–64, 2002.

[106] Kamil E. Barbour, Louise B. Murphy, Charles G. Helmick, Jennifer M. Hootman, Jordan B. Renner, and Joanne M. Jordan. Bone mineral density and the risk of hip and knee osteoarthritis: The johnston county osteoarthritis project. *Arthritis Care and Research*, 69(12):1863–1870, 2017.

[107] Duncan K. Temple, Anna A. Cederlund, Bernard M. Lawless, Richard M. Aspden, and Daniel M. Espino. Viscoelastic properties of human and bovine articular cartilage: a comparison of frequency-dependent trends. *BMC Musculoskeletal Disorders*, 17(1):419, 2016.

[108] P. P. Brahmachary, H. D. Welhaven, and R. K. June. Metabolomic profiling to understand chondrocyte metabolism. *Methods Mol Biol*, 2598:141–156, 2023.

[109] R. Saraswat, I. Ratnayake, E. C. Perez, W. M. Schutz, Z. Zhu, S. P. Ahrenkiel, and S. T. Wood. Micropatterned biphasic nanocomposite platform for maintaining chondrocyte morphology. *ACS Appl Mater Interfaces*, 12(13):14814–14824, 2020.

[110] L. G. Alexopoulos, M. A. Haider, T. P. Vail, and F. Guilak. Alterations in the mechanical properties of the human chondrocyte pericellular matrix with osteoarthritis. *J Biomech Eng*, 125(3):323–33, 2003.

[111] E. M. Darling, R. E. Wilusz, M. P. Bolognesi, S. Zauscher, and F. Guilak. Spatial mapping of the biomechanical properties of the pericellular matrix of articular cartilage measured in situ via atomic force microscopy. *Biophys J*, 98(12):2848–56, 2010.

[112] Wendy R. Trickey, Greta M. Lee, and Farshid Guilak. Viscoelastic properties of chondrocytes from normal and osteoarthritic human cartilage. *Journal of Orthopaedic Research*, 18(6):891–898, 2000.

[113] Wendy R. Trickey, Frank P. T. Baaijens, Tod A. Laursen, Leonidas G. Alexopoulos, and Farshid Guilak. Determination of the poisson's ratio of the cell: recovery properties of chondrocytes after release from complete micropipette aspiration. *Journal of Biomechanics*, 39(1):78–87, 2006.

[114] Nikolai Steklov, Ajay Srivastava, K. L. P. Sung, Peter C. Chen, Martin K. Lotz, and Darryl D. D'Lima. Aging-related differences in chondrocyte viscoelastic properties. *Molecular and cellular biomechanics : MCB*, 6(2):113–119, 2009.

[115] G. D. Nicodemus and S. J. Bryant. Mechanical loading regimes affect the anabolic and catabolic activities by chondrocytes encapsulated in peg hydrogels. *Osteoarthritis and Cartilage*, 18(1):126–137, 2010.

[116] P. Brahmachary, E. Erdogan, E. Myers, and R. K. June. Metabolomic profiling and characterization of a novel 3d culture system for studying chondrocyte mechanotransduction. *bioRxiv*, 2024.

[117] F. R. Niu, D. C. Wang, J. P. Lu, W. Wu, and X. D. Wang. Potentials of single-cell biology in identification and validation of disease biomarkers. *Journal of Cellular and Molecular Medicine*, 20(9):1789–1795, 2016.

[118] M. Lekka, K. Pogoda, J. Gostek, O. Klymenko, S. Prauzner-Bechcicki, J. Wiltowska-Zuber, J. Jaczewska, J. Lekki, and Z. Stachura. Cancer cell recognition - mechanical phenotype. *Micron*, 43(12):1259–1266, 2012.

[119] Xiaole Mao and Tony Jun Huang. Exploiting mechanical biomarkers in microfluidics. *Lab on a chip*, 12(20):4006–4009, 2012.

[120] Subra Suresh. Biomechanics and biophysics of cancer cells. *Acta Biomaterialia*, 3(4):413–438, 2007.

[121] Chengpeng Chen, Benjamin T. Mehl, Akash S. Munshi, Alexandra D. Townsend, Dana M. Spence, and R. Scott Martin. 3d-printed microfluidic devices: fabrication, advantages and limitationsa mini review. *Anal. Methods*, 8(31):6005–6012, 2016.

[122] Niall P. Macdonald, Joan M. Cabot, Petr Smejkal, Rosanne M. Guijt, Brett Paull, and Michael C. Breadmore. Comparing microfluidic performance of three-dimensional (3d) printing platforms. *Analytical chemistry*, 89(7):3858, 2017.

[123] Yf Zhou. The recent development and applications of fluidic channels by 3d printing. *J. Biomed. Sci.*, 24(1), 2017.

[124] Eric Lepowsky and Savas Tasoglu. Emerging anti-fouling methods: Towards reusability of 3d-printed devices for biomedical applications. *Micromachines*, 9(4):196, 2018.

[125] Shengli Mi, Zhichang Du, Yuanyuan Xu, and Wei Sun. The crossing and integration between microfluidic technology and 3d printing for organ-on-chips. *Journal of Materials Chemistry B*, 6(39):6191–6206, 2018.

[126] Ryan D. Sochol, Eric Sweet, Casey C. Glick, Sung-Yueh Wu, Chen Yang, Michael Restaino, and Liwei Lin. 3d printed microfluidics and microelectronics. *Microelectronic Engineering*, 189:52–68, 2018.

[127] Jia Min Lee, Swee Leong Sing, Miaomiao Zhou, and Wai Yee Yeong. 3d bioprinting processes: A perspective on classification and terminology. *International Journal of Bioprinting*, 4, 2018.

[128] Nirveek Bhattacharjee, Arturo Urrios, Shawn Kang, and Albert Folch. The upcoming 3d-printing revolution in microfluidics. *Lab on a chip*, 16(10):1720–1742, 2016.

[129] Hua Gong, Michael Beauchamp, Steven Perry, Adam T. Woolley, and Gregory P. Nordin. Optical approach to resin formulation for 3d printed microfluidics. *RSC Adv.*, 5(129):106621–106632, 2015.

[130] Valentin Romanov, Raheel Samuel, Marzieh Chaharlang, Alexander R. Jafek, Adam Frost, and Bruce K. Gale. Fdm 3d printing of high-pressure, heat-resistant, transparent microfluidic devices. *Analytical Chemistry*, 90(17):10450–10456, 2018.

[131] Arturo Urrios, Cesar Parra-Cabrera, Nirveek Bhattacharjee, Alan M. Gonzalez-Suarez, Luis G. Rigat-Brugarolas, Umashree Nallapatti, Josep Samitier, Cole A. Deforest, Francesc Posas, Jos L. Garcia-Cordero, and Albert Folch. 3d-printing of transparent bio-microfluidic devices in peg-da. *Lab Chip*, 16(12):2287–2294, 2016.

[132] Hua Gong, Adam T. Woolley, and Gregory P. Nordin. High density 3d printed microfluidic valves, pumps, and multiplexers. *Lab Chip*, 16(13):2450–2458, 2016.

[133] Hua Gong, Bryce P. Bickham, Adam T. Woolley, and Gregory P. Nordin. Custom 3d printer and resin for 18 um x 20 um microfluidic flow channels. *Lab on a Chip*, 17(17):2899–2909, 2017.

[134] Hua Gong, Adam T. Woolley, and Gregory P. Nordin. 3d printed high density, reversible, chip-to-chip microfluidic interconnects. *Lab on a Chip*, 18(4):639–647, 2018.

[135] Ellen K. Parker, Anna V. Nielsen, Michael J. Beauchamp, Haifa M. Almughamsi, Jacob B. Nielsen, Mukul Sonker, Hua Gong, Gregory P. Nordin, and Adam T. Woolley. 3d printed microfluidic devices with immunoaffinity monoliths for extraction of preterm birth biomarkers. *Analytical and Bioanalytical Chemistry*, 411(21):5405–5413, 2019.

[136] Yuan-Sheng Lee, Nirveek Bhattacharjee, and Albert Folch. 3d-printed quake-style microvalves and micropumps. *Lab on a Chip*, 18(8):1207–1214, 2018.

[137] Yong Tae Kim, Kurt Castro, Nirveek Bhattacharjee, and Albert Folch. Digital manufacturing of selective porous barriers in microchannels using multi-material stereolithography. *Micromachines*, 9(3):125, 2018.

[138] Yong Tae Kim, Sara Bohjanen, Nirveek Bhattacharjee, and Albert Folch. Partitioning of hydrogels in 3d-printed microchannels. *Lab on a Chip*, 2019.

[139] Michael J. Beauchamp, Hua Gong, Adam T. Woolley, and Gregory P. Nordin. 3d printed microfluidic features using dose control in x, y, and z dimensions. *Micromachines*, 9(7):326, 2018.

[140] Michael J. Beauchamp, Anna V. Nielsen, Hua Gong, Gregory P. Nordin, and Adam T. Woolley. 3d printed microfluidic devices for microchip electrophoresis of preterm birth biomarkers. *Analytical Chemistry*, 91(11):7418–7425, 2019.

[141] Chad I. Rogers, Kamran Qaderi, Adam T. Woolley, and Gregory P. Nordin. 3d printed microfluidic devices with integrated valves. *Biomicrofluidics*, 9(1):016501–016501, 2015.

[142] Kimberly Plevniak, Matthew Campbell, Timothy Myers, Abby Hodges, and Mei He. 3d printed auto-mixing chip enables rapid smartphone diagnosis of anemia. *Biomicrofluidics*, 10(5):054113–054113, 2016.

[143] Alexandra P. Kuo, Nirveek Bhattacharjee, Yuan-Sheng Lee, Kurt Castro, Yong Tae Kim, and Albert Folch. High-precision stereolithography of biomicrofluidic devices. *Advanced Materials Technologies*, 4(6):1800395, 2019.

[144] Feng Li, Niall P. Macdonald, Rosanne M. Guijt, and Michael C. Breadmore. Increasing the functionalities of 3d printed microchemical devices by single material, multimaterial, and print-pause-print 3d printing. *Lab on a Chip*, 19(1):35–49, 2019.

[145] Muinul Banna, Kaustav Bera, Ryan Sochol, Liwei Lin, Homayoun Najjaran, Rehan Sadiq, and Mina Hoorfar. 3d printing-based integrated water quality sensing system. *Sensors (Basel, Switzerland)*, 17(6):1336, 2017.

[146] Gabriel Gaal, Melissa Mendes, Tiago P. de Almeida, Maria H. O. Piazzetta, Ângelo L. Gobbi, Antonio Riul, and Varlei Rodrigues. Simplified fabrication of integrated microfluidic devices using fused deposition modeling 3d printing. *Sensors and Actuators B: Chemical*, 242:35–40, 2017.

[147] Roberto Pol, Francisco Céspedes, David Gabriel, and Mireia Baeza. Fully integrated screen-printed sulfide-selective sensor on a 3d-printed potentiometric microfluidic platform. *Sensors and Actuators B: Chemical*, 290:364–370, 2019.

[148] Nicolò Giuseppe Di Novo, Edoardo Cantù, Sarah Tonello, Emilio Sardini, and Mauro Serpelloni. Support-material-free microfluidics on an electrochemical sensors platform by aerosol jet printing. *Sensors (Basel, Switzerland)*, 19(8):1842, 2019.

[149] Aaron D. Benjamin, Reha Abbasi, Madison Owens, Robert J. Olsen, Danica J. Walsh, Thomas B. LeFevre, and James N. Wilking. Light-based 3d printing of hydrogels with high-resolution channels. *Biomedical Physics & Engineering Express*, 5(2):025035, 2019.

[150] J. Atencia, G. A. Cooksey, A. Jahn, J. M. Zook, W. N. Vreeland, and L. E. Locascio. Magnetic connectors for microfluidic applications. *Lab Chip*, 10(2):246–9, 2010.

[151] Liju Yang. Electrical impedance spectroscopy for detection of bacterial cells in suspensions using interdigitated microelectrodes. *Talanta*, 74(5):1621–1629, 2008.

[152] E. Hecht. *Optics*. Pearson Education, Incorporated, 2017.

[153] Bruce Alberts, Alexander Johnson, Julian Lewis, Martin Raff, Keith Roberts, and Peter Walter. *Molecular Biology of the Cell*. Garland Science, New York, 5th edition, 2007.

[154] Xingpeng Di, Xiaoshuai Gao, Liao Peng, Jianzhong Ai, Xi Jin, Shiqian Qi, Hong Li, Kunjie Wang, and Deyi Luo. Cellular mechanotransduction in health and diseases: from molecular mechanism to therapeutic targets. *Signal Transduction and Targeted Therapy*, 8(1):282, 2023.

[155] N. Wang. Review of cellular mechanotransduction. *J Phys D Appl Phys*, 50(23), 2017.

[156] Elisabetta Canetta, Alain Duperray, Anne Leyrat, and Claude Verdier. Measuring cell viscoelastic properties using a force-spectrometer: influence of protein-cytoplasm interactions. *Biorheology*, 42(5):321–333, 2005.

[157] Ya Hua Chim, Louise M. Mason, Nicola Rath, Michael F. Olson, Manlio Tassieri, and Huabing Yin. A one-step procedure to probe the viscoelastic properties of cells by atomic force microscopy. *Scientific Reports*, 8(1):14462, 2018.

[158] Yuri M. Efremov, Wen-Horng Wang, Shana D. Hardy, Robert L. Geahlen, and Arvind Raman. Measuring nanoscale viscoelastic parameters of cells directly from afm force-displacement curves. *Scientific Reports*, 7(1):1541, 2017.

[159] M. Lekka. Discrimination between normal and cancerous cells using afm. *Bionanoscience*, 6:65, 2016.

[160] Torsten W. Remmerbach, Falk Wottawah, Julia Dietrich, Bryan Lincoln, Christian Wittekind, and Jochen Guck. Oral cancer diagnosis by mechanical phenotyping. *Cancer Research*, 69(5):1728, 2009.

[161] I. Sraj, C. D. Eggleton, R. Jimenez, E. Hoover, J. Squier, J. Chichester, and D. W. M. Marr. Cell deformation cytometry using diode-bar optical stretchers. *J. Biomed. Opt.*, 15(4):047010, 2010.

[162] Yongsheng Li, Yueqin Li, Quanyou Zhang, Lili Wang, Meiqing Guo, Xiaogang Wu, Yuan Guo, Jing Chen, and Weiyi Chen. Mechanical properties of chondrocytes estimated from different models of micropipette aspiration. *Biophysical Journal*, 116(11):2181–2194, 2019.

[163] Nathalie Bufi, Pauline Durand-Smet, and Atef Asnacios. *Chapter 11 - Single-cell mechanics: The parallel plates technique*, volume 125, pages 187–209. Academic Press, 2015.

[164] B. P. Chan, C. H. Li, K. L. Au-Yeung, K. Y. Sze, and A. H. Ngan. A microplate compression method for elastic modulus measurement of soft and viscoelastic collagen microspheres. *Ann Biomed Eng*, 36(7):1254–67, 2008.

[165] O. Thoumine and A. Ott. Time scale dependent viscoelastic and contractile regimes in fibroblasts probed by microplate manipulation. *J Cell Sci*, 110 (Pt 17):2109–16, 1997.

[166] M. Neubauer, M. McGlennen, S. Thomas, and S. Warnat. 3d printing on glass for direct sensor integration. *Engineering Research Express*, 1(2):025051, 2019.

[167] W. N. Findley, J. S. Lai, K. Onaran, and R. M. Christensen. Creep and relaxation of nonlinear viscoelastic materials with an introduction to linear viscoelasticity. *Journal of Applied Mechanics*, 44(2):364–364, 1977.

[168] E. M. Darling, S. Zauscher, and F. Guilak. Viscoelastic properties of zonal articular chondrocytes measured by atomic force microscopy. *Osteoarthritis and Cartilage*, 14(6):571–579, 2006.

[169] W. Duan, L. Wei, J. Zhang, Y. Hao, C. Li, H. Li, Q. Li, Q. Zhang, W. Chen, and X. Wei. Alteration of viscoelastic properties is associated with a change in cytoskeleton components of ageing chondrocytes from rabbit knee articular cartilage. *Mol Cell Biomech*, 8(4):253–74, 2011.

[170] Farshid Guilak, Geoffrey R. Erickson, and H. Ping Ting-Beall. The effects of osmotic stress on the viscoelastic and physical properties of articular chondrocytes. *Biophysical Journal*, 82(2):720–727, 2002.

[171] W. R. Trickey, T. P. Vail, and F. Guilak. The role of the cytoskeleton in the viscoelastic properties of human articular chondrocytes. *J Orthop Res*, 22(1):131–9, 2004.

[172] Heiko Blaser, Michal Reichman-Fried, Irinka Castanon, Karin Dumstrei, Florence L Marlow, Koichi Kawakami, Lilianna Solnica-Krezel, Carl-Philipp Heisenberg, and Erez Raz. Migration of zebrafish primordial germ cells: A role for myosin contraction and cytoplasmic flow. *Developmental Cell*, 11(5):613–627, 2006.

[173] Ewa K. Paluch and Erez Raz. The role and regulation of blebs in cell migration. *Current Opinion in Cell Biology*, 25(5):582–590, 2013.

[174] Ewa Paluch, Cécile Sykes, Jacques Prost, and Michel Bornens. Dynamic modes of the cortical actomyosin gel during cell locomotion and division. *Trends in Cell Biology*, 16(1):5–10, 2006.

[175] Mathew L. Coleman, Erik A. Sahai, Margaret Yeo, Marta Bosch, Ann Dewar, and Michael F. Olson. Membrane blebbing during apoptosis results from caspase-mediated activation of rock i. *Nature Cell Biology*, 3(4):339–345, 2001.

[176] Jason C. Mills, Nicole L. Stone, Joseph Erhardt, and Randall N. Pittman. Apoptotic membrane blebbing is regulated by myosin light chain phosphorylation. *Journal of Cell Biology*, 140(3):627–636, 1998.

[177] Guillaume T. Charras, Margaret Coughlin, Timothy J. Mitchison, and L. Mahadevan. Life and times of a cellular bleb. *Biophysical Journal*, 94(5):1836–1853, 2008.

[178] Alessandro Di Cerbo, Valentina Rubino, Francesca Morelli, Giuseppina Ruggiero, Rosaria Landi, Gianandrea Guidetti, Sergio Canello, Giuseppe Terrazzano, and Andrea Alessandrini. Mechanical phenotyping of k562 cells by the micropipette aspiration

technique allows identifying mechanical changes induced by drugs. *Scientific Reports*, 8(1):1219, 2018.

[179] Priyanka Pravincumar, Dan L. Bader, and Martin M. Knight. Viscoelastic cell mechanics and actin remodelling are dependent on the rate of applied pressure. *PLOS ONE*, 7(9):e43938, 2012.

[180] Kristina Sliogeryte, Stephen D. Thorpe, David A. Lee, Lorenzo Botto, and Martin M. Knight. Stem cell differentiation increases membrane-actin adhesion regulating cell blebability, migration and mechanics. *Scientific Reports*, 4(1):7307, 2014.

[181] K. Sliogeryte, L. Botto, D. A. Lee, and M. M. Knight. Chondrocyte dedifferentiation increases cell stiffness by strengthening membrane-actin adhesion. *Osteoarthritis and Cartilage*, 24(5):912–920, 2016.

[182] Pouyan Keshavarz Motamed, Hesam Abouali, Mahla Poudineh, and Nima Maftoon. Experimental measurement and numerical modeling of deformation behavior of breast cancer cells passing through constricted microfluidic channels. *Microsystems and Nanoengineering*, 10(1):7, 2024.

[183] A. Cahn, L. Livshits, A. Srulevich, I. Raz, S. Yedgar, and G. Barshtein. Diabetic foot disease is associated with reduced erythrocyte deformability. *Int Wound J*, 13(4):500–4, 2016.

[184] Mario Gutierrez, Mark Shamoun, Katie Giger Seu, Tyler Tanski, Theodosia A. Kalfa, and Omolola Eniola-Adefeso. Characterizing bulk rigidity of rigid red blood cell populations in sickle-cell disease patients. *Scientific Reports*, 11(1):7909, 2021.

[185] C. H. Hsieh, Y. H. Lin, S. Lin, J. J. Tsai-Wu, C. H. Herbert Wu, and C. C. Jiang. Surface ultrastructure and mechanical property of human chondrocyte revealed by atomic force microscopy. *Osteoarthritis Cartilage*, 16(4):480–8, 2008.

[186] H. Long, Q. Liu, H. Yin, K. Wang, N. Diao, Y. Zhang, J. Lin, and A. Guo. Prevalence trends of site-specific osteoarthritis from 1990 to 2019: Findings from the global burden of disease study 2019. *Arthritis Rheumatol*, 74(7):1172–1183, 2022.

[187] D. J. Hunter and S. Bierma-Zeinstra. Osteoarthritis. *Lancet*, 393(10182):1745–1759, 2019.

[188] C. A. Poole. Articular cartilage chondrons: form, function and failure. *J Anat*, 191 (Pt 1)(Pt 1):1–13, 1997.

[189] Rebecca E. Wilusz, Johannah Sanchez-Adams, and Farshid Guilak. The structure and function of the pericellular matrix of articular cartilage. *Matrix Biology*, 39:25–32, 2014.

[190] Leonidas G. Alexopoulos, Lori A. Setton, and Farshid Guilak. The biomechanical role of the chondrocyte pericellular matrix in articular cartilage. *Acta Biomaterialia*, 1(3):317–325, 2005.

[191] Cheng Chen, Dhananjay T. Tambe, Linhong Deng, and Liu Yang. Biomechanical properties and mechanobiology of the articular chondrocyte. *American Journal of Physiology-Cell Physiology*, 305(12):C1202–C1208, 2013.

[192] J. Bonaventure, N. Kadhom, L. Cohen-Solal, K. H. Ng, J. Bourguignon, C. Lasselin, and P. Freisinger. Reexpression of cartilage-specific genes by dedifferentiated human articular chondrocytes cultured in alginate beads. *Experimental Cell Research*, 212(1):97–104, 1994.

[193] Christopher M. Larson, Scott S. Kelley, A. Denene Blackwood, Albert J. Banes, and Greta M. Lee. Retention of the native chondrocyte pericellular matrix results in significantly improved matrix production. *Matrix Biology*, 21(4):349–359, 2002.

[194] Lucienne A. Vonk, Behrouz Zandieh Doulabi, ChunLing Huang, Marco N. Helder, Vincent Everts, and Ruud A. Bank. Preservation of the chondrocyte's pericellular matrix improves cell-induced cartilage formation. *Journal of Cellular Biochemistry*, 110(1):260–271, 2010.

[195] M. Amr, A. Mallah, S. Yasmeen, B. Van Wie, A. Gozen, J. Mendenhall, and N. I. Abu-Lail. From chondrocytes to chondrons, maintenance of phenotype and matrix production in a composite 3d hydrogel scaffold. *Gels*, 8(2), 2022.

[196] J. E. Jeon, K. Schrobback, C. Meinert, V. Sramek, D. W. Hutmacher, and T. J. Klein. Effect of preculture and loading on expression of matrix molecules, matrix metalloproteinases, and cytokines by expanded osteoarthritic chondrocytes. *Arthritis Rheum*, 65(9):2356–67, 2013.

[197] L. Ng, H. H. Hung, A. Sprunt, S. Chubinskaya, C. Ortiz, and A. Grodzinsky. Nanomechanical properties of individual chondrocytes and their developing growth factor-stimulated pericellular matrix. *J Biomech*, 40(5):1011–23, 2007.

[198] M. J. Stoddart, L. Ettinger, and H. J. Häuselmann. Generation of a scaffold free cartilage-like implant from a small amount of starting material. *Journal of Cellular and Molecular Medicine*, 10(2):480–492, 2006.

[199] Hiroaki Kamishina, Takayoshi Miyabayashi, Roger M. Clemmons, James P. Farese, and Elizabeth W. Uhl. Three-dimensional culture of feline articular chondrocytes in alginate microspheres. *Journal of Veterinary Medical Science*, 68(11):1239–1242, 2006.

[200] Emily D. Lindberg, Tiffany Wu, Kristen L. Cotner, Amanda Glazer, Amir A. Jamali, Lydia L. Sohn, Tamara Alliston, and Grace D. O'Connell. Priming chondrocytes during expansion alters cell behavior and improves matrix production in 3d culture. *Osteoarthritis and Cartilage*, 32(5):548–560, 2024.

[201] A. R. Phull, S. H. Eo, Q. Abbas, M. Ahmed, and S. J. Kim. Applications of chondrocyte-based cartilage engineering: An overview. *Biomed Res Int*, 2016:1879837, 2016.

[202] Clarisse Zigan, Claudia Benito Alston, Aritra Chatterjee, Luis Solorio, and Deva D. Chan. Characterization of composite agarose–collagen hydrogels for chondrocyte culture. *Annals of Biomedical Engineering*, 2024.

[203] Zijun Zhang. Chondrons and the pericellular matrix of chondrocytes. *Tissue Engineering Part B: Reviews*, 21(3):267–277, 2015.

[204] N. A. Zelenski, H. A. Leddy, J. Sanchez-Adams, J. Zhang, P. Bonaldo, W. Liedtke, and F. Guilak. Type vi collagen regulates pericellular matrix properties, chondrocyte swelling, and mechanotransduction in mouse articular cartilage. *Arthritis Rheumatol*, 67(5):1286–94, 2015.

[205] Jacob P. Fredrikson, Priyanka P. Brahmachary, Ayten E. Erdoğan, Zachary K. Archambault, James N. Wilking, Ronald K. June, and Connie B. Chang. Metabolomic profiling and mechanotransduction of single chondrocytes encapsulated in alginate microgels. *Cells*, 11(5):900, 2022.

[206] T. T. Chowdhury, S. Arghandawi, J. Brand, O. O. Akanji, D. L. Bader, D. M. Salter, and D. A. Lee. Dynamic compression counteracts il-1b induced inducible nitric oxide synthase and cyclo-oxygenase-2 expression in chondrocyte/agarose constructs. *Arthritis Research and Therapy*, 10(2):R35, 2008.

[207] Aaron A. Jutila, Donald L. Zignego, Bradley K. Hwang, Jonathan K. Hilmer, Timothy Hamerly, Cody A. Minor, Seth T. Walk, and Ronald K. June. Candidate mediators of chondrocyte mechanotransduction via targeted and untargeted metabolomic measurements. *Archives of Biochemistry and Biophysics*, 545:116–123, 2014.

[208] Aaron A. Jutila, Donald L. Zignego, William J. Schell, and Ronald K. June. Encapsulation of chondrocytes in high-stiffness agarose microenvironments for in vitro modeling of osteoarthritis mechanotransduction. *Annals of Biomedical Engineering*, 43(5):1132–1144, 2015.

[209] Carley N. McCutchen, Donald L. Zignego, and Ronald K. June. Metabolic responses induced by compression of chondrocytes in variable-stiffness microenvironments. *Journal of Biomechanics*, 64:49–58, 2017.

[210] Eric M. Darling, Matthew Topel, Stefan Zauscher, Thomas P. Vail, and Farshid Guilak. Viscoelastic properties of human mesenchymally-derived stem cells and primary osteoblasts, chondrocytes, and adipocytes. *Journal of biomechanics*, 41(2):454–464, 2008.

[211] M. A. McLeod, R. E. Wilusz, and F. Guilak. Depth-dependent anisotropy of the micromechanical properties of the extracellular and pericellular matrices of articular cartilage evaluated via atomic force microscopy. *J Biomech*, 46(3):586–92, 2013.

[212] M. Danalache, R. Kleinert, J. Schneider, A. L. Erler, M. Schwitalle, R. Riester, F. Traub, and U. K. Hofmann. Changes in stiffness and biochemical composition of the pericellular matrix as a function of spatial chondrocyte organisation in osteoarthritic cartilage. *Osteoarthritis Cartilage*, 27(5):823–832, 2019.

[213] F. Guilak and V. C. Mow. The mechanical environment of the chondrocyte: a biphasic finite element model of cell-matrix interactions in articular cartilage. *J Biomech*, 33(12):1663–73, 2000.

[214] B. V. Nguyen, Q. Wang, N. J. Kuiper, A. J. El Haj, C. R. Thomas, and Z. Zhang. Strain-dependent viscoelastic behaviour and rupture force of single chondrocytes and chondrons under compression. *Biotechnol Lett*, 31(6):803–9, 2009.

[215] D. R. Haudenschild, J. Chen, N. Pang, N. Steklov, S. P. Grogan, M. K. Lotz, and D. D. D'Lima. Vimentin contributes to changes in chondrocyte stiffness in osteoarthritis. *J Orthop Res*, 29(1):20–5, 2011.

[216] M. Neubauer, P. P. Brahmachary, A. Fine, R. K. June, and S. Warnat. Viscoelastic recovery times of chondrocytes measured using a novel 3d printed device. *[Manuscript in preparation]*, 2024.

[217] G. M. Lee, T. A. Paul, M. Slabaugh, and S. S. Kelley. The incidence of enlarged chondrons in normal and osteoarthritic human cartilage and their relative matrix density. *Osteoarthritis and Cartilage*, 8(1):44–52, 2000.

[218] I. Youn, J. B. Choi, L. Cao, L. A. Setton, and F. Guilak. Zonal variations in the three-dimensional morphology of the chondron measured in situ using confocal microscopy. *Osteoarthritis and Cartilage*, 14(9):889–897, 2006.

[219] Thomas M. Randau, Frank A. Schildberg, Mauro Alini, Matthias D. Wimmer, El-Mustapha Haddouti, Sascha Gravius, Keita Ito, and Martin J. Stoddart. The effect of dexamethasone and triiodothyronine on terminal differentiation of primary bovine chondrocytes and chondrogenically differentiated mesenchymal stem cells. *PLOS ONE*, 8(8):e72973, 2013.

[220] Valery A. Loiko, Gennady I. Ruban, Olga A. Gritsai, Alexey D. Gruzdev, Svetlana M. Kosmacheva, Natalia V. Goncharova, and Alexander A. Miskevich. Morphometric model of lymphocyte as applied to scanning flow cytometry. *Journal of Quantitative Spectroscopy and Radiative Transfer*, 102(1):73–84, 2006.

[221] Rowena McBeath, Dana M. Pirone, Celeste M. Nelson, Kiran Bhadriraju, and Christopher S. Chen. Cell shape, cytoskeletal tension, and rhoa regulate stem cell lineage commitment. *Developmental Cell*, 6(4):483–495, 2004.

[222] Zeynab Mousavikhamene, Daniel J. Sykora, Milan Mrksich, and Neda Bagheri. Morphological features of single cells enable accurate automated classification of cancer from non-cancer cell lines. *Scientific Reports*, 11(1):24375, 2021.

[223] Christina M Chavez, Marizeth Groenewald, Amanda B Hulfachor, Gideon Kpurubu, Rene Huerta, Chris Todd Hittinger, and Antonis Rokas. The cell morphological diversity of saccharomycotina yeasts. *FEMS Yeast Research*, 24, 2023.

[224] Weiqi Fu, Yuexuan Shu, Zhiqian Yi, Yixi Su, Yiwen Pan, Fan Zhang, and Sigurdur Brynjolfsson. Diatom morphology and adaptation: Current progress and potentials for sustainable development. *Sustainable Horizons*, 2:100015, 2022.

[225] P. R. J. Yulo and H. L. Hendrickson. The evolution of spherical cell shape; progress and perspective. *Biochem Soc Trans*, 47(6):1621–1634, 2019.

[226] Yingjun Yan, Liwei Jiang, Karl J. Aufderheide, Gus A. Wright, Alexander Terekhov, Lino Costa, Kevin Qin, W. Tyler McCleery, John J. Fellenstein, Alessandro Ustione, J. Brian Robertson, Carl Hirschie Johnson, David W. Piston, M. Shane Hutson, John P. Wikswo, William Hofmeister, and Chris Janetopoulos. A microfluidic-enabled mechanical microcompressor for the immobilization of live single- and multi-cellular specimens. *Microscopy and microanalysis : the official journal of Microscopy Society of America, Microbeam Analysis Society, Microscopical Society of Canada*, 20(1):141–151, 2014.

[227] J. A. Zinskie, M. Shribak, M. F. Bruist, K. J. Aufderheide, and C. Janetopoulos. A mechanical microcompressor for high resolution imaging of motile specimens. *Exp Cell Res*, 337(2):249–56, 2015.

[228] Aydogan Ozcan and Euan McLeod. Lensless imaging and sensing. *Annual Review of Biomedical Engineering*, 18(1):77–102, 2016.

[229] Vivek Boominathan, Jacob T. Robinson, Laura Waller, and Ashok Veeraraghavan. Recent advances in lensless imaging. *Optica*, 9(1):1–16, 2022.

[230] You-Hai Liu, Tian-Xiang Qin, Ying-Ce Wang, Xing-Wang Kang, Jun Liu, Jia-Chen Wu, and Liang-Cai Cao. Research advances in simple and compact optical imaging techniques. *Acta Physica Sinica*, 72(8):084205–1–084205–26, 2023.

[231] Guoan Zheng, Seung Ah Lee, Samuel Yang, and Changhuei Yang. Sub-pixel resolving optofluidic microscope for on-chip cell imaging. *Lab on a Chip*, 10(22):3125–3129, 2010.

[232] Yuan Fang, Ningmei Yu, Runlong Wang, and Dong Su. An on-chip instrument for white blood cells classification based on a lens-less shadow imaging technique. *PLOS ONE*, 12(3):e0174580, 2017.

[233] Xiwei Huang, Yu Jiang, Xu Liu, Hang Xu, Zhi Han, Hailong Rong, Haiping Yang, Mei Yan, and Hao Yu. Machine learning based single-frame super-resolution processing for lensless blood cell counting. *Sensors*, 16(11):1836, 2016.

[234] John R. Lake, Keith C. Heyde, and Warren C. Ruder. Low-cost feedback-controlled syringe pressure pumps for microfluidics applications. *PLOS ONE*, 12(4):e0175089, 2017.

APPENDICES

APPENDIX A

LAPLACE TRANSFORMS

The Laplace transform enables conversion of differential equations into algebraic equations, greatly simplifying the solution methods. A piecewise-continuous function of a real variable (in this case t, in the time-domain) defined for $t \geq 0$ can be transformed to a function of complex variable s in the s-domain. The Laplace transform and is defined in Equation A.1.

$$\mathcal{L}\{f(t)\} = \hat{f}(s) = \int_0^\infty f(t)e^{-st}\,dt \tag{A.1}$$

The Laplace transform of time derivatives are:

$$\begin{aligned} \mathcal{L}\{\dot{f}\} &= s\hat{f} - f(0) \\ \mathcal{L}\{\ddot{f}\} &= s^2\hat{f} - sf(0) - \dot{f}(0), \end{aligned} \tag{A.2}$$

and some useful transforms are shown in Table A.1, in which α is a constant, $H(t)$ is the Heaviside step function, and $\delta(t)$ is the Dirac delta function.

Table A.1: Useful Laplace transforms.

$f(t)$	$\hat{f}(s)$
α	α/s
$H(t)$	$1/s$
$\delta(t-\tau)$	$e^{-\tau s}$
$\dot{\delta}(t)$	s
$e^{-\alpha t}$	$1/(\alpha+s)$
$(1-e^{-\alpha t})/\alpha$	$1/s(\alpha+s)$
$t/\alpha - (1-e^{-\alpha t})/\alpha^2$	$1/s^2(\alpha+s)$

APPENDIX B

SUPPLEMENTAL MATERIAL FOR: VISCOELASTIC RECOVERY TIMES OF CHONDROCYTES MEASURED USING A NOVEL 3D-PRINTED DEVICE

An FTIR spectrum (Fig. B.1) of the untaped glass and glass with water soluble tape removed show consistent peaks while the spectrum of the tape pressure sensitive adhesive (PSA) and backing show many additional peaks not found in the other spectra. This result demonstrates that the tape is effectively removed, and no residue remains on the glass.

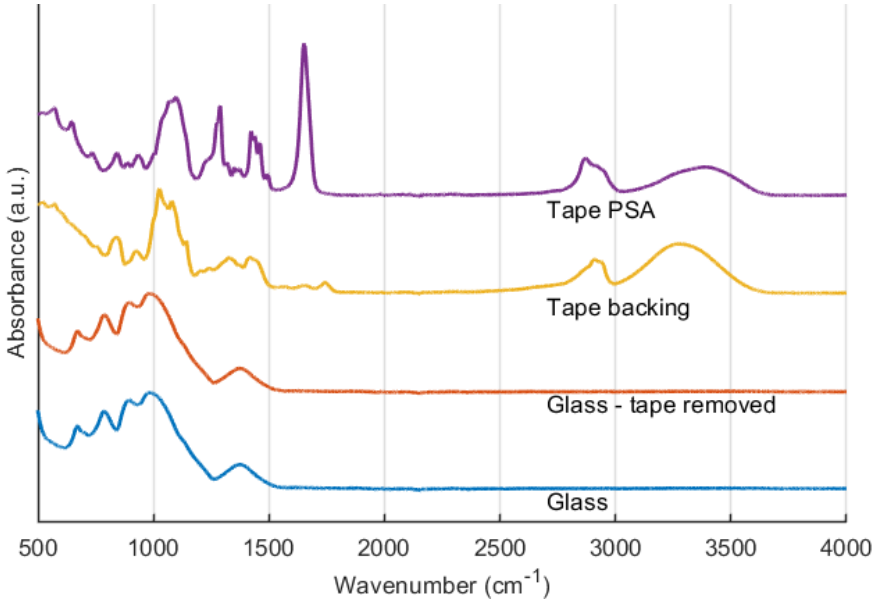


Figure B.1: FTIR spectra of glass and tape showing effective tape removal.

The height of the microfluidic chamber was controlled by a syringe mounted in a syringe pump, shown in Fig. B.2. A piezo-resistive pressure sensor (PRESS-S-000, Pendotech, USA) was connected to the syringe to monitor the pressure of the control chamber. To output of the sensor was amplified by a simple amplifier circuit [234] with a gain factor of 205. When the sensor and circuit was powered by 9 volts, the sensitivity of the sensor was 0.2598 V/psig. The output of this circuit was measured with a LabJack U6 connected to LabVIEW 2017. The custom VI takes desired pressure or pressure profile as input, measures the voltage of the pressure sensor circuit, calculates the pressure, and sends commands to the syringe pump controlling the displacement of the control chamber syringe based on LabVIEWs built in a custom proportional feedback loop VI. The response time and reliability of the pressure controller system was evaluated with 8 psig step profile. This pressure was chosen as it was the maximum pressure ever used in experiments.

The response time of the pressure controller under minimum to maximum pressure changes used in any experiments is demonstrated in Fig. B.3. The rise and fall times are consistent with a response time of 3 seconds. However, the pressures used in the experiments were set such that the movable glass was just above the cells and then moved to clamp them, such that the actual pressure change and response time was lower than the maximum three seconds.

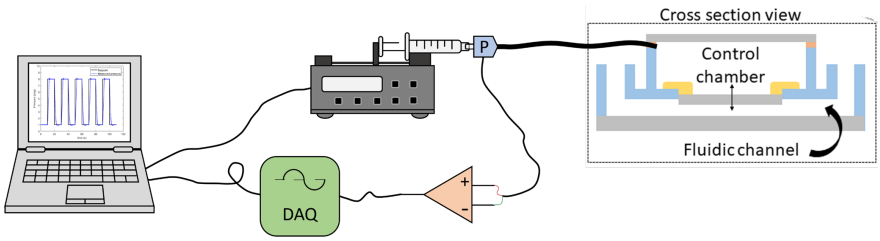


Figure B.2: An overview schematic of the custom pressure controller. A pressure sensor on a syringe mounted in a syringe pump is controlled through LabVIEW on a computer. The pressure sensor is connected to the control chamber by tubing and its electrical output is fed back to the computer through a DAC after passing through a gain circuit. A simple P control algorithm is used to control the pressure in the feedback loop.

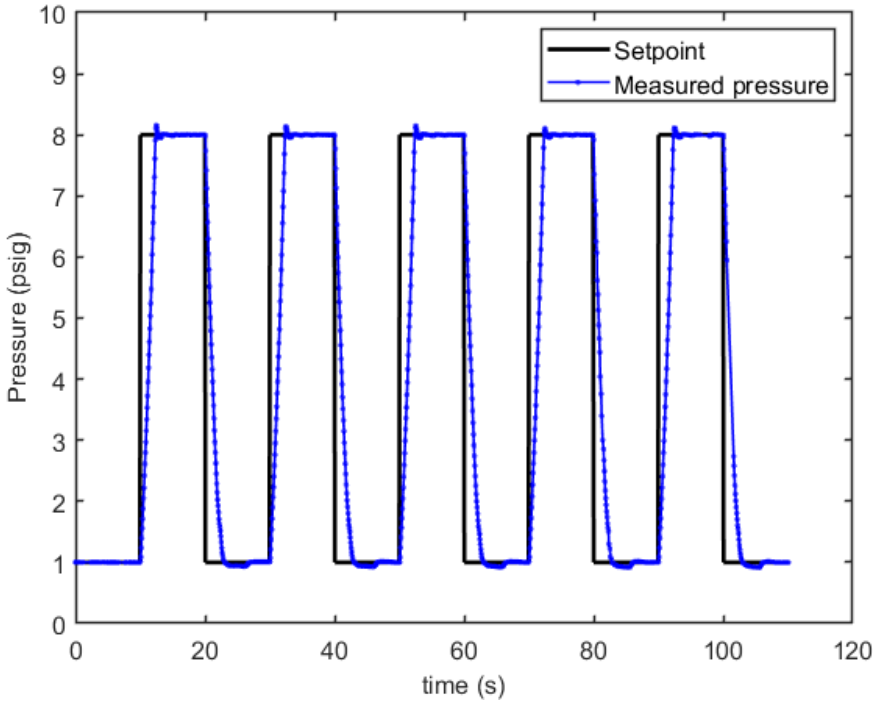


Figure B.3: The setpoint vs measured pressure for the custom pressure controller. The maximum response time used in any experiments was three seconds.

The uniformly deformed cells from Fig. 4.7 and Fig. 4.8 are displayed in Fig. B.4 to show that there was no apparent relationship between cell diameter and the total/permanent strain.

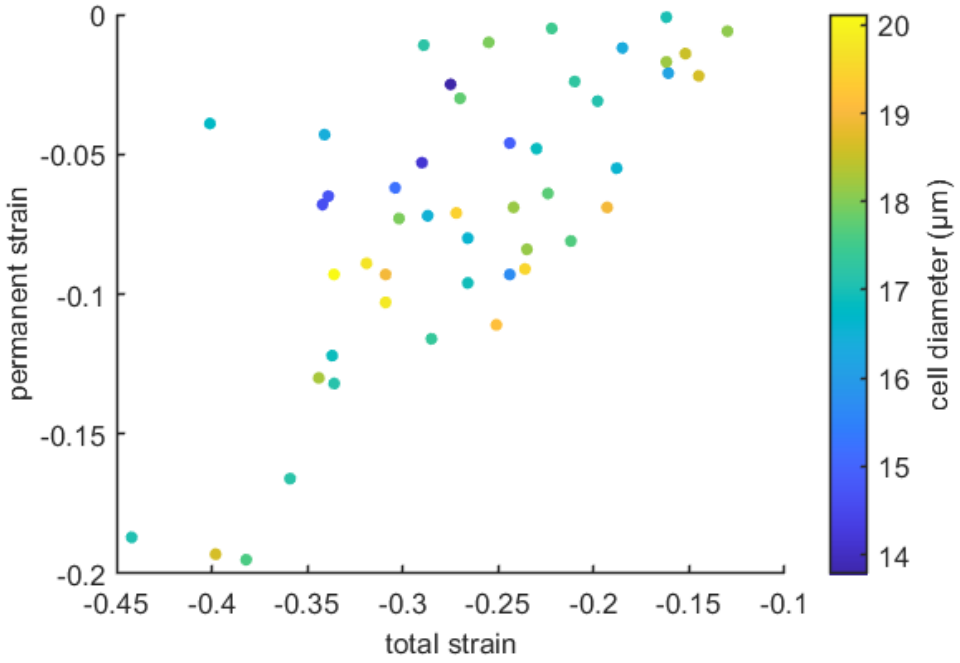


Figure B.4: Calculated permanent vs total strain for uniformly deformed cells. Each point is colored based on cell diameter. There appears to be no relation between cell size and permanent strain.